10 years of rapidly disentangling drivers of extreme weather disasters

Author list

Friederike Otto, *Centre for Environmental Policy, Imperial College, London, UK*
Ben Clarke, *Centre for Environmental Policy, Imperial College, London, UK*
Clair Barnes, *Centre for Environmental Policy, Imperial College, London, UK*
Joyce Kimutai, *Centre for Environmental Policy, Imperial College, London, UK*
Mariam Zachariah, *Centre for Environmental Policy, Imperial College, London, UK*
Niklas Merz, *Centre for Environmental Policy, Imperial College, London, UK*
Dora Vrkic, *Grantham Institute for Climate Change and the Environment, Imperial College, London, UK*
Sjoukje Philip, *Royal Netherlands Meteorological Institute (KNMI), De Bilt, The Netherlands*
Sarah Kew, *Royal Netherlands Meteorological Institute (KNMI), De Bilt, The Netherlands*
Izidine Pinto, *Royal Netherlands Meteorological Institute (KNMI), De Bilt, The Netherlands*
Maja Vahlberg, *Red Cross Red Crescent Climate Centre, The Hague, the Netherlands; Swedish Red Cross, Stockholm, Sweden (based in Ubmeje/Umeå, Sweden)*
Roop Singh, *Red Cross Red Crescent Climate Centre, The Hague, The Netherlands; Columbia University, New York, USA (based in New Jersey, USA)*
Zinzi Horne, *Red Cross Red Crescent Climate Centre, The Hague, The Netherlands (based in Kingstown, Saint Vincent and the Grenadines)*
Julie Arrighi, *Global Disaster Preparedness Centre, American Red Cross, Washington D.C., USA; Red Cross Red Crescent Climate Centre, The Hague, The Netherlands; University of Twente, Enschede, The Netherlands (based in New York, USA)*
Nathan Sparks, *Department of Physics, Imperial College London, UK*
Joseph Giguere, *Climate Central, Princeton, NJ 08542, USA*
Daniel Gilford, *Climate Central, Princeton, NJ 08542, USA*

1. Introduction

While climate change is often talked about in the context of global mean temperature, the impacts on people and nature manifest primarily through the changing intensity and frequency of extreme weather events, with the very first IPCC assessment report stating that changes in the extremes will have a larger impact on society than changes in the means (IPCC, 1990). However, it took more than a decade to develop the methodologies from this theoretical understanding to actually link observed extreme weather events with human-induced climate change. After Allen (2003) developed the idea in February 2003, it took almost two more years until December 2004 for the first extreme weather event - the devastating, deadly European heatwave 2003 - to be formally attributed to human-induced climate change (Stott et al., 2004).

While this paved the way to enable scientists to understand how the burning of fossil fuels affects extreme weather events today, this development did not reach the general public and many influential media outlets kept repeating the statement that “no single event can be attributed to human-caused climate change” (Painter et al., 2021). To address this, World Weather Attribution was founded ten years ago with the objective of providing scientific evidence on the role of climate change in the immediate aftermath of an extreme weather event, when the causes of disasters are still discussed by the general public and the media. Since the first study was published in December 2014, the science of attribution and the work of World Weather Attribution has made huge progress. Starting with case studies on different types of extreme events, such as heavy rainfall in the UK and Chennai, droughts in Ethiopia and Brazil, and heatwaves in Europe that were all peer-reviewed after the publication of the rapid assessments, we developed a formal protocol for rapid studies. This combines different lines of evidence and different types of climate models with observational data sets to provide robust attribution statements (Philip et al., 2020).

While the underlying idea behind the scientific methods has not changed compared to the early years of World Weather Attribution, the types of events that can now be attributed - and the development of the science overall - has changed dramatically. Some of the deadliest extreme weather events since the first attribution study have not been assessed in an attribution study at all (Otto et al., 2023), including one of the deadliest extreme weather event within the last 20 years, Cyclone Nargis, that hit Myanmar in 2008 and took more than 138,000 lives. At the same time, others might have falsely or misleadingly been blamed on climate change alone (Raju et al. 2022), without considering the key factors of vulnerability and exposure that turn weather into disasters. Similarly, while events such as the extremely deadly 2010 Russian heatwave were studied a lot at the time (Otto et al., 2012; Rahmstorf and Coumou 2011; Dole et al., 2011), and have since become benchmark events for identifying the role of climate change, they would be assessed differently today. This is in light of more than a decade of both methodological development and, crucially, ever increasing greenhouse gas emissions.

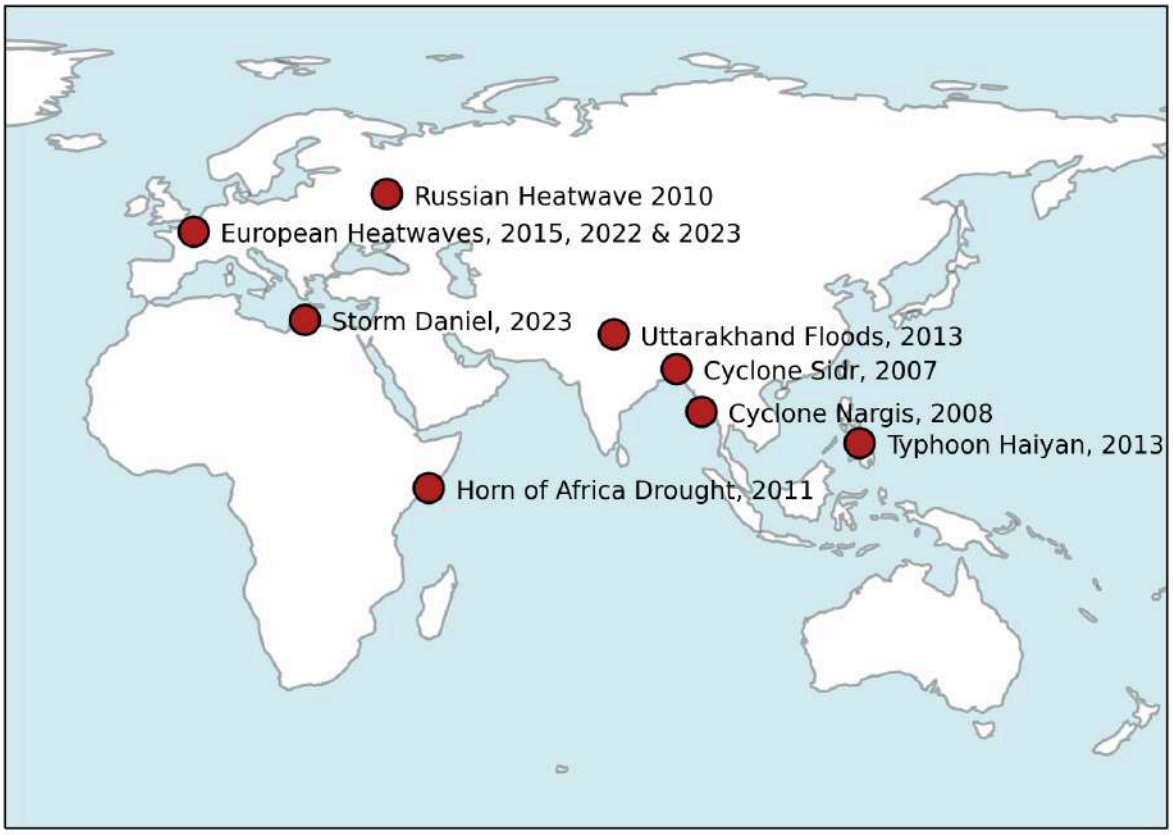

Fig. 1: 10 deadliest extreme weather events since 2004 according to EM-DAT.

10 deadliest extreme weather disasters

To mark the 10th anniversary of World Weather Attribution, we look back at the 10 deadliest extreme weather events in the 20 years since the first attribution study. We use these to highlight key findings and developments in science as well as changes since some of the earlier studies were undertaken, due to the additional global warming in recent years. Beginning with the two first attribution assessments of tropical cyclones Sidr (Bangladesh, 2007) and Nargis (Myanmar, 2008), we go on to discuss the Russian heatwave (2010), the Horn of Africa drought (2011), the deadly Uttarakhand floods (2013), Typhoon Haiyan (2013), three European heatwaves (2015, 2022, 2023), and the heavy rainfall related to Mediterranean storm Daniel (2023). While only undertaking the first ever attribution studies for the two oldest events, the storms Sidr and Nargis, we assess the other events in the context of more recent events of the same type and, in the cases of the Russian heatwave and the floods in Uttarakhand, also new data. We summarise these findings and demonstrate how much can be learned by using different approaches and methodologies. The fact that there are many studies now also highlights that the often-feared scenario - that different studies with differing quantitative attribution statements would lead to confusion, increased distrust in climate research, or unethical political decision making (Hulme, 2014) - has, so far, not materialised.

We base the list of the 10 deadliest events on the disaster database EM-DAT, as it is the most comprehensive database available. National entries for individual European heatwaves have been grouped together. It is important to note the database is very incomplete,

especially when it comes to heatwaves outside Europe; African heatwaves, which are rarely studied, are almost entirely missing, meaning we don't have an understanding of how many people are dying in heatwaves in Africa (Harrington and Otto, 2020), or indeed most of the hottest, most populated and poorest parts of the world.

This fact highlights the most important learning and subsequent development in the short history of event attribution science - that is, that inequality is the key factor in attribution assessments. It drives not only what we know about the events in the first place and how well an attribution study can be undertaken due to data availability and scientific capacity (Otto et al., 2020) but also whether and to what extent any given extreme weather event turns into a disaster. This is why including vulnerability and exposure assessments into the framework of extreme event attribution is the most important development in the science of attribution in the last 20 years. Not only does it help contextualise attribution and inform policy, it also supports local governments and citizens to use their agency to become more resilient in a changing climate.

While many drivers of vulnerability and exposure are location specific and apply differently for different demographics, there are also findings that hold universally and are crucial to highlight when reporting on extreme weather events, even in the absence of a specific attribution study.

Key findings from Vulnerability and Exposure reviews

Having analysed the vulnerability and exposure factors driving impacts in numerous events, there are several trends and lessons learned emerging from this body of work.

1 Put the most vulnerable people first

Time and again, our analyses of disasters have demonstrated that certain people are more susceptible to impacts from extreme weather events due to social vulnerability factors. It is the elderly who tend to die disproportionately during extreme heat events (e.g. WWA, 2024 Sahel heatwave, WWA, 2023 Northern Hemisphere heatwave, WWA, 2023 South America heatwave). It is marginalised communities affected by conflict and displacement (e.g. WWA, 2024 Sudan floods, WWA, 2020-2023 Syria, Iraq and Iran drought, WWA, 2024 Mindanao floods, WWA, 2023 Horn of Africa drought, WWA, 2024 Storm Bettina), people with disabilities or those who lack access to information (e.g. WWA, 2024 Central Europe floods) that are disproportionately affected by floods and storms. It is subsistence farmers that suffer severe food insecurity as a result of precipitation changes (e.g. WWA, 2021 Madagascar drought). Yet, many programs, policies, and plans exclude or fail to address the differential needs of the most vulnerable people. People are incredibly resilient, relying on coping mechanisms and social networks in order to manage and bounce back from a disaster (e.g. WWA, 2024 Rio Grande do Sul floods), but this often leaves them further behind as shocks mount and can give rise to disaster poverty cycles, which occur when disasters deplete households' resources and disrupt livelihoods, preventing full recovery. This was observed in the aftermath of the 2022 Pakistan floods (Otto et al., 2023), where recent estimates suggest that the devastating floods increased the national poverty rate by up to 4.3 percentage

points, equal to another 9 million people (Knippenberg et al., 2024). Similarly, in Nigeria, mere averages of 52.5 and 41.5% of the urban and rural populations, respectively, had recovered from the 2022 floods (WWA, 2022 West Africa floods) before the 2024 floods (WWA, 2024 Sudan and Nigeria floods) hit in nearly the same place (UNDP, 2023), further straining households' abilities to recover. Relying on inherent resilience places an undue burden on people and communities.

Shock-responsive social protection systems can support the poorest and most vulnerable people during hard times. Cash transfers to help families cover immediate needs, preventing disruption of livelihoods through livelihood insurance schemes, relocation assistance and housing repair grants, skills training to diversify or change sources of income from climate-sensitive livelihoods. For example, in Texas, US, the Comprehensive Energy Assistance Program provides financial assistance to pay energy bills during extreme temperatures (WWA, 2024 North and Central America heatwave). Additionally, as seen during 2024 Hurricane Helene (WWA, 2024 Hurricane Helene), various U.S federal shock-responsive programs provide aid to affected individuals and businesses, such as FEMA which offers rental, home repair, and legal assistance, and the Disaster Unemployment Assistance which supports those who lose employment. Similarly, as highlighted in the study on the 2024 Southern African drought (WWA, 2024 Southern Africa Drought), the governments in Mozambique and Zambia are currently scaling up their shock-responsive social protection systems, in part by integrating social protection into anticipatory action mechanisms.

2 From reaction to prevention

Early warning and early action often makes the difference between life and death. Early hazard detection (weather forecasts), timely and impact-based warnings, and adequate coverage of warnings to reach those most at risk can ensure that people have the information they need to evacuate out of the path of a life-threatening extreme weather event. Upgrading early warning systems in developing countries would cost around 4 billion US dollars over 5 years, according to one study, and would have a benefit-cost ratio ranging between 4 and 36 (Hallegatte, 2012).

Critically, the warnings must be linked to action and resources that enable people and responsible agencies to take the necessary life-saving measures. This was exemplified during the 2011 drought and food security crisis in Somalia in which warnings were present, but various actors failed to act on them due to lack of incentives and resources. Similarly, in 2008, during Cyclone Nargis, Myanmar faced challenges in its meteorological infrastructure, which was still in development. As a result, the general public had limited information about the cyclone, and evacuation measures were not as effective as needed. Over the past 10 years, early warning systems and forecasts have improved markedly. In Europe, for example, the GloFAS system has accurately predicted extreme flood events like the recent 2024 Central Europe floods (WWA, 2024 Central Europe Floods) days in advance. Research by Gallo et al. (2024) suggests that heat-related mortality in Europe would be about 80% higher had not adaptive measures been implemented over the past two decades. Famously, as a result of Bangladesh's Cyclone Preparedness Programme which disseminates early warnings and coordinates evacuation there has been a well above 100-fold reduction in cyclone-associated fatalities since 1970 when Cyclone Bhola took ~500,000 lives (Haque et al., 2011).

In addition, the concept of Anticipatory Action has been spearheaded by the Red Cross Red Crescent movement since 2008, and is now an integral component of various humanitarian actors' disaster risk management approaches. Anticipatory action mechanisms are built on the principles of early warning early action and leverages pre-arranged financing to activate pre-determined early action in response to an early warning.

Looking ahead, the coverage of Early Warning Systems needs to be expanded especially in developing countries, and forecasts need to be impact-based in order to inform decision making. Finally, at-risk populations need to understand warnings, and risk perception is crucial to motivate people to take preemptive measures.

3 Resilient cities by design

Urbanisation, especially of the rapid and unplanned variety, is one of defining trends of the 21st century, with the global urban population projected to increase by 2.5 billion people and nearly 90% of this growth occurring in Africa and Asia (UN DESA, 2018). Many of our attribution studies highlight how rapid, unplanned growth is driving an increase in the vulnerability and exposure of people and assets to climate extremes. The majority of the growth is happening in small and medium-sized urban areas in developing countries (UN Habitat, 2022), presenting unique challenges but also opportunities to reduce risk. Outpacing the capacity of formal housing and infrastructure to accommodate new residents, a significant portion of this urban growth tends to be concentrated in informal settlements. Planners can work with communities in informal areas to improve infrastructure and land tenure, and promote safer building practices rather than forcibly removing settlements which only deepens vulnerability (e.g. 2022 India and Pakistan heatwave (Zachariah et al., 2023). Implementing and enforcing zoning regulation can restrict construction in high-risk areas, while the protection and creation of green and blue infrastructure - such as wetlands, vegetated roofing, and urban forests - can enhance resilience to extreme weather such as flooding, extreme heat, and drought (e.g. WWA, 2023 West Mediterranean heatwave, WWA, 2024 Hurricane Milton). In certain scenarios, relocation and managed retreat may be necessary to safeguard communities (e.g. WWA, 2024 Rio Grande do Sul floods, WWA, 2023 Cyclone Gabrielle). Urban design should prioritise disaster resilience by ensuring adequate road widths for emergency vehicles, emergency shelters that are strategically located and easily accessible, and creating open spaces that can double as hazard impact mitigation infrastructure. Importantly, urban planning and design practices, as well as infrastructure more generally, must proactively incorporate not only the risks of today, but anticipate and mitigate the evolving risks of the future. Moreover, affordable housing initiatives must ensure lower-income populations have access to safe housing in lower-risk areas. Lastly, equitable access to essential services, including electricity, water, healthcare, and education, is crucial to mitigate risk.

4 Ensuring continuity of lifelines amidst extreme weather

Maintaining the continuity of critical infrastructure during extreme weather events is essential for building community resilience. A resilient energy grid, reinforced facilities, and distributed energy resources like microgrids, helps maintain power and telecommunications during weather shocks. Similarly, a robust health system with backup power, redundant water

systems, and mobile medical units ensures uninterrupted care, even in crises. Transportation networks must also be reinforced, with flood-resistant corridors, diversified modes of transportation, and optimised evacuation routes to facilitate efficient movement. To improve the reliability of and adapt these lifelines to future risks, different sectors must collaborate effectively and prioritise routine maintenance.

In recent studies, for example, we have seen the failure of water management infrastructure (e.g. WWA, 2024 Central Europe floods, WWA. 2023 Libya floods, WWA, 2024 Sudan and Nigeria floods, WWA, 2024 Rio Grande do Sul floods). In some cases, this is a result of infrastructure that was not designed for the types of extreme rainfall events that we are seeing in our new climate. In other cases, it's human factors such as conflict and disrepair that plays an outsize role in the failure (e.g. WWA, 2023 Libya floods). Similarly, other recent extreme weather events have revealed weaknesses in energy grids, transportation, and telecommunications systems (e.g. WWA, 2023 Cyclone Gabrielle, WWA, 2024 North and Central America heatwave, WWA, 2024 Amazon drought, WWA, 2022-2023 Central South America drought). Energy grids often struggle under surging demand, particularly during periods of extreme heat when increased energy needs (e.g. for air conditioning) leads to blackouts. Transportation routes are frequently compromised by flooding and landslides, leading to disrupted and unsafe mobility. Telecommunications networks often fail under severe weather, disrupting communication during the moments they are most needed to reconnect loved ones and coordinate disaster response. It's critical that ageing infrastructure is updated for the new climate.

Beyond "hard" infrastructure, it is also critical to ensure the continuity of "soft" lifelines such as livelihoods during extreme weather events. By ensuring that people can maintain their jobs, income sources, and economic activities, communities are better positioned to cope, rebuild, and recover. For periods of extreme heat, worker safety policies and regulations are important to ensure that at-risk workers (both indoor and outdoor workers, such as street vendors, manufacturers, and construction workers) have the means to take self-protective measures. These include, but are not limited to, adjusting working hours to avoid strenuous activity during the hottest hours, taking more frequent breaks, spending more time in shaded areas, drinking more, and using personal cooling gear (e.g. WWA, 2024 Asia heatwaves, WWA, 2024 North and Central America heatwave).

5 Compounding and cascading events require creative and systemic solutions

We are increasingly seeing that the impact of extreme weather events cascade into additional geographies and sectors (e.g. WWA, 2024 Nepal floods, WWA, 2024 Panama drought, 2022 India and Pakistan heatwave (Zachariah et al., 2023)). At the same time, we are seeing an increase in both compounding extreme weather events, such as wildfires and heatwaves (e.g. WWA, 2024 Pantanal fires, WWA, 2024 Chile fires, WWA, 2023 Eastern Canada fires), back-to-back storms and extreme rainfall events (e.g. WWA, 2024 Hurricane Helene and Hurricane Milton, WWA, 2022 Cyclones Ana and Batsirai, WWA, 2023-2024 UK winter storm season, WWA, 2024 Kerala landslides, WWA, 2024 Typhoon Gaemi), and weather whiplash, notably rapid shifts from dry conditions to extreme rainfall (e.g. WWA, 2023 Horn of Africa drought). This is also true for impacts, as associated with interactions between, for example, natural hazards, COVID-19, war in Ukraine impacting global food and energy prices, and more (e.g. WWA, 2022 Pakistan floods (Otto et al., 2023), WWA,

2020-2023 Syria, Iraq and Iran drought; WWA, 2024 Nepal floods).

Addressing these challenges will require creative solutions that go beyond the typical boundaries of risk management, and encompass systems-thinking (UNDRR, 2022). Prioritising solutions that have co-benefits for multiple hazards can help. For example, rain gardens and bioswales are designed to absorb and filter rainwater, reducing the risk of flooding while also contributing to cooling the surrounding area (Kasprzyk, 2022). They can be integrated into urban landscapes, helping to manage stormwater and reduce the urban heat island effect. Focusing on governance, adaptive planning and integrated risk assessments can also help reduce compounding and cascading risks (NAS, 2022).

6 Multi-hazard adaptation should be integrated into recovery

Due to the rapid nature of our assessments, we are not analysing the post-disaster recovery efforts of the events we study. However we often look back to previous, similar events in the same area, and see both the power of recovery to build back better, and the often missed opportunity to build forward to the climate of tomorrow, rather than the historical record (e.g. WWA, 2017 Hurricane Harvey, WWA, 2018, Cape Town drought).

The types of events we study are tragic in the breadth and depth of their destruction. However, once they occur, they create a critical moment in time to leapfrog our resilience to a future climate by integrating multi-hazard adaptation approaches into how we recover. For example, following a devastating flood, rebuilding to prevent impacts of the floods of the future as well as the extreme heat that will affect the same area in the future.

7 The limits to adaptation are emerging

Some of the attribution studies we have done are for events that are so unusual or so extreme that the study team has wrestled with more existential questions such as, 'would it have been feasible to have adapted to an event *so* extreme or *so* unprecedented?' Or 'can the global pace of adaptation catch-up to today's new climate, let alone the climate of the future?' Or 'When an entire town is wiped away, including the 'safe' areas, what could have reasonably been done differently?' (e.g. WWA, 2024 Rio Grande do Sul floods, WWA, 2021 Pacific Northwest USA and Canada heatwave, WWA, 2024 Hurricane Helene, WWA, 2022 Pakistan floods).

We can already start to see some of the limits to adaptation in some of these questions, such as the funding, technological feasibility and/or political will (from leaders and constituents) needed to proactively adapt infrastructure to the much more common and extreme events of today. Or socio-cultural limits such as ties to ancestral lands. With climate change, we expect to see these limits occur more frequently. As limits to adaptation grow, loss and damage funding becomes increasingly critical.

Looking ahead

Going forward, World Weather Attribution will continue to push the boundaries of science, to assess the causes of disasters, highlighting where the continued burning of fossil fuels is

making the lives of many people harder, and where inequality, conflict, political failure, and post-colonial structures lead to high vulnerability. We aim to inform the public about climate change and extreme weather and the consequences of action and inaction.

2. Tropical Cyclone Sidr - Bangladesh 2007

Key messages (from Sidr, Nargis and Haiyan):

- *Climate change affects tropical cyclones and their impacts in different ways, which we are now able to address by using multiple approaches to study several facets of tropical cyclone hazards, including precipitation, wind speeds, sea surface temperatures and potential intensity.*
- *Effective early warning systems that evacuate people from the path of a cyclone into safe shelters has been shown to save thousands of lives, especially from dangerous storm surges. When people don't perceive the risk, don't receive warnings, don't have the means to evacuate, or are not comfortable in the temporary shelters, we tend to see higher impacts.*

2.1 Introduction

Tropical cyclone (TC) Sidr formed on November 11th, 2007 in the Bay of Bengal, south of the Andaman Islands. It moved briefly westward then almost directly northwards over warm waters (Figure 2.1), intensifying to a category 5 equivalent storm by the morning of November 15th (NASA, 2007). Later on the 15th, it made landfall over Bangladesh and the wider Ganges-Brahmaputra river delta, which is one of the most densely populated low-lying areas in the world (NASA, 2007). It brought winds of over 100 mph, storm surges of up to 6 metres and heavy precipitation to the region (Reliefweb, 2008). Though the exact death toll remains unknown, between 4,000 and 15,000 people were killed and the storm caused damages of approximately $2 billion (Reliefweb, 2008; Dhaka Tribune, 2020).

The links between climate change and the features of TCs in the Bay of Bengal remain understudied, especially given the record of catastrophic events in the region: major cyclones striking Bangladesh in 1970 and 1991, as well as Nargis in Myanmar in 2008 (see next section) all caused hundreds of thousands of deaths and represent some of the deadliest events in recent decades (Paul, 2009). This is due in part to the combination of high population density in a very low-lying area (Gupta et al., 2018).

Studies on trends to date, though not attributed to climate change, suggest an increase in the overall accumulated cyclone energy in TC seasons in the North Indian ocean (comprising both the Arabian sea and Bay of Bengal); while the frequency of cyclones appears to be decreasing slightly, the number and duration of the most intense events are increasing (Balaji et al., 2018). In the Bay of Bengal alone, trends appear to be similar to the wider region with decreasing cyclone frequency but greater intensity, which are also projected to increase with further warming (Gupta et al., 2018). This trend analysis is further reinforced by high-resolution modelling of recent major TCs using a pseudo-global warming approach to test the influence of representative concentration pathways (RCPs). This study of four recent events found that with further warming, TCs in the Bay of Bengal will have slower translation speeds, and lead to more intense rainfall and winds; the TCs studied would have each been a category higher on the Saffir-Simpson scale in the highest RCP

scenarios (Jyoteeshkumar et al., 2021). Similarly, events like Cyclone Amphan will affect more people in a warmer climate due to both rising exposure and sea level rise (Mitchell et al., 2022).

The mounting evidence on the role of climate change suggests the need for complementary attribution work on historical events, including hazard, vulnerability and exposure, to shed light on changing risks.

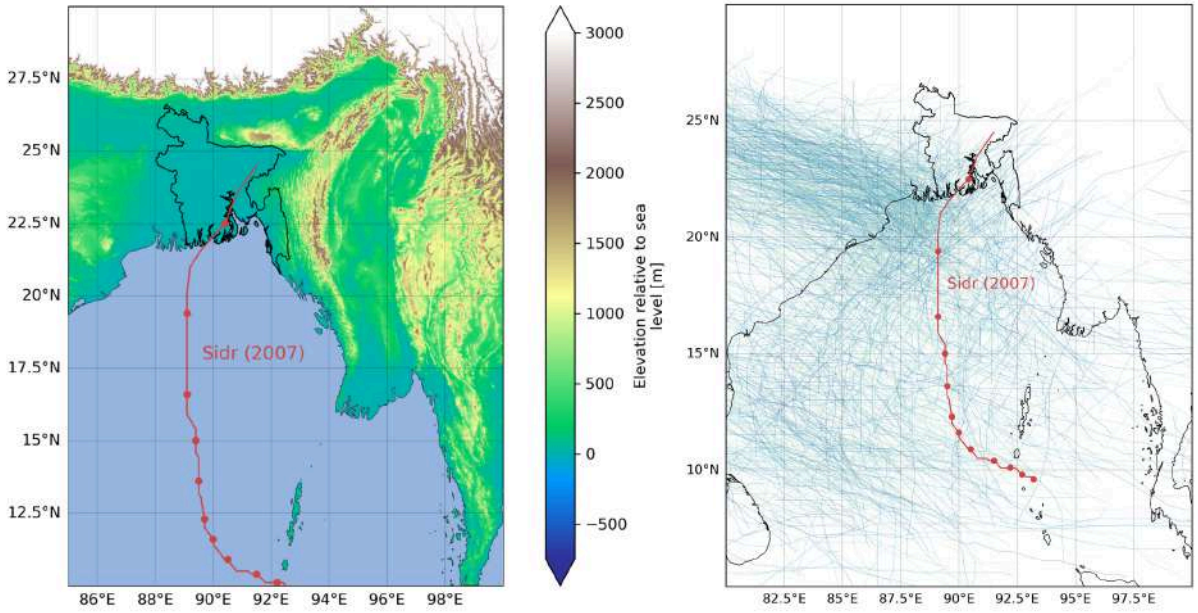

Figure 2.1: The track of Cyclone Sidr over the Bay of Bengal and into low-lying Bangladesh (shown in black). Left: the elevation of land areas in the vicinity of the storm. Data from GEBCO bathymetry. Right: All other historical cyclones in the Bay of Bengal in the IBTrACS database.

2.2 Event definition

We characterise the event in two ways in order to capture the different ways in which it led to impacts, including both extreme rainfall and high winds. The rainfall extreme is studied using probabilistic event attribution according to the WWA protocol (see section A.1.4). Cyclone Sidr made a relatively rapid landfall and passage over Bangladesh, with the majority of rainfall concentrated on one day (15th November; Figure 2.2). This rainfall affected Bangladesh and a wider part of the Ganges-Brahmaputra basin, which flows into Bangladesh. We therefore use part of this river basin, bordered at 88 °E to capture the most intense rains and 26 °N to avoid the influence of orographic rainfall, to characterise the rainfall. Finally, to minimise the influence of monsoon rains on the results, which ends in September, and still capture the cyclone season of September-December, the season of interest was chosen as October-December.

In addition, the attributable changes in wind speed intensity are assessed using a stochastic model of storm tracks and intensities (see section A.1.6), and the sea surface temperatures along the track of the storm are assessed using Climate Central's Climate Shift Index: Ocean tool (see section A.1.7) The three event definitions are summarised as follows:

- **Rainfall:** 1 day maximum precipitation over part of the Ganges-Brahmaputra basin, bordered by 88 E and 26 N, during October-December
- **Wind speeds:** cyclones of the same intensity as Sidr making landfall in a region 2 degrees from Sidr
- **Sea surface temperatures:** SSTs along the track of Cyclone Sidr

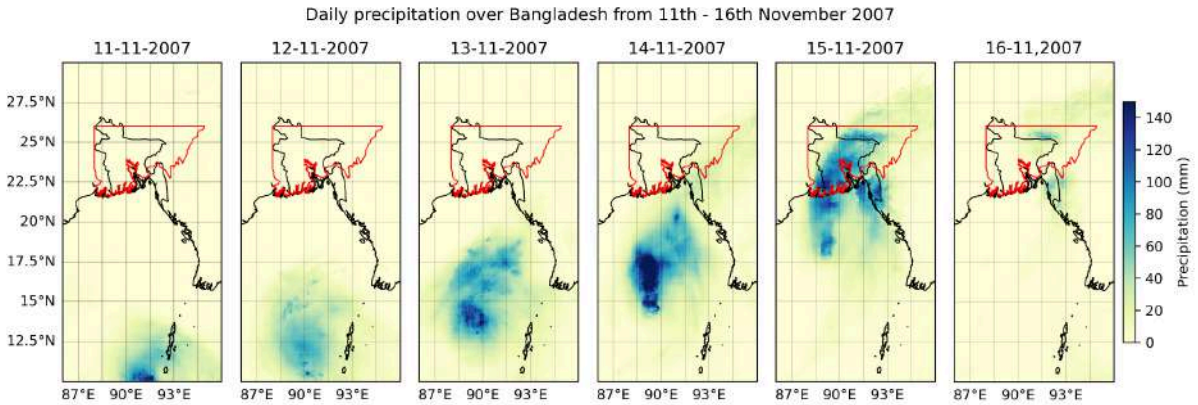

Figure 2.2: Daily precipitation over the Bay of Bengal and Bangladesh (shown in black) for several days during the passage of Cyclone Sidr. The study region, consisting of part of the Ganges-Brahmaputra river basin, is highlighted in red. Data from MSWEP.

2.3 Observational Analysis of Rainfall

To assess the changes in the likelihood and intensity of an event like Cyclone Sidr, we first use a range of observational and reanalysis datasets as described in appendix sections A.1.1 and A.1.3. This analysis follows the World Weather Attribution protocol, as described in appendix section A.1.4. This data is used to estimate the return period of the event at the time of occurrence and in 2024, as well as the changes of such extremes associated with increases in GMST (table 2.1).

Dataset	**Return period (2007)**	**Preindustrial - 2007 (0.9 C)**		**Return period (2024)**	**Preindustrial - 2024 (1.3 C)**	
		Probability Ratio	Change in magnitude (%)		Probability Ratio	Change in magnitude (%)
MSWEP	3.34 (2.21-5.76)	1.64 (0.42 - 38.79)	17.87 (-31.29 - 81.84)	2.89 (1.70-8.05)	1.99 (0.26 - 137.55)	26.70 (-41.93 - 136.84)
ERA5	5.40 (3.60-9.51)	2.53 (0.80 - 12.33)	27.87 (-6.91 - 75.74)	4.15 (2.48-10.13)	3.60 (0.72 - 28.42)	42.52 (-9.89 - 125.80)
GPCC	2.83 (1.92-5.17)	1.07 (0.42 - 10.16)	2.60 (-39.15 - 64.41)	2.74 (1.70-7.87)	1.13 (0.19 - 18.02)	5.06 (-51.27 - 102.01)

Table 2.1: Return periods, and change in probability ratio and magnitude for extreme rainfall in the region in which Sidr made landfall, due to GMST. Light blue indicates a wetting trend that crosses no change.

While all datasets show decreasing return periods between 2007 and 2024, they are broadly similar, at approximately a 2.5-5.5 year event (table 2.1). In order to compare the probability ratios and changes in magnitude in both 2007 and 2024 across models as well as observations, it would be ideal to ensure that an event of equivalent magnitude is being compared, which requires an accurate and precise assessment of the return period at each level of warming. However, given the uncertainty ranges on each return period all encapsulate all other estimates, it is not possible to precisely estimate the return period in each case. As a result, we assess changes in the 1-in-4 year event in both climates going forwards. In all three observational datasets the trend best estimate is positive, albeit with large uncertainties.

2.4 Hazard Synthesis

2.4.1 Rainfall

To undertake a full attribution of an extreme event to climate change, we synthesise results from both observations and climate models. To ensure that the climate models are fit for purpose, we first evaluate their ability to reproduce the observed characteristics of local conditions, assessed through the spatial patterns, seasonal cycles and parameters of the statistical distribution of extremes (see section A.1.5 for details). Only those that pass evaluation are combined into the final results (see section A.2.1 for evaluation results).

Dataset	**Preindustrial - 2007 (0.9 C)**		**Preindustrial - 2024 (1.3 C)**	
	Probability Ratio	Change in magnitude (%)	Probability Ratio	Change in magnitude (%)
Observations	1.64 (0.39 - 19.8)	15.6 (-30.6 - 84.0)	2.01 (0.23 - 51.2)	23.8 (-40.7 - 139)
Models	0.65 (0.33 - 1.47)	-7.21 (-24.1 - 9.96)	0.89 (0.67 - 1.51)	3.27 (-11.5 - 19.8)
Synthesis (unweighted)	1.03 (0.47 - 3.82)	4.20 (-21.3 - 32.6)	1.34 (0.45 - 6.91)	13.54 (-22.4 - 58.3)

Table 2.2: Summary of results for extreme precipitation due to Cyclone Sidr (shown in Figure A.2.3): changes due to GMST include preindustrial-2007 changes and preindustrial-2024 changes. Statistically significant increases (decreases) in probability and intensity are highlighted in dark blue (orange), while non-significant increases are highlighted in light blue (orange).

There are several interesting aspects arising from this synthesis that must be considered in its interpretation. First, to combine the results for rainfall, we use an unweighted synthesis of the two, both because observations and models disagree on the sign of the change, and because the synthesised model uncertainty does not accurately reflect the overall variability across the ensemble (Figure A.2.3). Additionally, both observational datasets and many individual models give quite different results and uncertainties depending on the time frame assessed - the additional 17 years of data for 2024 vs 2007 changes both the best estimates and uncertainties quite strongly in some cases.

At the time of occurrence in 2007, the synthesised result shows essentially no change, with the change in likelihood spanning two times lower to four times higher, and the intensity 21% lower to 33% higher than a preindustrial event. By 2024, although the uncertainty range change is still too large to distinguish a clear trend, the best estimates indicate a trend towards more similar precipitation events, with a change in likelihood ranging two times lower to seven times higher, and change in intensity from 22% lower to 58% higher, relative to a preindustrial event.

However, climate models are clearly underestimating the observed trend across both time periods, suggesting that trends in rainfall are likely higher than the synthesis statement suggests. Although with the current models we can not quantify the trend that can be attributed to climate change with confidence, it is more likely than not that it made the rainfall from Sidr heavier and more likely.

2.4.2 Wind intensity

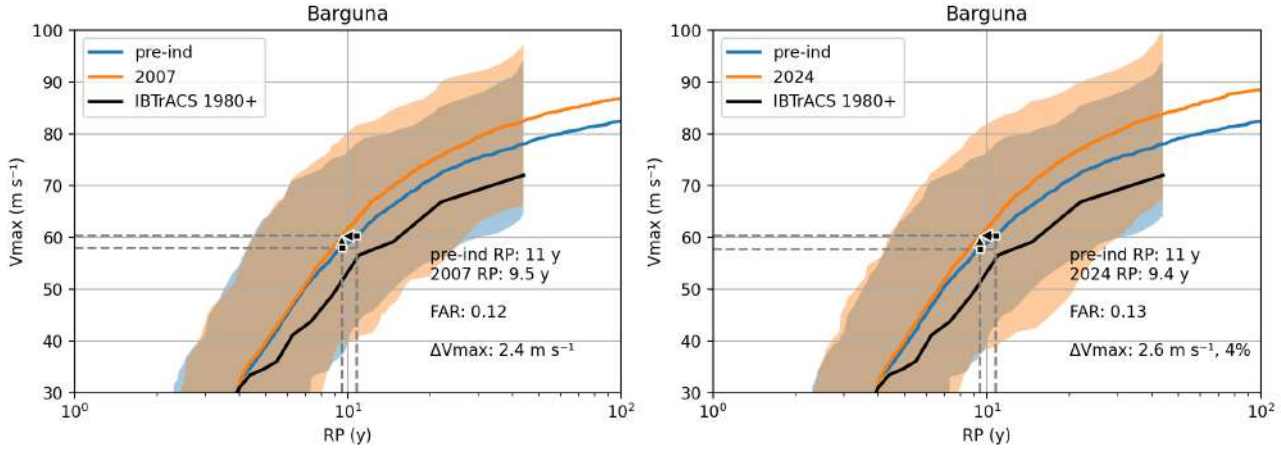

Figure 2.3: Return curves for tropical cyclones making landfall around the same region as Sidr. The orange curves show the present day climate in 2007 (left) and 2024 (right), while the blue curves show the pre-industrial climate. The black line shows the distribution of observed storms in this region since 1980.

Event	Return period (time of	Preindustrial - 2008 (0.9 C)	Preindustrial - 2024 (1.3 C)

	event)	Probability Ratio	Change in magnitude (m/s)	Probability Ratio	Change in magnitude (m/s)
Sidr	9.5	1.16	2.4	1.17	2.6

Table 2.3: Summary of results for wind speeds associated with cyclones around the landfall of Sidr.

The change in wind speed for an event like Cyclone Sidr striking southern Bangladesh is clear (Figure 2.3). At the time of occurrence, such events occurred roughly once every 9.5 years, but prior to warming of 0.9 C would have occurred only once every 11 years. This represents an increase in likelihood of approximately 16%. Equivalently, events of a similar rarity to Sidr in preindustrial times would have been approximately 2.4 m/s slower. The change in likelihood and wind speeds between preindustrial times and 2024 is very similar, at 17% more likely and 2.6 m/s more intense, suggesting a further increase since the time of occurrence.

2.4.3 Sea Surface Temperatures

On average, in 2007 temperatures along the track were made 0.69°C (1.24°F) warmer by human caused climate change (Fig. 2.4). The strongest climate-driven warming occurred early on in the life cycle of Tropical Cyclone Sidr, while it was still developing into a tropical storm (with temperatures being an estimated 0.6-0.8°C warmer due to climate change during this period). Although climate-driven warming along the track of the tropical cyclone decreased throughout its development, we estimate that prior to landfall, temperatures in the area were still 0.2°C higher than they would have been without human-caused climate change.

Event	CSI (Probability ratio)		Average change in intensity
	Average	Peak	
Cyclone Sidr (2007)	1.3	3.8	0.69 °C

Table 2.4: Summary of results for SSTs associated with the track of Sidr.

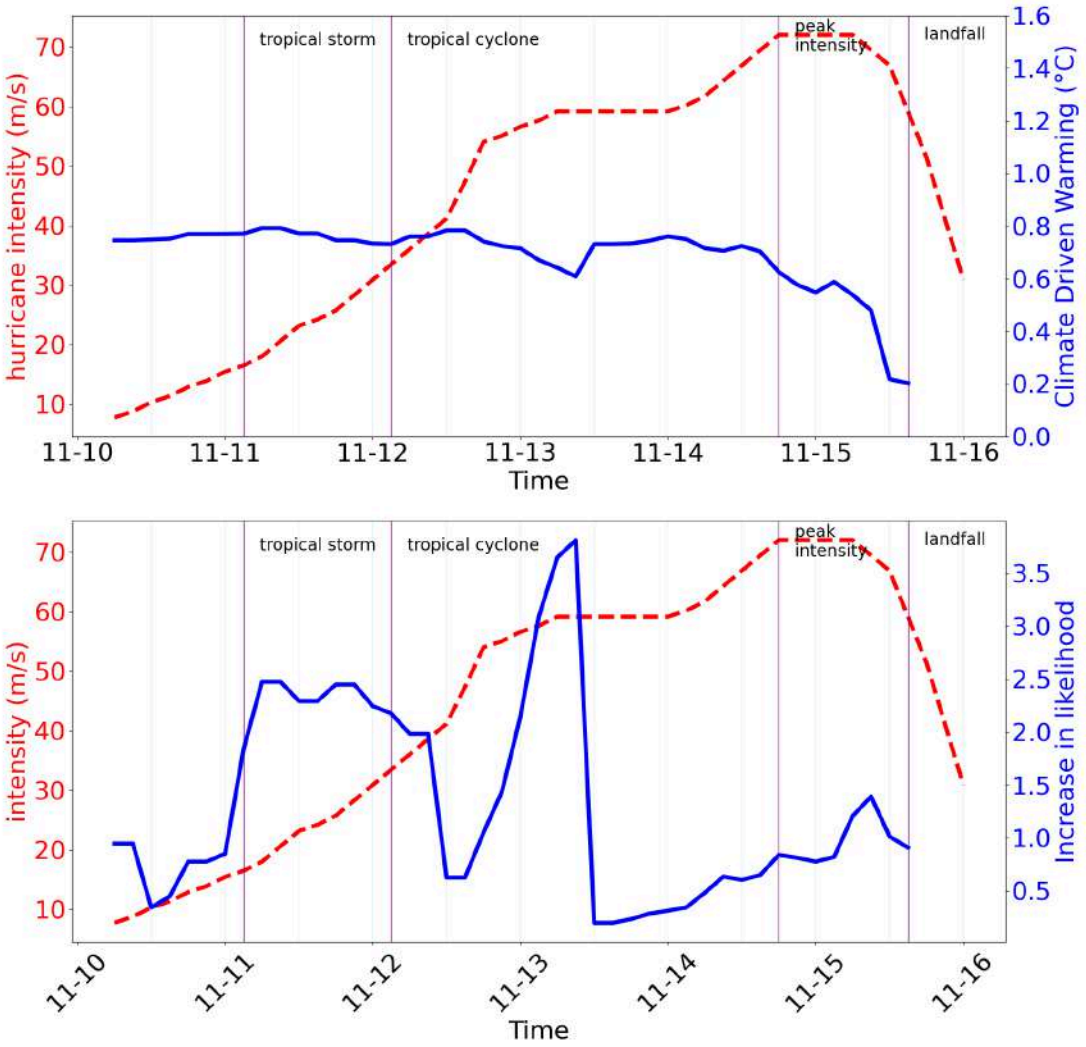

Figure 2.4: Climate driven warming (top) and increase in likelihood of sea surface temperatures occurring as a result of climate change (bottom). Data from Climate Central Ocean CSI. Additionally, both figures present intensity (as a red, dashed line).

Ocean CSI reached its highest value (3.8) on November 13th, when the storm was already a tropical cyclone on its way to peak intensity and subsequent landfall. Sea Surface Temperatures that Sidr passed over were made 3.8 times more likely to occur in the climate of 2007 (for that location and time of year) than in a world without climate change. On average, temperatures along Sidr's lifetime from disturbance to landfall were made 1.3 times more likely to occur as a result of climate change. However, throughout periods of the storm's lifetime, the Ocean CSI of SSTs occurring as a result of climate change was often less than 1, indicating that the temperatures were actually *less likely* to occur in the modern climate than the counterfactual one at these points, even though climate change driven warming has occurred. This is a result of the Ocean CSI being measured as a ratio of probabilities of the specific temperatures occurring, rather than the ratio of exceedance likelihoods. In other words, observed temperatures may be unusually cool in relation to the

modern climate with some probability P_{mod} and unusually warm in relation to the counterfactual climate with some probability $P_{counter} > P_{mod}$. This results in an Ocean CSI of less than 1. However, warming has still occurred in the region, resulting in some climate driven warming greater than 0°C (as seen for the temperatures along Sidr's track, Fig 3.4, top).

Tropical Cyclone intensities and rapid intensification are strongly related to elevated Sea Surface Temperatures (e.g. Hong and Wu 2021). Increased Sea Surface Temperatures allow for higher levels of local humidity, atmospheric instability, and potential intensity (e.g. Emanuel 2006). Although Ocean CSI values along the track were frequently less than 1, indicating that the probability of a Sea Surface Temperature along Sidr's track was more likely to occur in the counterfactual climate than the modern climate, further nuanced analysis is required: along Sidr's track, ocean temperatures were consistently more than 0.5°C warmer than they would have been in a world without climate change. We can thus conclude that warmer Sea Surface Temperatures along the track of Tropical Cyclone Sidr were influenced by human-caused climate change, which affected Sidr's development environment and made it more likely to intensify.

2.5 Vulnerability and exposure

Cyclone Sidr made landfall in southwestern Bangladesh, the most heavily populated low-lying area in the world (NASA Earth Observatory, 2007). Up to 6m storm surges took over 3,000 lives and caused unprecedented destruction, breaching coastal and river embankments, contaminating water, and damaging infrastructure (Government of Bangladesh, 2008a).

Though the Bangladesh Meteorological Department issued timely cyclone warnings, there were nevertheless several obstacles to evacuation. In many cases, people struggled to comprehend the magnitude of surges or how quickly they would arrive (Government of Bangladesh, 2008b). While 2,400 cyclone shelters were available, able to house 1.5 million of the roughly 3 million people evacuated from the low-lying coastal areas, many people struggled to understand risks posed by the signal number 10, the highest level, thereby failing to appropriately adjust their responses. In other cases, people were discouraged from seeking shelter due to disrepair, lack of gender-sensitive facilities or amenities for the disabled, or inadequate space for livestock (Government of Bangladesh, 2008b).

Moreover, Cyclone Sidr was the second natural disaster to hit Bangladesh in 2007. The preceding monsoon season, which caused extensive agricultural losses and damage to physical assets totaling almost $1.1 billion, helped compound impacts, as it likely further strained the country's resources and resilience. It also hampered humanitarian access and early evacuation due to power outages, disruption to telecommunications and impassable roads (Government of Bangladesh, 2008a).

Socio-economic factors are key drivers of vulnerability. Bangladesh is one of the poorest and most densely populated countries (Shelter Projects, 2007). Two years before Cyclone Sidr hit in 2007, the country's poverty rate was a 40% (World Bank, 2008). Limited financial means led many low-income families to settle disaster-prone areas such as coastal regions

and newly emerged lands from riverbeds. The densely populated coastal zones were especially at risk, with some residents living in informal settlements.

Since Cyclone Sidr, Bangladesh has continued to make significant strides in disaster risk management, also drawing lessons from previous cyclones, including the 1970 Cyclone Bhola (~500,000 fatalities) and 1991 Cyclone Gorky (~138,000 fatalities). Enhancements in preparedness, such as improved early warning systems, cyclone shelters, and anticipatory action, have greatly decreased casualties (Haque et al., 2011). Furthermore, cyclone walls reinforced with trees have been constructed to shield vulnerable areas from storm surges.

3. Tropical Cyclone Nargis - Myanmar 2008

Key messages - see section 2

3.1 Introduction

Tropical cyclone Nargis formed on April 28th, 2008 in the centre of the Bay of Bengal (NASA, 2008). It moved westward then northwest under the influence of a ridge to the north. After severely weakening, it steered eastwards and began to rapidly intensify on May 1st due to favourable atmospheric conditions, reaching category 4 equivalent storm by the morning of May 2nd (Shi & Wang, 2008). Later on the 2nd, it made landfall over southern Myanmar in the Ayeyarwady region, a densely populated and very low-lying area that makes up part of the Irrawaddy river delta. The storm brought winds of over 100 mph, storm surges of up to 12 ft and heavy precipitation to the region (Preventionweb, 2018). Though the exact death toll remains unknown, at least 138,000 people were killed and the storm caused damages of at least $4 billion (Reliefweb, 2018).

For evidence to date on the influence of climate change on TCs in the Bay of Bengal, see Cyclone Sidr above. Mounting evidence on the role of climate change suggests the need for complementary attribution work on historical events, including hazard, vulnerability and exposure, to shed light on changing risks.

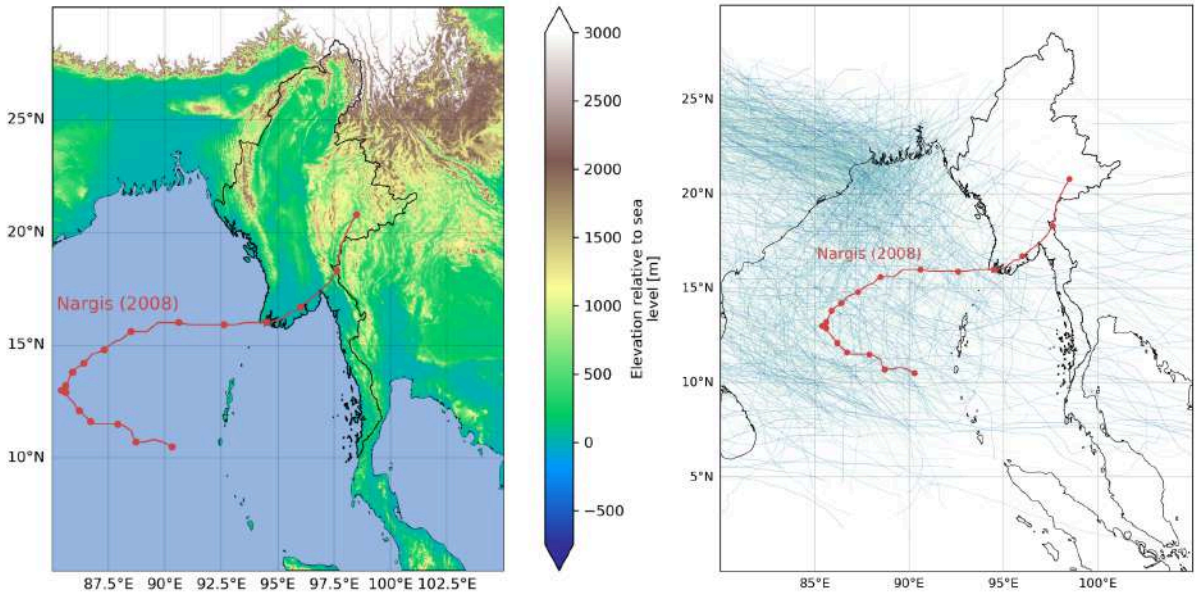

Figure 3.1: The track of Cyclone Nargis over the Bay of Bengal and into low-lying southern Myanmar (shown in black). Left: the elevation of land areas in the vicinity of the storm. Data from GEBCO bathymetry. Right: All other historical cyclones in the Bay of Bengal in the IBTrACS database.

3.2 Event definitions

We characterise the event in two ways in order to capture the different ways in which it led to impacts, including both extreme rainfall and high winds. The rainfall extreme is studied using probabilistic event attribution according to the WWA protocol (see section A.1.4). Cyclone Nargis affected southern Myanmar over two days, with the majority of rainfall concentrated on 2nd - 3rd May (Figure 3.2). However, the same region was affected by another intense rainfall event on 29-30th April, with just a day of respite. This rainfall may have preconditioned the land surface to flood more easily. As a result, we study changes in 5-day rainfall extremes to capture similarly successive events. Furthermore, the impacts of Nargis were concentrated in the southeastern part of Myanmar. We therefore border the study region as land areas within Myanmar between 15 - 20 °N (shown in Figure 3.2) to avoid other regions with different climatologies and to capture the rainfall itself. Finally, to capture the cyclone season of March-May, this was selected as the season of interest.

In addition, the attributable changes in wind speed intensity are assessed using a stochastic model of storm tracks and intensities (see section A.1.6), and the sea surface temperatures along the track of the storm are assessed using Climate Central's Climate Shift Index: Ocean tool (see section A.1.7). The three event definitions are summarised as follows:

- **Rainfall:** 5-day maximum precipitation over part of the southern Myanmar, bordered by 15-20 N, during March-May
- **Wind speeds:** cyclones of the same intensity as Nargis making landfall in a region 2 degrees from Nargis
- **Sea surface temperatures:** SSTs along the track of Cyclone Nargis

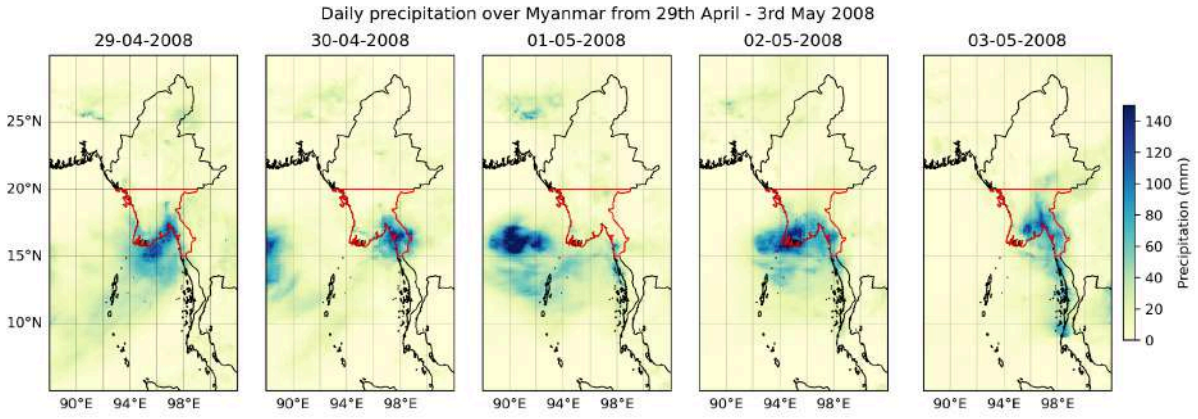

Figure 3.2: Daily precipitation over the Bay of Bengal and Myanmar (shown in black) for several days during the passage of Cyclone Nargis. The study region, consisting of part of southern Myanmar between 15-20 N, is highlighted in red. Data from MSWEP.

3.3 Observational Analysis of Rainfall

To assess the changes in the likelihood and intensity of an event like Cyclone Nargis, we first use a range of observational and reanalysis datasets as described in appendix sections A.1.1 and A.1.3. This analysis follows the World Weather Attribution protocol, as described in appendix section A.1.4. This data is used to estimate the return period of the event at the time of occurrence and in 2024, as well as the changes of such extremes associated with increases in GMST (table 2.1).

Dataset	Return period (2008)	Preindustrial - 2008 (0.9 C)		Return period (2024)	Preindustrial - 2024 (1.3 C)	
		Probability Ratio	Change in magnitude (%)		Probability Ratio	Change in magnitude (%)
MSWEP	10.45	0.69 (0.14 - inf)	-8.31 (-43.65 - 45.63)	11.36	0.69 (0.05 - inf)	-8.01 (-56.1 - 65.54)
CHIRPS	15.09	1.36 (0.22 - 36140)	5.40 (-26.86 - 56.26)	13.06	1.74 (0.10 - inf)	10.11 (-36.51 - 88.56)
ERA5	20.16	1.37 (0.41 - 13.77)	6.63 (-17.06 - 34.83)	18.13	1.57 (0.27 - 35.58)	9.60 (-23.86 - 53.70)
GPCC	3.08	24.19 (0.88 - inf)	50.94 (-3.43 - 103.43)	2.04	30.52 (1.06 - inf)	69.65 (1.26 - 175.48)

Table 3.1: Return periods, and change in probability ratio and magnitude for extreme rainfall in the region in which Nargis made landfall, due to GMST. Light blue (orange) indicates a wetting (drying) trend that crosses no change, dark blue indicates a statistically significant wetting trend.

The return periods in all datasets are broadly similar between the two time periods, and 3 out of the 4 estimate that it was a 1-in-10-20 year event (table 2.1). In order to compare the probability ratios and changes in magnitude in both 2008 and 2024 across models as well as observations, it would be ideal to ensure that an event of equivalent magnitude is being compared, which requires an accurate and precise assessment of the return period at each level of warming. However, given the uncertainty ranges on each return period all encapsulate all other estimates, it is not possible to precisely estimate the return period in each case. As a result, we assess changes in the 1-in-15 year event in both climates going forwards. Except for MSWEP, the best estimates of the trend in observational the datasets are positive, albeit with large uncertainties around it. For MSWEP the uncertainty is centred around no change.

3.4 Hazard Synthesis

3.4.1 Rainfall

To undertake a full attribution of an extreme event to climate change, we synthesise results from both observations and climate models. To ensure that the climate models are fit for purpose, we first evaluate their ability to reproduce the observed characteristics of local conditions, assessed through the spatial patterns, seasonal cycles and parameters of the statistical distribution of extremes (see section A.1.5 for details). Only those that pass evaluation are combined into the final results (see section A.3.1 for evaluation results).

Dataset	Preindustrial - 2008	Preindustrial - 2024

	(0.9 C)		(1.3 C)	
	Probability Ratio	Change in magnitude (%)	Probability Ratio	Change in magnitude (%)
Observations	2.36 (0.056 - 2560)	11.7 (-37.1 - 93.3)	2.75 (0.04 - 9370)	17.1 (-44.8 - 139)
Models	1.07 (0.37 - 3.30)	9.71 (-12.4 - 36.4)	0.46 (0.101 - 2.23)	-15.6 (-44.8 - 29.0)
Synthesis (unweighted)	1.59 (0.23 - 54.8)	10.71 (-18.7 - 48.7)	1.12 (0.12 - 70.7)	0.75 (-35.4 - 50.6)

Table 3.2: Summary of results for extreme precipitation due to Cyclone Nargis (shown in Figure A.3.3): changes due to GMST include preindustrial-2008 changes and preindustrial-2024 changes. Statistically significant increases (decreases) in probability and intensity are highlighted in dark blue (orange), while non-significant increases are highlighted in light blue (orange).

As with Cyclone Sidr above, there are several interesting aspects arising from this synthesis that must be considered in its interpretation. First, to combine the results for rainfall, we use an unweighted synthesis of the two, both because observations and models disagree on the sign of the change, and because the synthesised model uncertainty does not accurately reflect the overall variability across the ensemble (Figure A.3.3). Additionally, both observational datasets and many individual models give quite different results and uncertainties depending on the time frame assessed - the additional 16 years of data for 2024 vs 2008 changes both the best estimates and uncertainties quite strongly in some cases.

The synthesised results show that, at the time of occurrence in 2008, the rainfall likely increased substantially, with the change in likelihood spanning four times lower to 55 times higher, and the intensity 19% lower to 49% higher than a preindustrial event. By 2024, the models deviate more from the observed trend, showing a tendency to a decrease where observations give an increase. This results in a much wider uncertainty range for the unweighted synthesis results, which still suggest an overall wetting but with very high uncertainty.

Overall, there is very low confidence in the synthesis result best estimates. This is due to a combination of the disagreement between models and observations in 2024, the high uncertainties, and the overall poor performance of models for this region, with none rated ‘good’ in the model evaluation process (Table A.3.1). Nonetheless, the same arguments hold as for Cyclone Sidr regarding the qualitative attribution. Since climate models are clearly underestimating the observed trend across both time periods, trends in rainfall are likely higher than the synthesis best estimates suggest. As a result, although with the current models we can not quantify the trend that can be attributed to climate change with confidence, it is more likely than not that it made the rainfall from Nargis heavier and more likely.

3.4.2 Wind intensity

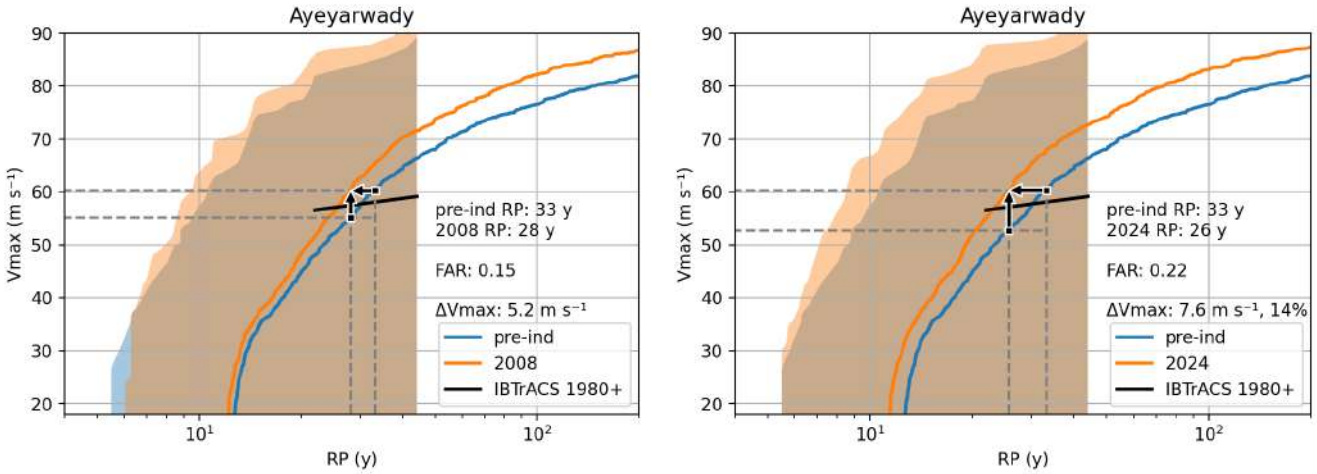

Figure 3.3: Return curves for tropical cyclones making landfall around the same region as Nargis. The orange curves show the present day climate in 2008 (left) and 2024 (right), while the blue curves show the pre-industrial climate. The black line shows the distribution of observed storms in this region since 1980.

Event	**Return period (time of event)**	**Preindustrial - 2008 (0.9 C)**		**Preindustrial - 2024 (1.3 C)**	
		Probability Ratio	Change in magnitude (m/s)	Probability Ratio	Change in magnitude (m/s)
Nargis	28	1.18	5.2	1.27	7.6

Table 3.3: Summary of results for wind speeds associated with cyclones around the landfall of Nargis.

The change in wind speed for an event like Cyclone Nargis striking southern Myanmar is clear. At the time of occurrence, such events occurred roughly once every 28 years, but prior to warming of 0.9 C would have occurred only once every 33 years. This represents an increase in likelihood of approximately 18%. Equivalently, events of a similar rarity to Nargis in preindustrial times would have been approximately 5.2 m/s slower. The change in likelihood and wind speeds between preindustrial times and 2024 is significantly larger, at 27% more likely and 7.6 m/s more intense, suggesting a further increase since the time of occurrence.

3.4.3 Sea Surface Temperatures

On average, temperatures along the track were made 0.66°C (1.19°F) warmer by human caused climate change (Fig. 3.4). Climate-driven warming did not vary much throughout the life cycle of Tropical Cyclone Nargis, staying largely between 0.6 and 0.8°C. However, there

is a slight upward trend in the warming throughout its life, as the storm moved into waters more attributably warmed by human-caused climate change.

Event	CSI (Probability ratio)		Average change in intensity
	Average	Peak	
Cyclone Nargis (2008)	1.47	2.4	0.66 °C

Table 3.4: Summary of results for SSTs associated with the track of Nargis.

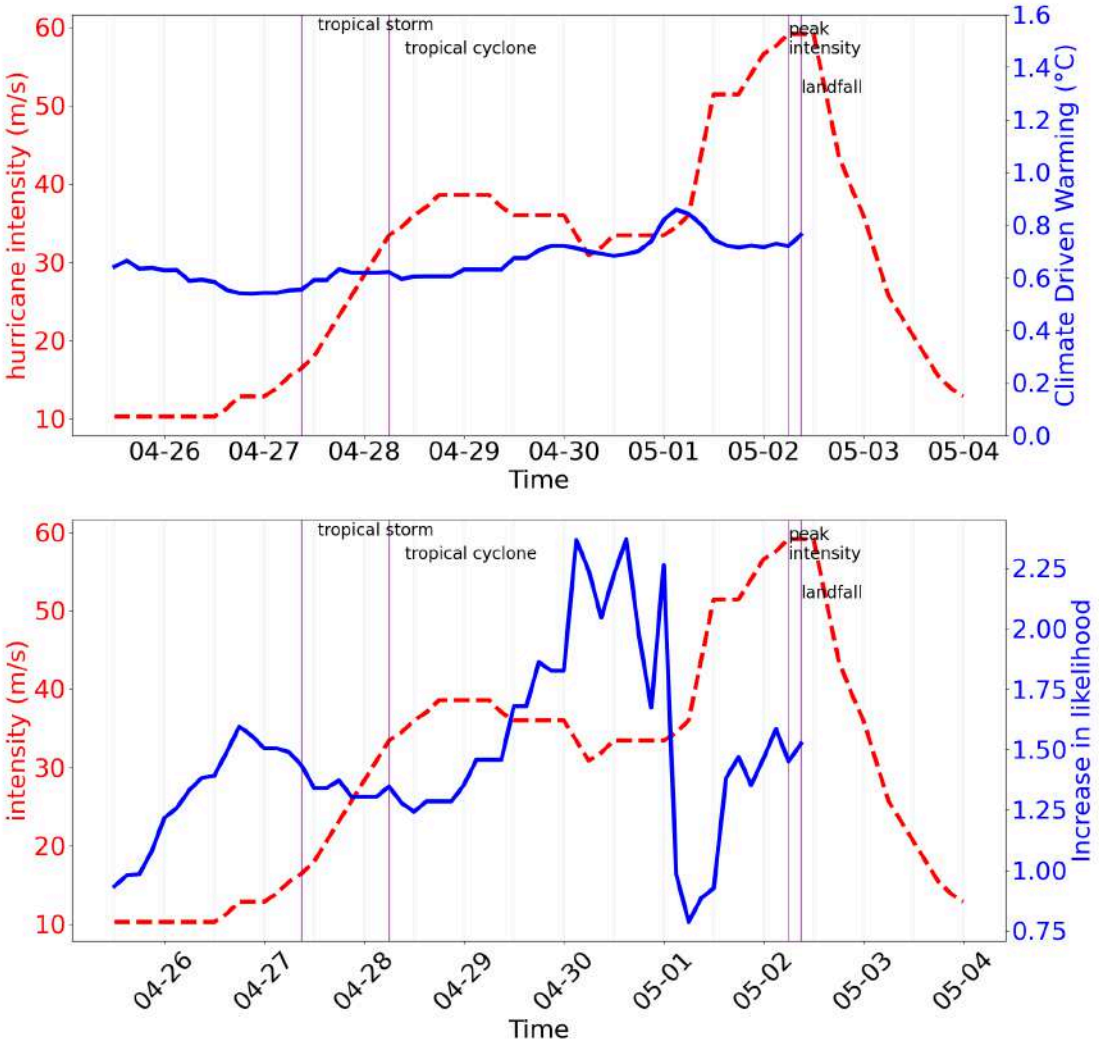

Figure 3.4: Climate driven warming (top) and increase in likelihood of sea surface temperatures occurring as a result of climate change (bottom). Data from Climate Central Ocean CSI. Additionally, both figures present intensity (as a red, dashed line).

Ocean CSI reached its highest value (2.4) on April 30th, when the storm was already a tropical cyclone and on its way to peak intensity and subsequent landfall. This indicates that the Sea Surface Temperatures which Nargis passed over were made 2.4 times more likely to occur in the climate of 2008 for that location than in a world without climate change. On average, temperatures along Nargis's lifetime from disturbance to landfall were made 1.47 times more likely to occur as a result of climate change. Although Ocean CSI values were briefly below 1 early in Nargis's lifespan, and again early on May 1st, overall, they were greater than 1, indicating that overall, the SSTs over which Nargis was passing were more likely to occur in a world with climate change than without.

Tropical Cyclone intensities and rapid intensification are strongly related to elevated Sea Surface Temperatures (e.g. Hong and Wu 2021). Increased Sea Surface Temperatures allow for higher levels of local humidity, atmospheric instability, and potential intensity (e.g. Emanuel 2006). Along Nargis's track, ocean temperatures were consistently more than 0.6°C warmer than they would have been in a world without climate change. We can thus conclude that warmer Sea Surface Temperatures along the track of Tropical Cyclone Nargis were influenced by human-caused climate change, which affected Nargis's development environment and made it more likely to intensify.

3.5 Vulnerability and exposure

Cyclone Nargis resulted in devastating storm surges reaching up to 3.6 meters, inundating extensive areas of the densely populated Irrawaddy Delta (Tripartite Core Group, 2008). The disaster has a staggering human toll, in part due to the sheer number of people living in vulnerable areas. Playing an even greater role, Myanmar's meteorological infrastructure faced significant challenges in accurately forecasting the cyclone's intensity and trajectory (Tripartite Core Group, 2008; Kyaw et al., 2018; Kyaw et al., 2021). Exacerbating the situation, the cyclone underwent a phase of rapid intensification from Category 1 to 4 and followed an unusual eastern track before making landfall (Fritz et al., 2010). Research by Howe & Bang (2017) suggests that "where and how" the cyclone hit were bigger drivers of impact than its intensity. Inadequate forecasting resulted in limited risk perception and evacuation efforts (Myint et al., 2011), which were compounded by telecommunications disruptions that hindered effective coordination (Suwanvanichkij et al., 2010).

In the affected regions, many residential structures were constructed with walls of wood and grass roofs (Howe & Bang, 2017); materials which, naturally, could not withstand the intense winds surpassing 215 km/h. The majority of the impacted population resided in conditions of poverty, faced limited access to essential resources, and engaged in climate-sensitive livelihoods such as agriculture (Warr & Aung, 2019), which exacerbated the devastation wrought by the storm.

Communities' exposure was further aggravated due to environmental degradation, particularly with the loss of mangroves (Estoque et al., 2018; De Alban et al., 2020), which serve as natural barriers against storm surges. Over time, these forests experienced significant loss due to urban development and aquaculture practices, thereby diminishing their protective functions.

Since Cyclone Nargis in 2008, Myanmar has made significant strides in enhancing community resilience against natural hazards. Key improvements include a strengthened early warning system through increased weather stations and upgraded forecasting technologies (Kyaw et al., 2018). Disaster risk reduction initiatives have been prioritised, with national policies promoting community-based preparedness, such as through rolling out public awareness campaigns to educate communities about disaster response (Min et al., 2020). Furthermore, enhanced collaboration among government agencies, NGOs, and international partners have fostered coordinated disaster responses. Additionally, adaptation strategies have been integrated into development planning, recognizing the need for resilience in a changing climate (Tun & Lassa, 2023). Finally, infrastructure enhancements for cyclone shelters, building codes, and improved drainage systems have been implemented to withstand severe weather (Thwe, 2015).

4. Russian Heatwave 2010

Key messages from Russian Heatwave:

- *The death toll was extremely high due to the compounding nature of the extreme heat and smoke from ongoing wildfires that created a dangerous situation for human health.*
- *Although the event has been studied a lot, previous attribution studies are all based on climate models alone and underestimate the role of climate change in this event*

4.1 Introduction

After the summer of 2003 which was characterised by two periods of extreme heat over much of Western Europe – one in June and another one in the first half of August – that led to more than 70,000 heat-related deaths (Robine et al., 2008) and gave rise to the first ever extreme event attribution study (Stott et al., 2004), the summer of 2010 was another devastating one for Europe. A heatwave that lasted for the whole month of July into early August and centred around Western Russia led to an estimated 55,000 deaths, a decrease in agricultural productivity by about 25%, and around $15 billion of economic damages in Russia alone (Barriopedro et al., 2011).

Meteorologically, the event was caused by a blocking situation leading to a quasi-stationary anticyclonic pressure system centred over Western Russia. While not uncommon for this region, in 2010, the blocking high was extremely intense and persistent, accompanied by temperatures more than 5°C above the long term mean (Di Capua et al., 2021, Otto et al., 2012, Barriopedro et al., 2011). Due to the devastating impacts, scientists and society wondered alike why such an extreme event was happening again, and if it could and should have been expected due to human induced climate change. With several attribution studies being published in the months and years of the event, the 2010 Russian heatwave led to the reconciliation of different methods of event attribution and catalysed the development of the field. The first study by Dole et al., (2011) assessed whether the event could have been anticipated earlier in the year, which they found was not the case., Rather than answering the question of the overall influence on climate change, the study focused on dynamic changes and thus undertook an anatomy of the event, an idea that developed into the storyline approach of event attribution focusing, for example, on analogues (e.g., Yiou et al., 2017). Other studies focused on record breaking heatwaves in Western Russia (Rahmstorf and Coumou., 2011), finding a probability ratio of 5 using data up to 2010. This difference in approaches led some to assume that two attribution studies on the same event led to opposing conclusions which was later reconciled by Otto et al., (2012). Calculating the probability ratio and the intensity change for the heatwave over Western Russia as defined by Dole et al., (2011) (see section below), Otto et al., (2012) found that human-induced climate change up to 2010 made the event three times more likely and 1°C more intense. Using the same approach as Otto et al., (2012) but with a different climate model, Watanabe et al. (2013) also found a probability ratio of about a factor 5.

Other studies also focused on the role of soil-moisture in driving the very high temperatures (Hauser et al., 2016) but finding about a factor 3 for the overall role of climate change.

All these studies used climate models and not observations to estimate the change in likelihood. Several other attribution studies using multi-method approaches found that climate models underestimate human-induced warming quite dramatically in Europe (van Oldenborgh et al., 2022). Just to illustrate the discrepancy between the published model-based studies from the years following 2010 and the changes that would be attributable now and in 2010 when using reanalysis data instead of only models, we use the same event definition used by Dole et al., and subsequently Otto et al., applied to ERA5 data in 2010: July average temperatures over a box extending [35 - 55E, 50-60N].

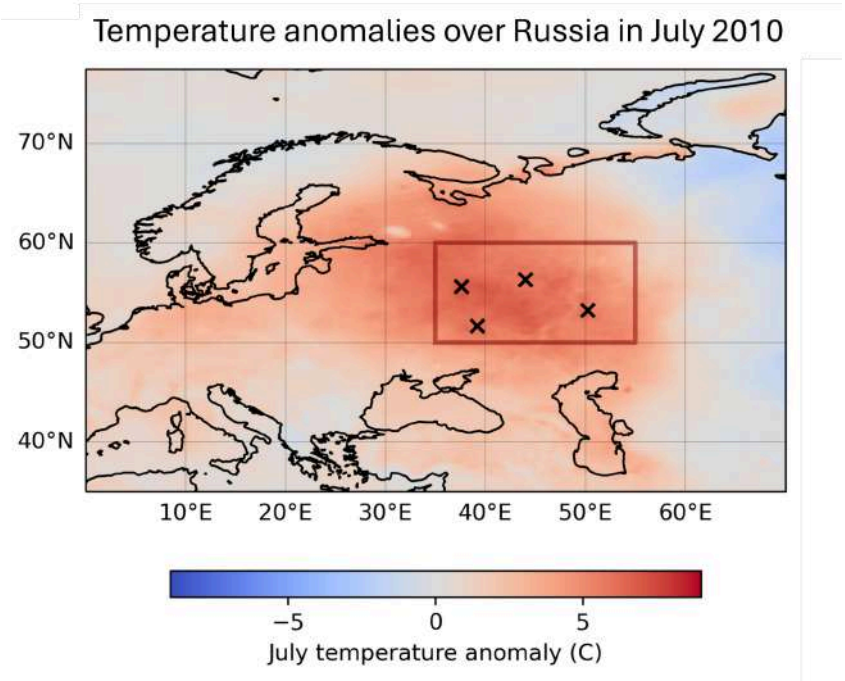

Fig 4.1 2010 July temperature anomalies with respect to 1980-2010 climatology over Europe in ERA5 data. Black crosses indicate some of the most impacted cities, Moscow, Voronezh, Nizhny Novgorod, and Samara, listed from West to East.

We use ERA5 data to estimate the return periods and changes in both the probability and magnitude of the event across the study region using the trend fitting methods described in Philip et al. (2020) (see methods). The results are summarised in table 4.1 showing that the event in 2010 is estimated to have a return time of 630 years. Using only data until 2010, we find that the likelihood of such an event to occur has been made about 83 times more likely. Similarly, the 1 in 630 is about 2°C hotter in 2010 than it would have been in a climate 0.9°C cooler than in 2010. Repeating the analysis in today's climate of 2024 that has been made 1.3°C warmer by the burning of fossil fuels the probability ratio has increased by another factor 1.7 and the intensity changed by a further 0.3°C with the last forteen years of warming.

Dataset	Return period (2010)	Preindustrial - 2010 (0.9 C)		Preindustrial - 2024 (1.3 C)	
		Probability Ratio	Change in magnitude	Probability Ratio	Change in magnitude (C)
ERA5	630 (40 - 7000)	83 (3 - 7000)	1.9 (0.3 - 4)	140 (8 - inf)	2.2 (1.1 - 4.3)

Table 4.1 *Summary of results for mean July temperature associated with the 2010 Russian heatwave*

These numbers are much higher, by more than an order of magnitude, than all the results from previous model based studies, highlighting that by only relying on models that have known difficulties in representing the observed trends in extreme heat in Europe, the role of climate change has been severely underestimated and we thus potentially understate how much the risk of extreme heat in Europe has risen by the burning of coal, oil and gas.

4.2 Vulnerability and exposure

Killing 55,000 people across the country, the record-breaking heatwave of 2010 had a profound impact on the population of Russia. While the fires claimed many lives, the smog and the polluted air also impacted human mortality, with an additional 11,000 deaths attributed to smoke from wildfires in Moscow. Though excess deaths were recorded amongst the working age population as well, people over the age of 65 were particularly affected. Those with cardiovascular, respiratory, nervous, and genitourinary diseases were found to be at a higher risk of heat-related mortality (Shaposhnikov et. al., 2014.). Further, thousands of people were displaced due to property damage from wildfires (Hunt et al., 2021).

Whilst the heatwave and wildfire smoke had a direct influence on human mortality, the preceding flash drought helped compound the impacts. Agriculture - and more specifically, wheat which accounts for 60% of total grain production - was severely affected by the extreme drought (Hunt et al., 2021). The impacts were felt beyond Russia's border, as the subsequent export ban on wheat led to an increase of global prices, which also resulted in increase poverty and bread riots in countries reliant on Russia's grain exports (Hunt et al., 2021).

At the time, Russia lacked a dedicated heatwave alert system specifically designed to warn the public about the danger of prolonged heat, nor was there a coordinated public health response to mitigate the impacts. In fact, many people flocked to lakes and rivers to cool off, leading to over 2,000 drowning deaths. According to the Russian Emergency Ministry, 95% of those drowning had consumed alcohol (BBC, 2010).

In the immediate aftermath of the June 2010 heatwave and wildfires, the President of Russia directed the Government to set up fire protection and prevention efforts, draft proposals for procuring fire equipment and design a comprehensive emergency response plan (President of Russia, 2010). These measures were largely in response to this very impactful event, but there is a dearth of information about long-term future adaptation planning in Russia.

Consequently, it remains unclear how Russia has specifically addressed heatwave risk since then but there has been dialogue among key personnel surrounding adaptation efforts across the country. Alexander Shuvalov, head of the Meteo predictive centre, indicated that the number of dangerous phenomena has increased by an average of 20 percent compared to the last decade of the twentieth century (Guryanov, 2024). In the first half of 2024 alone, 325 of the 659 recorded hydrometeorological events directly affected people's lives as noted by Vadim Petrov, Chairman of the Public Council under Roshydromet (Kedr.media, 2024).

Fallout from climate-related phenomena like the 2010 heat wave which caused damage to the Russian economy necessitates strong commitment to adaptation. Climate plans have been created in many Russian regions (Guryanov, 2024). Minister of Natural Resources and Ecology, Alexander Kozlov indicated that 59 Russian regions were ready to include climate change adaptation in their planning, construction and repair (Kedr.media, 2024; Smotrim, 2023). He emphasised that appropriate actions for flood risk adaptation would include building dams or deciding on population resettlement, constructing water pipelines for drought adaptation and strengthening underground utilities in preparation for melting permafrost (Smotrim, 2023).

5. Horn of Africa Drought 2011

Key messages from Horn of Africa drought

- Attributing the role of climate change in extreme droughts and floods in East Africa is challenging, due to high natural variability. The high number of extreme events and clear increase in frequency for some of them means however that climate change makes a difficult situation of cascading and compounding extreme weather worse.
- While early warning systems and regional disaster coordination have improved in 2024 compared to 2011, the ability for individuals and systems (natural, government, humanitarian) to fully recover from back-to-back extremes is limited.

5.1 Introduction

In the last two decades, the Horn of Africa has frequently experienced severe and prolonged droughts. The deadliest occurred in 2011. Between these droughts, extreme rainfall events caused additional impacts, impeded recovery and increased vulnerability (Kilavi et al, 2018; Kimutai et al., 2022; Palmer et at., 2023; Liebmann et al., 2014; Philippon et al., 2015; Hoell et al., 2017; Funk et al., 2018; WWA, 2020-22 Horn of Africa Drought). In 2011 (Lott at al., 2013), 2016-2017 (Uhe et al., 2018) and 2020-2023 (WWA, 2020-22 Horn of Africa Drought), prolonged drought conditions resulted in widespread impacts to humans, including through crop and harvest losses, livestock deaths, hunger, and malnutrition (WFP, 2022; MPI, 2023). In March-April-May (MAM) 2012, 2016 and 2018 (Kimutai et al., 2022) and October-November-December (OND) 2019 (FEWSNET, 2020; Wainwright et al., 2020) and 2023 (WWA, 2020-22 Horn of Africa Drought) the region experienced several heavy precipitation events again with devastating impacts on agriculture, infrastructure, settlements, property, and life. In April 2024, floods killed over 200 people and displaced over 150,000 people in Kenya. These recurring events continue to wreck developmental gains and bring hardship for communities across the region.

The 2011, 2016 and 2020-2023 drought events were marked by below normal rainfall conditions of two (2011, 2020-2023 & 2016) and five (2022) consecutive rainfall seasons (Hastenrath et al., 2011; Lott at al., 2013; WWA, 2020-22 Horn of Africa Drought). Three countries were hit hardest: Ethiopia, Kenya and Somalia. It led to severe crop failures, and harvest losses which contributed to famine in Somalia. In all cases, many refugees from southern Somalia fled to neighbouring Kenya and Ethiopia, increasing the strain on already limited resources in the drought-stricken regions of these countries. For the 2011 drought, 13 million people were left in need of humanitarian assistance, with 258,000 people reported dead in Somalia, half of whom were children under the age of five (Checchi & Robinson, 2013). In July 2011 Kenyan corporate leaders and the Red Cross Society spearheaded 'Kenyans for Kenya' initiative, fundraising to support Kenyans facing starvation from famine in Turkana County. The 2020-2023 drought was reported as the worst in 40 years (WMO, 2022, FAO 2022). At least 180,000 refugees from Somalia and South Sudan crossed into the drought-stricken areas of Kenya and Ethiopia (UNHCR, 2022). By December 2022, up to 7.1 million people in Somalia were at risk of acute malnutrition and in need of urgent humanitarian aid (OCHA, 2023). More than 1 million people had moved from their homes.

5.2 Meteorological Context

The Horn of Africa is one of the most meteorologically complex regions on the continent (Nicholson, 2017; Cook and Vizy, 2013; Rowell et al., 2015), characterised by high seasonal and interannual rainfall variability driven by complex interactions among local factors, regional circulation patterns, and remote forcings or teleconnections. The region's landscape is dominated by the Great Rift Valley, which has eastern and western branches running north to south through Kenya and Tanzania, bordered by highlands and mountains. At the core of the eastern branch lies Lake Victoria, the world's largest tropical lake, along with other smaller lakes. The valley is bounded by the Indian Ocean to the east and the dense Congo rainforest to the west, creating varied topography that influences mesoscale circulation systems. These contrasting geographical features create dynamic effects; for example, the topography disrupts uniform airflow and modulates the speed of the East African low-level jet (Bernoulli effect; Indeje et al., 2001; Nicholson, 2016). Meanwhile, lake-induced circulations generate convective nighttime storms around Lake Victoria (Anyah et al., 2006; Thiery et al., 2016).

Global climate models often misrepresent East African rainfall variability, particularly the seasonal cycle, by overestimating OND rainfall and underestimating MAM rainfall (Yang et al., 2016). This discrepancy is central to the 'East African climate paradox' (Rowell et al., 2015), where an increase in drought frequency and a general drying trend, beginning in the early 1990s have been observed (e.g., Funk et al., 2008; Liebmann et al., 2014; Maidment et al., 2015; Nicholson, 2016a; Ongoma & Chen, 2017), despite global climate model projections indicating increased rainfall (Meehl et al., 2007; Otieno & Anyah, 2012). However, signs of recovery in this dominant drying trend, particularly during the MAM season, have been noted since 2012 (e.g., Kimutai et al., 2022; WWA, 2024 East Africa floods, see Figure 5.1). Tierney et al. (2015) demonstrated that simulated El Niño-like conditions, typically associated with increased OND rainfall in East Africa, tend to overestimate annual rainfall. Batté and Déqué (2011) attributed this to the limited understanding of complex interactions between local, regional, and large-scale processes in the tropics, making model simulations less reliable. Giannini et al. (2018) argued that future rainfall projections for East Africa are affected by significant biases due to models' limited capacity to accurately simulate regional climate and trends in tropical Pacific and Indian Ocean SSTs. As a result, confidence in attributing rainfall trends to climate change remains limited.

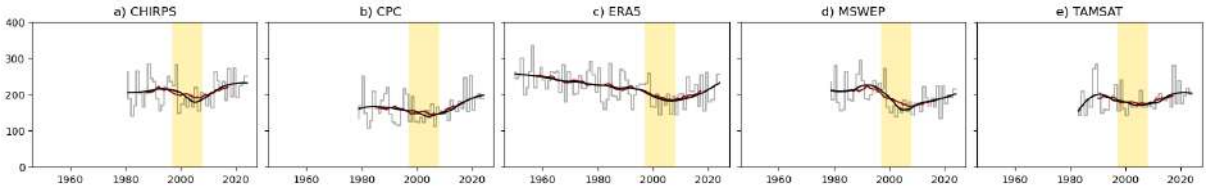

Figure 5.1: *Time series of MAM RX30day over the region most affected by the recurring droughts, interspersed with heavy rainfall from 2011 in (a) CHIRPS; (b) CPC; (c) ERA5; (d) MSWEP; (e) TAMSAT. The thick black line is a loess (local regression) curve; the dark red line is a 15-year rolling mean. The shaded region indicates the period from 1997-2008. Source: WWA, 2024*

5.3 Previous Studies

Several studies have assessed the role of climate change in the drying trends across East Africa. Lott at al., (2013) found that human influence increased the likelihood of rainfall deficits during the MAM 2011 season and not in OND. Hoell and Funk (2014) and Funk et al. (2018) attributed the drying trend from 1981 to 2016 to the intensification of the Indian Ocean branch of the Walker Circulation, driven by human-induced warming in the northwestern Pacific. Similarly, Liebmann et al. (2014) linked the MAM 1979-2012 drying trend to greater sensitivity of weather systems caused by increased zonal SST gradients between Indonesia and the central Pacific, also attributed to climate change. On the contrary, Marthews et al. (2015) and Uhe et al. (2018) found no anthropogenic influence on droughts during MAM 2014 and MAM/OND 2016, respectively, although they detected human influence on surface air temperature and net incoming radiation. Over the past two decades, however, there has been a partial recovery from the dominant MAM drying trend (e.g., Kimutai et al., 2022). Kew et al. (2021) analysed annual drought indicators including precipitation and PET for several subregions of the Horn of Africa using both observations and multiple models, finding a human-driven signal towards reduced rainfall in the southeastern part of the region (southern Somalia) but with all regions showing positive trends in PET. Soil moisture variability was found to be largely driven by precipitation rather than PET, also in dry periods, on both annual and sub-annual timescales, consistent with a water-limited regime. However, positive trends in PET could translate into actual evaporation when water becomes available, having strong implications for irrigated regions.

While there have been fewer studies on the dynamics behind flood-inducing MAM rainfall events in East Africa, the main drivers of MAM intraseasonal and interannual rainfall variability include Madden-Julian Oscillation (MJO), Indian Ocean Dipole, inter-annual tropical SST variability which largely influence zonal wind anomalies, moisture advection, and the zonal propagation of convection (Camberlin and Wairoto, 1997; Okoola, 1999; Pohl & Camberlin, 2006a; Nicholson, 2017; Vellinga & Milton, 2018). Camberlin and Wairoto (1997) found that wet spells in Western Kenya were linked to weakened easterlies, or even a reversal to westerly flow, causing anomalous convergence. Pohl and Camberlin (2006) noted that 80% of the wettest episodes in the Kenyan highlands were associated with deep convection driven by high Madden-Julian Oscillation (MJO) amplitude. Recent studies by Kilavi et al. (2018) and Finney et al. (2020) examined the interaction of low-level westerlies, the MJO, and tropical cyclones during the extreme MAM rainfall in 2018. They found that westerly moisture flux combined with an active MJO in the Indian Ocean (phases 2-4) was associated with more frequent wet spells and a greater likelihood of tropical cyclones in the southwest Indian Ocean. These studies consistently show that anomalous westerly flow over equatorial Africa is tied to a large-scale zonal pressure gradient, with higher pressure over the Atlantic and lower pressure over the Indian Ocean.

No new hazard analysis was conducted for this study; instead, we provide a summary of findings from previous work in the region (see Appendix 5.1 for synthesis plots) and a recommendation for drought studies more generally.

For the 2011 East African drought, Lott et al. (2013) found no attributable change in the 2010 OND rains, as La Niña conditions were the primary driver. However, they linked an increased risk of failure of the MAM 2011 rains to human-induced climate change. Uhe et al. (2018) found no consistent signal of human-induced climate change affecting the likelihood of low

rainfall, as observed in 2016, though La Niña and specific sea surface temperatures made such events more probable. The 2020-2022 drought analysis indicated a decline in MAM rainfall and an upward trend during OND, both attributable to climate change (WWA, 2020-22 Horn of Africa Drought). While there was no trend in 24-month precipitation, the 24-month Standardised Precipitation Evapotranspiration Index (SPEI) showed a significant increase in drought likelihood and intensity due to human influence.

There are several key takeaway messages from this review. First, combining evidence from past studies, we are confident that the deadly drought in 2011 was more intense due to human-induced climate change. However, it remains challenging to quantify this effect due to its high dependence on the exact spatiotemporal domain, season and other sources of internal variability. This conclusion is drawn from the multiple studies above finding an increased chance of low precipitation during the long rains. Furthermore, while the short rains appear to be increasing with climate change, there is also evidence that rising temperatures contribute to water balance deficits over longer time periods of multiple seasons and years, rendering the impacts of recurring droughts and floods worse.

The second takeaway message from this review is that it is important to analyse not only precipitation for drought events, but also other indices like PET, soil moisture or a drought index like SPEI to get a more complete picture of factors contributing to drought and trends therein.

Finally, and more broadly, combining information from observations and climate models remains complex, in understanding drivers of change in East African climate. This is true not only for droughts, but other impactful extreme weather events as well. In particular, Kimutai et al., 2022 found that MAM floods in 2012, 2016, and 2018 were more intense compared to the pre-industrial era driven by GMST but not statistically significant. Similarly, the 2024 MAM floods showed increased wettening but no clear signal attributable to climate change. For the OND 2023 event, both climate change and a positive Indian Ocean Dipole (IOD) contributed to its intensity (WWA, 2024 East Africa floods).

As demonstrated by these studies, alternating or compound extreme events—such as floods and droughts in different areas—pose significant challenges for risk management in the region. Repeated exposure to such extremes increases vulnerability and reduces the adaptive capacity of both natural and human systems. This underscores the importance of sustainable investments in climate-resilient development programs that incorporate climate risk management into long-term planning. Enhancing early warning systems to improve anticipatory action, readiness, and the prevention of loss of lives and livelihoods is crucial.

5.4 Vulnerability and exposure

Along with its neighbours in The Horn of Africa, Somalia is projected to experience more volatile and extreme weather patterns within the next 50 years and has experienced three major droughts in the last 25 years, (OCHA, 2020). The 2011 drought, one of the worst in East Africa and especially in Somalia where it claimed over 250,000 lives, half being children under five, and resulted in 955,000 refugees in nearby countries (OCHA, 2020).

In Somalia, the failure of two consecutive rainy seasons (Deyr - Oct to Dec 2010, and Gu March/April-June 2011) led to a decline in cereal production and livestock deaths. This was coupled with the increasing control of the militant group Al Shabab in southern Somalia which limited population movement and humanitarian access, and contributed to the withdrawal of the World Food Programme from the region (Hillbrener and Maloney, 2012).

The drought was a failure of the global food security humanitarian response system to use forecasts to anticipate the food security crisis that was unfolding in Somalia. Lessons from the 2011 drought underscored the importance of including incentives to take early action in response to an early warning (Hillbrener and Maloney, 2012). Eleven months of increasingly serious, timely, high-quality warnings were issued by FEWSNET and FSNAU, but they failed to mobilise significant early action until after a Famine was declared in July 2011 (Hillbrener and Maloney, 2012).

Since the droughts of 2011 and also 2016-17, a drought anticipatory action framework has been designed by humanitarian partners, in collaboration with the federal government of Somalia (OCHA, 2021). This framework uses food security projections disseminated every quarter by the Somalia Food Security and Nutrition Analysis Unit and FEWS NET (OCHA, 2021). Food Security Phases within the Integrated Food Security Phase Classification (IPC) are used as proxy indicators for worsening conditions across sectors and determine whether there is increased risk of an extraordinary crisis (OCHA, 2021).

The framework was first triggered in June 2020 when projections indicated that 22% of the population would face at least crisis-levels of food security and triggered again 2021 (OCHA, 2021). Somalia's drought anticipatory action framework has a trigger mechanism that relates to the forecast of the hazard following which various pre-agreed activities are implemented through the release of pre-agreed finance (OCHA, 2021). These include activities that prevent or mitigate the potential impact (e.g. sustain water study, livestock and food production etc.), and activities that stabilise and protect vulnerable people and contain worsening conditions (e.g. prevent disease outbreaks, keep children in school etc.)OCHA (2020).

6. Typhoon Haiyan Philippines - 2013

Key messages - see section 2

6.1 Introduction

Typhoon Haiyan (known in the Philippines as 'Yolanda') was first classified as a tropical depression in the western North Pacific basin on November 3rd 2013. It moved westwards under the influence of a subtropical ridge while undergoing rapid intensification as it approached the Philippines (Joint Typhoon Warning Centre, 2013a). It reached a peak intensity on November 7th with 1-minute sustained winds of approximately 196 mph (JWTC, 2013b), equivalent to a high category 5 event on the Saffir-Simpson scale, prompting discussion of introducing a 'category 6' (Lin et al., 2014). As it approached landfall, many parts of the Visayas and particularly the eastern islands of Leyte and Samar experienced storm surges of up to 5 metres, causing devastation across the archipelago and especially in Tacloban City, situated at the head of the Gulf of Leyte (Reliefweb, 2014).

In total, the storm killed over 6000 people, injured almost 30000 and displaced over 4 million (Lagmay et al., 2015; Lum and Margesson, 2014). It also led to the widespread destruction of infrastructure and housing in coastal areas, destroying or damaging over a million homes, and disrupting crucial services for months (Lagmay et al., 2015; Yi et al., 2015; USAID, 2014), as well as severely disrupting the valuable coconut farming sector, in which local farmers had no crop insurance largely due to its cost (Serino et al., 2021).

6.1.1 Evidence on links to climate change

To date, research suggests that there has been a slowdown in translation speed (Yamaguchi and Maeda, 2020a), as well as a poleward (northward) shift in storm tracks (Yamaguchi and Maeda, 2020b; Kossin et al., 2016). Assuming all other factors are equal, this poleward shift may lead to fewer TCs landfalling in the Philippines and a corresponding increase around southern Japan and Korea (Seneviratne et al., 2021). However, no trend in landfall rate has been found to date (Cinco et al., 2016) and there are many other potential and highly relevant influences of climate change on TC hazards in the basin that remain unexplored.

Over the basin, the majority of attribution studies on TCs indicate increases in likelihood and intensity due to anthropogenic climate change. First, the accumulated cyclone energy in the 2015 season was found to be linked to high sea surface temperatures in the eastern and central Pacific (Zhang et al., 2016). In turn, it increased in likelihood significantly due to anthropogenic climate change. In 2019, Typhoon Hagabis brought extreme rainfall to the Tokyo region of Japan. Across all sources of extreme rainfall in the region, the amounts associated with Hagabis were 15-150% more likely to occur because of human induced climate change. This in turn was linked with an increase of approximately US$4 billion in damages (Li & Otto, 2022). In accordance with this, a storyline approach to extreme attribution found that rainfall from the typhoon was amplified by around 11% due to human-induced warming across the atmosphere and oceans (Kawase et al., 2021). Similarly, in early August 2009, Typhoon Morakot made landfall in Taiwan, causing extreme

rainfall. The previous 20 years of anthropogenic forcing accounted for an increase of approximately 3.5% in the rainfall total (Wang et al., 2019).

More recently, the rainfall from Typhoon Gaemi in Taiwan was found to have become about 14% more intense, while in the Philippines the observed increase was around 12% but both observations and models were too uncertain for an attribution statement to be made. Additionally, the wind speeds from Gaemi were enhanced by around 4 m/s (WWA, 202 Typhoon Gaemi). In 2020, central Vietnam experienced a series of typhoon-induced extreme rainfall events leading to severe impacts, but a study found that anthropogenic climate change had no detectable influence on the rainfall from consecutive events when they struck Vietnam (Luu et al., 2021).

6.2 Hazard attribution

Several studies have considered the influence of climate change on the intensity of Typhoon Haiyan, in both present day and hypothetical future climates, and through multiple mechanisms. First, increases in sea surface temperature (SSTs) decrease the minimum sea level pressure and increase cyclone intensity. However, this is offset by changes in atmospheric air temperature across the vertical profile, and relative humidity that is important for cloud formation, though the physical mechanisms behind this are not fully understood. It is unclear which effect is larger; two studies indicate that the influence of SSTs is the dominant effect (Takayabu et al., 2015; Nakamura et al., 2016), pointing to overall likely increases in the intensity of storms like Haiyan. However, another demonstrates that these results can be both storm- and model-dependent, leaving the influence of ACC on Haiyan's intensity unclear (Wehner et al., 2019). In particular, in this study, use of both global and regional atmospheric model analysis explicitly found different net influences of climate change on the intensity of Haiyan.

As a result, the signal of climate change on storm intensity is uncertain and difficult to quantify. However, new studies and the breadth of attribution literature for TCs in the wider basin suggest that a signal is emerging. Using a 'pseudo-global warming' approach, Delfino et al. (2023) found that the maximum winds from Haiyan were increased by 2 m/s relative to preindustrial times (alongside similar increases for Typhoons Bopha and Mangkhut). Using a completely different approach, the stochastic storm model IRIS gives an increase of 3 m/s for Haiyan due to human-induced warming (Sparks & Toumi, 2024a; Sparks & Toumi, 2024b). Furthermore, in addition to intensity as described above, Takayabu et al. (2015) also considered the effect of the change in intensity of Haiyan on its storm surge, which in turn drove many of the impacts. This concluded that the storm surge was likely 20% higher due to climate change. While the quantification itself remains uncertain for the reasons described above, this analysis shows explicitly that if climate change did enhance the intensity of the storm, the storm surge also would have been enhanced.

To summarise, while analysis of the mechanisms driving Haiyan show different contributions from climate change, recent work using multiple methods suggests a small but increasing trend in intensity, which in turn likely drove a higher storm surge. Furthermore, all of the attribution studies of TCs in the basin to date point towards enhanced rainfall from similar storms. This is also in line with well-established thermodynamic arguments. It is therefore

with medium confidence that we can say that climate change increased the rainfall and intensity of Haiyan, and in turn its storm surge, though quantifying this remains challenging.

6.4 Vulnerability and exposure

Typhoon Haiyan was one of the most powerful super typhoons ever recorded, with up to 314 km/h in 1-minute sustained winds (Singer, 2014; International Charter Space and Major Disasters, 2013). It generated storm surges of about 5 metres, with up to 7.5 metres peaks in some coastal towns like Tacloban city, Leyte Province, accounting for more fatalities and extensive damage than the wind factor (Morella, 2018; Sherwood et al., 2014).

Authorities have also admitted that few understood the warnings - specifically the term “storm surge” - underestimating the severity of the impending flooding which led to insufficient evacuation from highly populated, low-lying coastal areas (Morella, 2018).

Deep poverty, unplanned coastal development and growth of informal settlements were major drivers of vulnerability and exposure to flood risk within the communities in Haiyan’s path, as much of the population made livelihoods in farming and fishing and settled along the narrow coastal plains of the islands (Morella, 2018). Earning low incomes meant that the population built shacks or weak, wooden housing structures which were easily destroyed by the typhoon (Morella, 2018; International Charter Space and Major Disasters, 2013).

Haiyan underwent rapid intensification shortly before landfall, giving authorities limited time to adjust and roll out early actions, and because of the lack of hurricane-grade shelters, many of those evacuated were still in structures that were vulnerable to storm surges and strong winds (Morella, 2018). The archipelagic geography of the Philippines in addition to destruction of key transportation infrastructure such as roads and airports, and disruption to communications, further complicated the roll-out of humanitarian aid (ECHO Factsheet, 2014; Sherwood et al., 2014).

Since the disaster, the government has worked with linguists on crafting simpler warning messages for typhoons, landslides, floods and other related phenomena for greater reach and understanding from populations with varying languages across regions in the Philippines (Morella, 2018). Emphasis has also been placed on building back better and greener. The International Labour Organisation (ILO) through its projects supported local communities in making interlocking compressed earth blocks with resistance exceeding the UN standard for shelter construction after natural disasters (ILO, n.d.). This intervention is termed as building back better and greener because the blocks are produced using limestone soil instead of sand, making them more solid than concrete blocks and preserves the natural resource and the islands’ beaches (ILO, n.d.).

Similarly, building local capacity in long-term adaptation to similar shocks became a central focus following Haiyan. Some individuals whose local water sources and sanitation systems were destroyed were taught how to build biogas digester septic tanks to produce potable household water (ILO, n.d.). Hence, in future, those trained can simultaneously diversify their livelihoods and increase community resilience by using these skills to build similar low-cost water supply and sanitation systems in other areas (ILO, n.d.).

7. Uttarakhand Flood 2013

Key messages from the Uttarakhand Flood, 2013:

- *The new analysis complements earlier attribution studies by combining observation data with high-resolution climate model outputs. The results indicate that anthropogenic climate change has made a heavy rainfall event like the one in Uttarakhand, India, in 2013, twice as likely and about 11% heavier.*
- *The devastating impacts are also linked to the exposure of people and assets on steep hillsides, and new construction that destabilised natural drainage pathways. This all occurred during the pilgrimage season, putting more people in harm's way.*

7.1 Introduction

In mid-June 2013, the state of Uttarakhand in northern India was hit by a cloudburst that led to heavy downpours that lasted for roughly four days. On June 17, the state recorded an average rainfall that was more than 4.5 times the daily average (65.9 mm). During 13-19 June, the heavily impacted Kedarnath region received more than nine times the precipitation, compared to average conditions (Dube et al., 2014). The heavy rainfall spell caused flash floods, several landslides, and also resulted in bursting the moraine-dammed Chorabari lake located above Kedarnath town (Das, 2013). Around 6,000 lives were lost (EM-DAT) and costs of around £480 million (Jogesh et al., 2016) were incurred in infrastructure damage. This includes 144 bridges, 1636 roads, 19 hydropower projects and over 4200 affected villages (Das, 2013). While the triggering cloudburst and heavy rainfall are probabilistic natural disasters the high death toll is also strongly influenced by anthropogenic activities such as mismanagement in construction, tourism and economic activities such as intensive mining which increased the intensity and magnitude of the damages (Kala, 2014).

Meteorologically, the extreme rainfall event was caused by a combination of cold air intrusion of polar origin, an unusual incursion of a mid-latitudinal westerly, a low pressure system over the Bay of Bengal, and orographic uplift in the Himalayas (Joseph et al 2014, Singh et al 2014, Ranalkar et al 2016). Incidentally, snow cover in the local river basins was approximately 30% above average in early June 2013. The impacts were exacerbated by rapid snowmelt in these basins that overwhelmed the regional hydrological system and eventually led to the bursting of the Chorabari dam (Kala, 2014, Durga et al 2014).

Climate change is already affecting the lives of millions of people in Uttarakhand through a combination of increased vulnerability due to climate-sensitive socio-economic sectors (agriculture, fisheries, forest-based industry) and changes in the prevailing climatic conditions (UAPCC, 2015). According to the Comptroller and Audit General of India Report No. 5, excessive rainfall and landslides caused more than 50% of the human casualties in Uttarakhand between 2008 and 2013. These numbers highlight the consequences of extreme rainfall spells such as the 2013 event on vulnerable communities in Uttarakhand and underpin the need for understanding the role of climate change in such events to help adaptation and mitigation.

7.1.1. Past studies

To answer the question of whether and to what extent climate change played a role in this event, a number of studies in the past have assessed the event in the context of extreme event attribution. The first study by Singh et al. (2014) contextualised the event as a 1-in-100 year event in terms of the total June precipitation. By comparing the likelihood of such an event between the pre-industrial and historical (20CR) runs from 11 CMIP5 models, the study concluded an increase in likelihood of such events attributable to human-induced climate change. A subsequent study by Cho et al. (2015) using observations, 10 global climate models and regional modelling experiments found that approximately 80% of the rainfall during the five days of the storm in June 2013 can be attributed to post-1980 climate trends found in the observations, which in turn is driven by increase in greenhouse gases and aerosols. On the other hand, the next study by Kumari et al. (2019), underscored the role of cooling from reflective aerosols in the atmosphere (e.g., Schaller et al. 2018) in counteracting the wettening tendency due to the warming from the greenhouse gases in the likelihood of extreme rainfall, based on one model- the weather@home - a high-resolution large ensemble modelling experiment using Hadley Centre's HadAM3P global model driven with the regional model HadRM3P. Overall, these studies suggest an increasing tendency towards more frequent and intense extreme rainfall as the world continues to warm and postulate the effects of atmospheric aerosols in addition to the greenhouse gases in influencing the trends. However, all three studies used a fixed-model approach in which the observations were only used to derive the return period of the extreme event and to evaluate the climate models.

In this study, we revisit this event using the WWA methods, which allows us to combine information from observations and newly available high-resolution climate models for drawing overarching conclusions. Our aim is to quantify the role of climate change in the event as it occurred and assess whether there are discernible changes if such an event were to occur in today's climate.

7.1.2. Event definition

To describe the extreme rainfall spell that caused the catastrophic flooding, we adopted a similar event definition to that used in the attribution study by Kumari et al. (2019). We use the same temporal definition as in the cited study, and characterise the 2013 event by the maximum 4-day accumulated rainfall (rx4day) in the early monsoon (JJA) season over Uttarakhand. This includes the months with the heaviest rainfall, July and August (Kala, 2014), as well as June – the month in which the climate extreme occurred. For the spatial extent, we use a slightly modified study region (highlighted in red in Fig. 7.1) focusing on the topographically homogeneous western part of the rectangular domain spanning 77°-82° E and 28°-32° N that was used in the original study (shown in dashed grey in Fig. 7.1). The adjusted domain excludes the mountainous Himalayan region, capturing only the worst-impacted areas. Additionally, the modified study region avoids model biases at higher elevations arising from the model physics (Ghimire et al, 2015; Shahi, 2022) and a potential underestimation of precipitation due to sparse observational sites (Andermann at al., 2011).

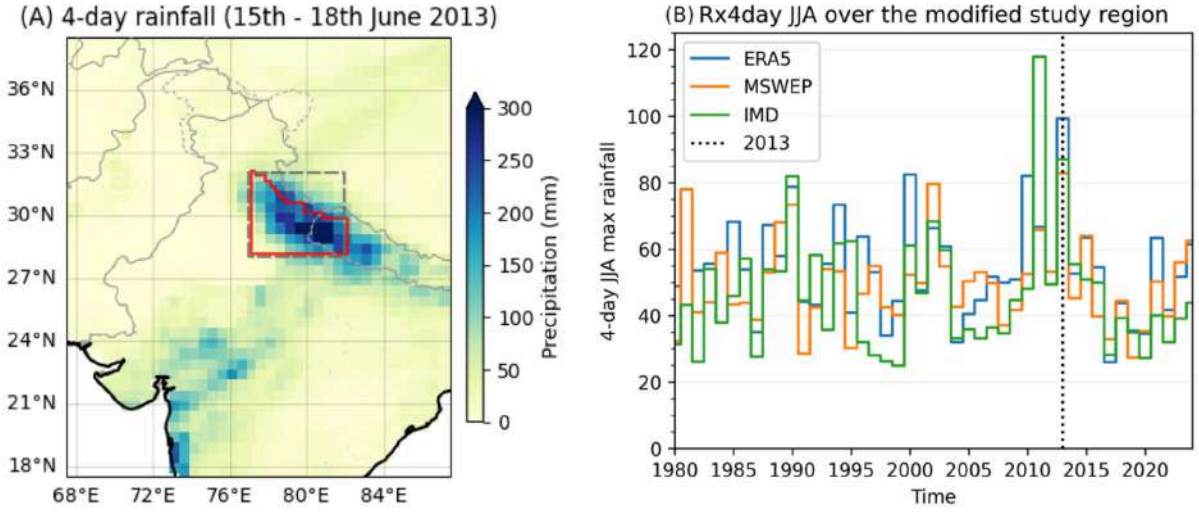

Figure 7.1: Event definition for the Uttarakhand flood. Panel (A) shows the accumulated 4-day precipitation over the modified study region (shown in red), which approximately covers the Uttarakhand region. The original study region is shown in dashed grey. Data from ERA5. Panel (B) visualises rx4day for JJA averaged over the modified region as a time series from 1980 to 2024. The extreme event value in 2013 is indicated by a dashed line.

7.2. Observational analysis

Using three independent datasets- ERA5, MSWEP and India Meteorological Department's station-based gridded data IMD (details about these datasets are provided in Appendix A.1.1), we calculated the return period of the event in the year 2013 when it occurred, as well as in the year 2024, along with changes in likelihood and intensity of extreme rainfall spells such as this event due to global warming since the pre- industrial era. The results are summarised in Table 7.1. In the year 2013, the best estimated return periods of the event are 66, 22 and 110 years in the IMD, ERA5 and MSWEP datasets respectively. In 2024, the 2013 event would have occurred once in 100 years based on the IMD dataset and once in 36 and 110 years in the ERA5 and MSWEP datasets. The near-similarities in these estimates for the 2013 and 2024 climates is reflective of the extreme nature of this event. For the attribution analysis, therefore, we define this event to be a 1-in-100 year both in the 2013 climate as well as in the 2024 climate; this is also in line with the return period for the event reported in previous studies (Singh et al., 2014; Kumari et al., 2019). The Probability Ratios (PR) and intensity changes based on IMD dataset reveals a near- doubling in the likelihood of the 2013 event due to climate change and a 7.2% increase in the amount of rainfall associated with the event. The shorter MSWEP dataset also shows the same direction of change but stronger with a PR of 590 and intensity change of 36%. In the ERA5 data, the PR is 0.8 with a decrease in intensity of 2.9%, meaning that there is no discernible climate change signal on the event in this data.

In the years since 2013, extreme rainfall spells in the JJA season in the study region have been seemingly precipitating less as compared to the past (see Figure 7.1(b)). This is reflected in the PR and intensity changes of this event between the 2024 climate and the pre-industrial climate, as shown in Table 7.1. The best-estimated PRs are less than 1 for the IMD and ERA5 datasets with decreases in intensity of 3.5% and 11% in the respective

datasets. The strong climate change signal in the MSWEP dataset in the 2013 vs. pre-industrial climate instance is substantially weakened now with a best estimated PR of 1.4 and a 2.7% increase due to climate change. The uncertainty range of the synthesised observed trends has become smaller between 2013 and 2024, but both clearly encompass no change.

Dataset	**Return period (2013)**	**Preindustrial - 2013 (0.9 C)**		**Return period (2024)**	**Preindustrial - 2024 (1.3 C)**	
		Probability Ratio	Change in magnitude (%)		Probability Ratio	Change in magnitude (%)
IMD	66 (14 ... 1.6e+4)	1.9 (0.17 ... 2.8e+3)	7.2 (-20 ... 59)	1.0e+2 (25 ... 2.1e+6)	0.73 (0.059 ... 3.3e+2)	-3.5 (-27 ... 29)
ERA5 (1950-2013)	22 (8.3 ... 1.3e+2)	0.82 (0.12 ... 17)	-2.9 (-25 ... 30)	36 (13 ... 2.6e+2)	0.43 (0.061 ... 2.4)	-11 (-30 ... 11)
MSWEP	1.1e+2 (20 ... ∞)	5.9e+2 (1.5 ... 3.5e+10)	36 (1.5 ... 91)	1.1e+2 (19 ... ∞)	1.4 (0.014 ... 1.4e+6)	2.7 (-25 ... 44)

Table 7.1: Return periods, and change in probability ratio and magnitude for extreme rainfall associated with the flood in India for the study region, due to GMST. Light blue (orange) indicates a wetting (drying) trend that crosses no change, dark blue indicates a statistically significant wetting trend.

7.3. Hazard Attribution

In addition to the observed data, two sets of climate models that have reasonably high resolution and passed the model evaluation criteria (see section A.1.5)- namely, CORDEX (five out of nine models) and HighResMIP (seven out of fourteen models) were used for estimating the change in likelihood and intensity of 4-day extreme rainfall in the study region attributable to climate change. The details of these models are provided in Appendix A.1.2. Figures A.6.1-A.6.4 shows the seasonal and spatial patterns for the climate models against those from the observed data. The overall rating for these models based on their ability to capture the observed seasonal and spatial patterns and the statistical distribution are summarised in Table A.6.1.

Figure 7.2 shows the changes in probability (Probability Ratio) and intensity based on the observations, models and from combining them both. The numbers are also summarised in Table 7.2. The synthesised results based on the observations show an overall increase in the likelihood and intensity of events such as the one under study between the pre-industrial climate and the climate of the year 2013 when it occurred. The PR is approximately 10 which implies that there was a factor of 10 increase in the likelihood of such events in 2013 due to climate change till then, and with a 12% increase in the intensity. Including the information from the additional years of data since 2013 reduces the magnitude of the trends across all datasets on account of these years recording lesser magnitudes as compared to the past. Consequently, the synthesised results based on observations between the 2024 climate and the pre-industrial climate shows an overall decrease- with a PR of 0.76 and a 4.2% decrease in intensity of rain. These differences are a reflection of caveats in the independent datasets used in this study. A closer examination of the numbers from the individual datasets (see

Table 7.1) shows that the overall changes are driven by one of the datasets, MSWEP, that shows a higher change; the other two datasets, one of which is based on station data (IMD), register smaller departures.

The climate models are consistent in the direction of change, with the majority of the models showing an increasing trend in extreme rainfall events in the region attributable to climate change (A.6.3). The large uncertainties in the observations translates into lower confidence in them and therefore, the overall synthesised results are largely driven by the models. The best-estimated PR and intensity changes are 1.97 and 11.4% between the pre-industrial climate and the 2013 climate, and statistically significant. These numbers are consistent with the physical relationship described in Clausius-Clapeyron theory that with every 1C warming of the atmosphere, the moisture holding capacity increases by 7%, which also reflects in the extreme rainfall amounts. Including the additional years of data does not change the best estimated PR and intensity change, with events such as this one becoming 2.03 times more likely and 11.1% more intense between today's climate and the pre-industrial climate. However, contrary to expectation, the uncertainty bounds in the climate models (red bars in Figure 7.2) are found to increase despite the inclusion of additional data points rendering these estimates to be no longer statistically significant. This is an artefact of the estimates from some of the climate models included in the analysis incurring uncertainties from intermodel spread; regardless, this does not affect the confidence in our findings.

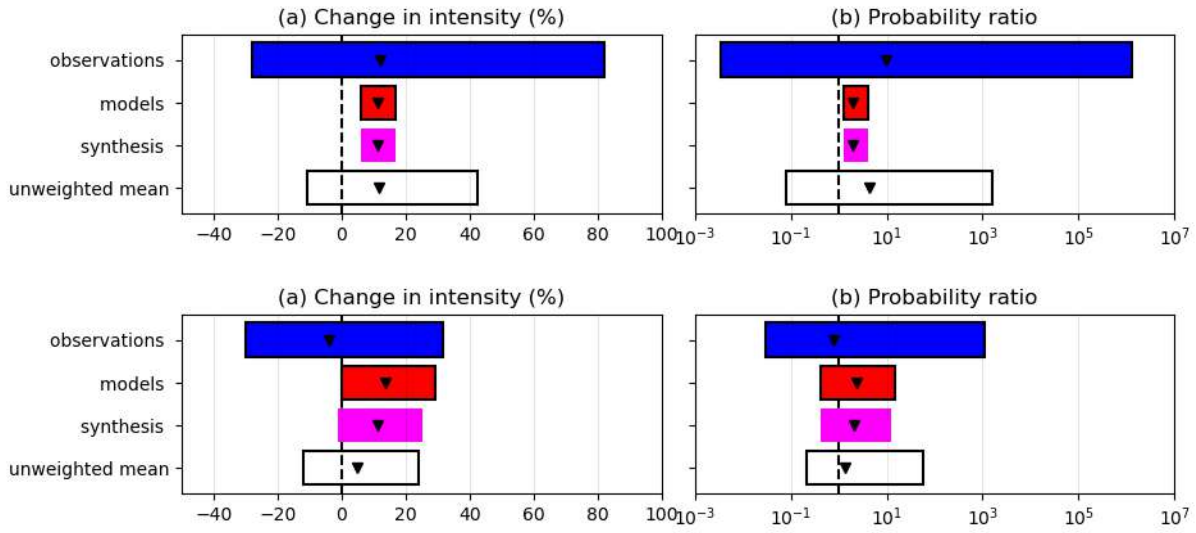

Figure 7.2: Synthesised changes for a 100-year 4-day JJA maximum rainfall event over Uttarakhand, India, due to GMST. Changes in PR (left) and intensity (right) are shown for two historical periods: comparing the climate at the time of occurrence with a past 0.9°C cooler climate (top row) and comparing the present 2024 climate with a 1.3°C warmed climate (bottom row).

Dataset	**Preindustrial - 2013 (0.9 C)**		**Preindustrial - 2024 (1.3 C)**	
	Probability Ratio	Change in magnitude (%)	Probability Ratio	Change in magnitude (%)

Observations	9.72 (3.43E-03 … 1.33E+06)	12.2 (-28.1 … 82)	0.757 (0.0296 … 1.13E+05)	-4.2 (-30.2 … 31.7)
Models	1.96 (1.25 … 4.17)	11.3 (5.86 … 16.9)	2.28 (0.421 … 14.7)	13.8 (0.0726 … 29.3)
Synthesis (weighted)	1.97 (1.26 … 4.17)	11.4 (5.9 … 16.9)	2.03 (0.431 … 12.7)	11.1 (-1.39 … 25.1)

Table 7.2: Summary of results for extreme precipitation associated with the flood in India (shown in Figure A.6.1): changes due to GMST include preindustrial-2013 changes and preindustrial-2024 changes. Statistically significant increases (decreases) in probability and intensity are highlighted in dark blue (orange), while non-significant increases are highlighted in light blue (light orange).

7.4 Vulnerability and exposure

When it comes to the 2013 floods in Uttarakhand, vulnerability of the population was exacerbated by an interplay of a variety of factors. As a result of unplanned and rapid urbanisation, construction of homes, hotels and roads in fragile hillside areas and along riverbanks with limited drainage systems left many people exposed to flood risk (Ziegler et al., 2014; Rautela, 2018). At the time, the region also saw several hydroelectric power projects, dams, and tunnels being put into operation or under construction. This, in turn, destabilised natural ecosystems by altering river courses and removing protective vegetation, exacerbating the intensity of the flooding - which has subsequently been described as a “Himalayan Tsunami” (National Institute of Disaster Management, 2013).

Although the Indian Meteorological Department issued early warnings of heavy rainfall, these were not sufficiently specific and had limited coverage (Lindell et al., 2019). Further, the floods and landslides struck at the height of the pilgrimage season in the state, when hundreds of thousands of pilgrims were visiting sacred sites like Kedarnath, Badrinath, and Gangotri (Ziegler et al., 2014; Kala, 2014). When the floods and landslides hit, many of these were trapped, leading to high casualties. With thousands also stranded in the mountainous areas, there were limited evacuation routes available. Additionally, many evacuees refused separation from family members (Rautela, 2018). This, in addition to washed-out and destroyed roads, complicated both early action and emergency response.

Following the floods, enhanced flood forecasting systems and satellite-based data integration were prioritised to improve early warning accuracy (Patel et al., 2022). Geotechnical measures, such as bioengineering and erosion control structures, were implemented to stabilise landslide-prone slopes (Ghosh & Pal, 2017). Stricter land-use policies now also limit construction in high-risk zones, addressing governance issues around unregulated urban development (Dash & Punia, 2019). Further, disaster preparedness training and resilient infrastructure designs, such as elevated roads, aim to reduce risk (Kansal & Singh, 2022). Finally, improved coordination among sectors involved in emergency response and spatial planning supports the enforcement of these measures (Dash & Punia, 2019).

8. European Heatwaves 2015, 2022 & 2023

Key messages from European Heatwaves:

- *The death toll from these events reflects the combination of quickly rising temperatures across Europe, an increasingly vulnerable population as the continent ages, and existing building stock and infrastructure not built for the hotter climate. While Europe has made considerable progress in developing Heat Action Plans and Heat-health Early Warning Systems, they have not been able to outpace the increases in the hazard, vulnerability and exposure.*
- *A large number of attribution studies exist for heatwaves in Europe, but climate models underestimate the observed warming, so the results are probably conservative estimates of the role of climate change.*

8.1 Introduction

Heatwaves are amongst the deadliest natural hazards with thousands of people dying from heat-related causes each year. However, the full impact of a heatwave is rarely known until weeks or months afterward, and in many regions may never be known at all, due to poor record-keeping. Of the ten deadliest disasters recorded in the EM-DAT database (https://www.emdat.be/), three are heatwave events that affected large regions of Europe, causing 3,275 recorded excess deaths in France in 2015; over 53,000 excess deaths across the continent, from Portugal to Romania, in 2022; and over 37,000 excess deaths in central and southern Europe in 2023. Here, we review existing attribution studies about the three events mentioned above as well as similar events across the European continent. However, we note that it is likely that heatwave mortality rates are even higher in other parts of the world, particularly the global south, but are unreported (eg. Gasparrini et al., 2015).

8.2 Previous attribution studies

Even before the full impacts were evident, each of these heatwave events was deemed significant enough at the time to be the subject of a World Weather Attribution rapid attribution study, and most have subsequently been analysed in more detail in peer-reviewed papers. A rapid study on the 2015 heatwave examined changes in three-day averages of daily maximum temperatures recorded at stations at de Bilt, Madrid, Mannheim, Beauvais and Zurich and found that the likelihood of observing temperatures as high as those recorded in July 2015 was at least four times higher in 2015 than it would have been in around 1900 (Sippel et al., 2016); comparison of simulated temperatures in the current climate and in a climate without anthropogenic warming, using the 'weather@home' model, found that in three of the five cities, similar heatwaves were at least twice as likely to occur in the current climate as in a world without climate change. This analysis was later peer reviewed, and the authors noted that the climate model that they used exhibited a warm, dry bias; even after bias correction the model simulated a substantially smaller increase in annual maximum 3-day temperatures than the observations (Sippel et al., 2016).

The June 2022 heatwave generated particular interest in the UK, where temperatures in excess of 40°C were recorded for the first time. A rapid attribution study looked at 1- day

maximum and 2-day mean temperatures over the rectangular domain 3.5W-0.5E, 51.25N-54N in the ERA5 reanalysis product (WWA, 2022 United Kingdom Heatwave; domain 1 in Figure 8.1). The hottest day of the heatwave was estimated to be a 1-in-1000-year event in the observations, and around 500 times more likely to occur than in a preindustrial climate. The hottest 2-day period (averaging over daily and nightly temperatures) was estimated to be a 1-in-100-year event, and nearly 50,000 times more likely to occur than in a preindustrial climate. The annual maximum temperatures over the region were found to be 3.6°C warmer due to 1.2°C of global warming, and the hottest two-day spell each year was found to be 4.0°C warmer. Climate models again showed a weaker signal than the observations, with an average increase of just under 2°C in both events; the probability ratio was 100 for one-day maxima and around 10 for maxima of two-day temperatures. Overall, because of the difficulty of estimating probability ratios for such extreme events, the best estimate of the probability ratio was not communicated. Instead the lower bound was used to give a conservative but robust estimate of the contribution of climate change, which increased the likelihood of seeing similar daily maximum temperatures by a factor of at least 9, and the likelihood of seeing similarly warm two-day periods by a factor of at least 17. No synthesised change in intensity was reported because the numbers from the observations and models were so different. An independent analysis of June average temperatures over a larger area of northwestern Europe (domain 2 in Figure 8.1) found that the likelihood of extreme June temperature anomalies (defined as more than 4.1°C above the 1901-1930 mean, the previous record anomaly) had been increased by a factor of 136 by human-caused warming (UK Met Office, 2022). Prior to this event, a separate study had found that summers with at least one day above 40°C somewhere in the UK were likely to occur once every 100-300 years in the current climate compared to a return time of thousands of years in a preindustrial climate (Christidis et al., 2020).

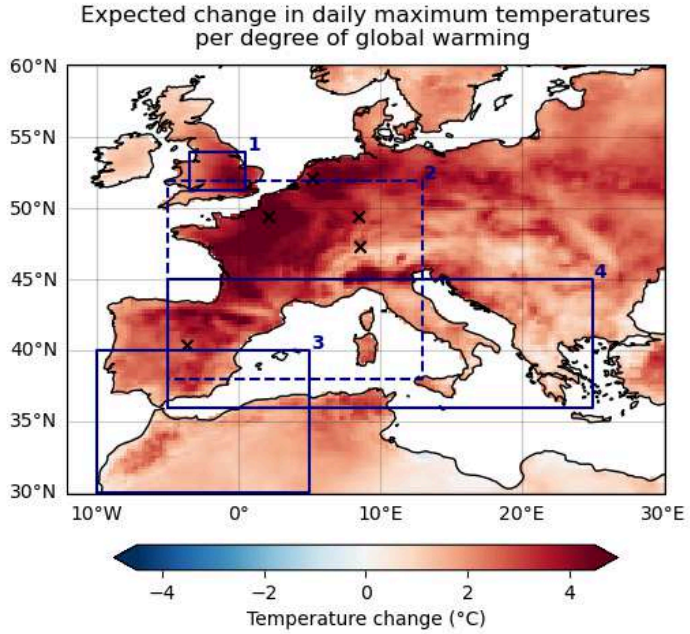

Figure 8.1: *Map of expected change in annual maximum daily temperatures in Europe per 1°C change in global mean temperatures (ERA5), showing the study regions discussed in this section.*

1: WWA UK heatwave study, 2022; 2: Met Office heatwave study, 2022; 3: WWA Southern Mediterranean heatwave study, April 2023; 4: WWA southern Europe study, July 2023. Black crosses indicate the cities included in the 2015 study.

Two major heatwave events occurred in 2023. The first of these was in the West Mediterranean region in April, months before the usual summer peak temperatures and therefore months before people and the environment had begun to acclimate to warmer temperatures. Local temperatures were around 20°C above the seasonal average and April temperature records were broken by as much as 6°C. A World Weather Attribution rapid study (WWA, 2023 Western Europe and North Africa Heatwave) examined April maxima of 3-day temperatures over Spain, Portugal, Morocco and Algeria from 10W-5E and 30N-40N (domain 3 in Figure 8.1). According to ERA5 reanalysis data, such high temperatures had a return period of around 400 years, and were at least 15 times more likely to occur in the current climate than in a climate without anthropogenic warming. The warmest April temperatures were found to have increased by around 3.5°C. Once again, the climate models exhibited a smaller but still clearly positive trend, with the warmest April days 1.5°C warmer in 2023 than in a 1.2C cooler climate; the upper bound of this estimate (1.8°C) just overlaps with the lower bound of the estimate from ERA5 (1.7°C). To avoid placing too much weight on the more conservative climate models, the unweighted mean of the models and observations was used to report an overall attributable increase of 2.5°C (95% confidence: 1.6 to 3.4°C) in similar temperatures due to anthropogenic warming.

The second European heatwave event of 2023 occurred in early July, with concurrent heatwaves across the northern hemisphere, notably in the US and eastern China. In response to huge media interest in these simultaneous events, World Weather Attribution carried out another rapid study, looking at changes in the hottest temperatures each year in each region (WWA, 2023 Northern Hemisphere Heatwave). In Europe, the report examined changes in the warmest week of the year over an area of southern Europe from 5W-25E and 36-45N (domain 4 in Figure 8.1). In ERA5 reanalysis, the week from July 12-18 2023 was found to be an unusual but not extreme event, with a return period of 9 years in the current climate. However, similar temperatures were found to have been virtually impossible in a 1.2°C cooler pre-industrial climate, while the hottest week of each year in that region was found to have been made 2.9°C warmer by climate change. Models again simulated smaller increases in local temperatures in response to global warming than in the reanalysis, but this time the discrepancy was smaller, with an average increase of 2.3°C in the mean temperature of the hottest week, and a probability ratio of over 2500. Overall, the study concluded that week-long heatwaves in the region were 2.5°C hotter than they would have been without human-caused climate change, and that similar week-long temperatures would have been virtually impossible without anthropogenic warming.

While these studies relate directly to heat events with large reported mortality impacts, many others have drawn similar conclusions about changing heat extremes in Europe. Christidis et al. (2015) found that European heatwaves that would have been expected to occur twice a century in the early 2000s were expected to occur twice a decade in 2015; Ma et al. (2020) used CMIP6 models to estimate a 23-fold increase in extreme heat events over Western-Central Europe since the 1980s; and Vautard et al. (2020) found that the July 2019 heatwave had a return period of 50-150 years at the time of writing, and would have had a return period of more than 1000 years without human influence, with local temperatures

increasing by two to three times the global warming level. They also note that the observed trends are much larger than those simulated by climate models; more recent research indicates that around 0.8°C of observed warming is likely due to changes in atmospheric circulation that are underestimated by the climate models (Vautard et al., 2023), implying that the synthesised numbers reported above are almost certainly conservative estimates of the true level of warming.

8.3 Vulnerability and exposure

The large number of excess deaths observed in 2015, 2022, and 2023 is a result of the combination of quickly rising temperatures across Europe, and an increasingly vulnerable population, especially as the continent ages, urbanises, and the existing building stock and infrastructure is not built for the hotter climate (EEA, 2023; Åstrom et al., 2017).

Those most susceptible to heat risks are ageing populations, people with pre-existing health conditions (such as heart, lung and kidney conditions), heavy labourers, young children and people living with mental health conditions. A 2022 study by Ballester et al in 2022 found that Southern Europe faces the highest rates of heat mortality in Europe (Italy, Greece and Portugal) (Ballester et al, 2023). The same study also found that women were 56% more susceptible to death than men, both physiological and sociocultural factors were cited as possible causes.

There has been notable progress in advancing heat early warning systems and action plans, especially following the historic 2003 heatwave in Europe. One study for example estimates that heat-related mortality is 80% lower than it would have been without adaptation measures. (Gallo et al., 2024). Another, 2017 study concluded that significant adaptation would need to be undertaken in Europe in order to maintain heat-related mortality at present levels in a changing climate, let alone reduce mortality (Åstrom et al., 2017).

However, death rates still remain high and notable gaps in existing Heat Action Plans include long-term urban planning, real-time surveillance measures, and indoor heat reduction strategies, as well as plan implementation (Sanchez Martinez et al., 2022, Kotharkar and Ghosh, 2021). Furthermore, Heat-Health Early Warning Systems need to be linked to active identification and care of high-risk people, with clear delineation of responsibilities across agencies like the weather service, local health and social care agencies to increase effectiveness, rather than passively disseminating heat avoidance advice (Kovats and Ebi, 2006).

9. Mediterranean Storm Daniel - 2023

Key messages from Storm Daniel:

- *Most of the fatalities in Libya occurred when two dams collapsed in the middle of the night. While the dams were not designed to deal with the record rainfall levels the region experienced, a lack of maintenance due to ongoing conflict in the region had led to deterioration of dam infrastructure, and lack of awareness of warnings meant that huge numbers of people were exposed to the floods once the dams gave way. Dam infrastructure is ageing around the world, and risk of failure is an emerging global risk.*
- *Observation-based assessments show a strong increase in rainfall, in line with what we would expect from physical understanding; however, these trends are only seen in some climate models while others show a drying. Including all models risks underestimating the role of climate change.*

9.1 Introduction

During the first two weeks of September 2023, torrential rain fell in several countries across the Mediterranean, caused by low-pressure systems forming around a blocking high centred over the Netherlands. The impacts began on the 3rd of September in Spain, when very heavy rainfall over a few hours led to floods in the central and southern parts of the country, killing at least six people (France24, 2023). This episode was followed by Storm Daniel, the worst storm to hit Greece since records began in 1930 (Reuters, 2023), which brought very heavy rain that led to floods in central Greece and Bulgaria between the 4th and the 7th of September. At least seventeen deaths were reported in Greece (Greek Herald, 2023), seven in Türkiye (Iran Front Page, 2023), and four in Bulgaria (Floodlist, 2023). The storm then moved south and developed into a 'medicane' (a Mediterranean hurricane) that made landfall on the Libyan coast in the early hours of the 10th with strong winds of 70-80 km/h (WMO, 2023). In the city of Derna, 250mm of rain fell within a few hours, with 414.1 mm in Bayda and 240 mm in Marawah, according to the National Center of Meteorology in Libya (FloodList, 2023). The intense rainfall caused two dam breaks in the city of Derna, which caused four bridges and some multi-storeyed buildings to collapse on the night of the 10th, sweeping away entire neighbourhoods (Aljazeera, 2023; Reuters; 2023). 5,923 fatalities were reported, while over 44,000 were displaced (ReliefWeb, 2024). The devastating scale of impacts associated with the event rendered it the deadliest and costliest storm over the Mediterranean and Africa, respectively, on record (Yale University, 2023).

9.1.1 Meteorological context

The combination of a high-pressure system trapped between two low-pressure systems is known as an Omega block, named for the resemblance of the circulation pattern to the Greek letter Ω. The block disrupted the typical west-to-east progression of weather systems, resulting in stagnant weather conditions across Europe which consequently led to heavy rainfall over the Iberian Peninsula, Greece, Bulgaria and Türkiye, as well as a late summer heatwave over France, the Benelux countries, and the UK. Omega blocks have been associated with several extreme events including those that caused record-breaking floods

downstream in Pakistan in 2010 (e.g. Hong et al., 2011), flash floods in large parts of western and central Europe in May 2018 (Mohr et al., 2020), extreme rainfall in Northwestern Iran in 2008 (Samakosh et al., 2012), the record-shattering 2010 heatwave in Russia (Di Capua e al., 2021), and exceptional heatwaves in 2019 May in France and July in Germany (Bissolli et al., 2019).

9.1.2 Previous studies

In the immediate aftermath of the storms, World Weather Attribution produced a rapid analysis evaluating the contribution of climate change to the intense rainfall (Zachariah et al., 2023), finding that the rainfall in Eastern Europe has been made up to ten times more likely and up to 40% more intense, and the rainfall in Libya up to fifty times more likely and as much as 50% more intense, by anthropogenic warming of 1.2C. These results were supported by independent analyses carried out by the ClimaMeter group, which found that daily rainfall associated with Mediterranean depressions similar to Storm Daniel has been made 4-9mm more intense over Greece (ClimaMeter, 2023a), and 5-9mm more intense over the Libyan coast, due to global warming since 1979-2000 (ClimaMeter, 2023b). No attribution study was carried out on the heavy rainfall in Spain on September 3rd because much of the rain fell in less than half a day, and attribution of sub-daily rainfall remains challenging.

9.2 Hazard attribution

No new hazard analysis has been carried out for this event. Instead, we summarise the findings of the rapid attribution of the deadly rainfall over Libya carried out in the immediate aftermath of the event (WWA, 2023 Libya floods). The study evaluated annual maxima of one-day rainfall averaged over the region outlined in Figure 9.1. The rainfall year is assumed to run from July to June so that the wettest part of the season (which peaks in January) falls in the centre of the year.

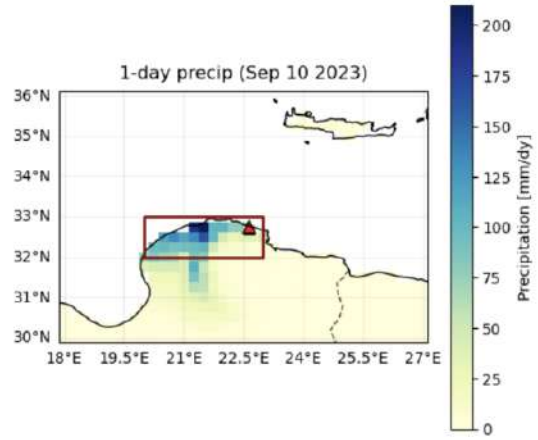

Figure 9.1: *Daily rainfall in northern Libya on 10 September (ERA5). The red triangle indicates the city of Derna, where the most severe impacts were reported.*

In ERA5, the rainfall in Libya on September 10th, 2023 was many times higher than any single day of precipitation previously recorded in that region; the event was estimated to have a return time of 643 years in the current climate, albeit with very high uncertainty (115

to over a million years). Events of comparable magnitude were estimated to be around three times more likely now than in a 1.2°C cooler climate, and around 29% more intense. Attribution was carried out for a hypothetical 1-in-600-year event in this region.

After comparing with station data, only ERA5 was found to replicate both the spatial extent and the magnitude of the rainfall event, so this was the only observational dataset included in the analysis. Fourteen climate models were found to adequately simulate the spatial, seasonal and statistical distribution of rainfall in the region well enough to be included in the hazard synthesis. The overall results of the analysis are summarised in Figure 9.2, with full details available from the WWA report (WWA, 2023 Libya floods).

ERA5 (blue bar) shows a strong increase in both the intensity (panel a) and likelihood (panel b) of similar events, albeit with very large uncertainties. However, the climate models exhibit mixed trends, and as a result the weighted model average (red bar) - and therefore the overall synthesis (purple bar), which places more weight on the models because of the high uncertainty about the observational result - indicates close to zero change. Because of the lack of agreement between the climate models, we reported the unweighted mean of the observations and model results (white bar), thus giving equal weight to the observations and the climate model mean. The resulting wide uncertainty ranges include the weighted average - and thus the possibility that human-induced climate change did not alter the likelihood or intensity of the event - but also highlights that the likelihood of such events could have increased by up to a factor of 50, and the intensity by up to 45%.

We were confident in reporting an expected increase in precipitation in response to global warming even though the uncertainty range included the possibility of no change, due to our understanding of the physical processes underpinning similar rainfall events. From thermodynamic theory we know that an increase in intensity of 7% is to be expected with each 1°C of warming, so around 10% more precipitation would be expected given current warming levels. We could therefore only confidently report “no change” as the main result if there was a well known dynamic process counteracting this effect. While there are some papers exploring this (e.g. Brogli et al., 2019, Zittis et al., 2021), no conclusive results have been found. Furthermore studies focussing on extreme rainfall with future warming also show an increase in heavy rainfall on the 1 to 5-day timescale emerging (Zittis et al., 2022; Seneviratne et al., 2021), rendering it very plausible that the increase in the observation based product is indeed a trend due to climate change. The known fact that climate models with a resolution that requires convection to be parameterized, rather than simulated directly, are unlikely to be able to fully capture these events (Berg et al., 2019) further supported the decision not to give too much weight to the models and suggests the models could indeed not capture the process leading to the observed increase. The assessment of the models at 2°C of global warming thus does not add more information to the trends seen in ERA5, so no projected increase was reported.

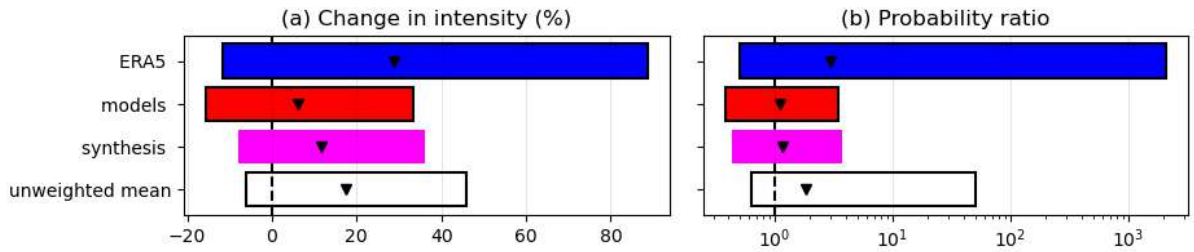

Figure 9.2: *Summary and synthesis of results from observational datasets and climate models for a 10-year event in the northern Libya region. See Section A.1.8 for a detailed description of how to interpret the synthesis plot.*

9.3 Vulnerability and exposure

The extensive and severe impacts in Libya were a result of both the highly unusual amount of rain that fell, and infrastructure and systems that were unable to withstand the hazard, compounded by the ongoing conflict situation, and cascading hazards such as landslides.

Built in the 1970s and located only one kilometre above Derna, the Abu Mansour and Al-Bilad dams were constructed to help protect the city after previous devastating flood events, as well as providing water for agriculture (News Libya, 2023). When the Al-Bilad dam burst at approximately 02:30 am on the morning of 11 September, the accumulated water rushed downstream and overwhelmed Abu Mansour to the point of collapse (Al Jazeera, 2023). Three to seven metre high flash floods subsequently tore through the city (CNN, 2023; EOS, 2023; IFRC, 2023), destroying dense settlements along the river's course. Preliminary reports indicated that both dams may not have been built to withstand the volumes of rainfall that fell over the largely arid Northeastern Libya, and state fragility had moreover severely limited the maintenance of the dam system since 2002 (Ashoor, 2022; University of Reading, 2023; Al Jazeera, 2023a; Al Jazeera, 2023b).

The volume of water and overnight timing of the dam failures meant that anyone in the path of the water was at increased risk, not just those who are typically highly vulnerable. Ongoing conflict and state fragility in Libya compounded the effects of the flooding, contributing to a lack of maintenance and deterioration of dam infrastructure over time and increasing people's risk and the resulting impacts (Irhiam & Watanabe, 2023). The conflict also limited nation-wide adaptation planning and coordination across a range of climate issues facing the country, such as water scarcity and extreme weather including heat and floods (UNFCCC, 2016).

Nonetheless, catastrophic dam failures and the associated impacts can be limited through risk reduction protocols that include real-time monitoring of forecasts, water volumes, and warning systems that alert those downstream of possible failures and the need to evacuate. While there was a forecast with a 3-day lead time on the track of Storm Daniel in Libya, the impact of that potential rainfall on infrastructure and people was not clearly understood in advance. Further, it is not clear to what extent forecasts and warnings were communicated and received by the general public, or relevant emergency responders (Reuters, 2023). In conjunction with improved emergency management capacity, impact-based forecasts may help to provide a clearer understanding of how the rainfall translates into potential impacts and could lead to improved warnings in the future (WMO, 2021).

This disaster also points to the challenge of needing to design and maintain infrastructure for not just the climate of the present or the past, but also the future (Perera et al., 2022). In Libya, this means taking into account the long-term decline in average rainfall, and at the same time, the increase in extreme rainfall like this heavy rainfall event; a challenging prospect especially for a country plagued by crises.

Appendix

A.1 Data and methods

Throughout the new studies shown in this report, multiple lines of evidence are synthesised including both observational and reanalysis datasets and climate models with different framings. They are described as follows and summarised in section A.1.3.

A.1.1 Observations and reanalysis

1. ERA5: The European Centre for Medium-Range Weather Forecasts's 5th generation reanalysis product is a gridded dataset that combines historical observations into global estimates using advanced modelling and data assimilation systems (Hersbach et al., 2020). We use daily precipitation data from this product at a resolution of 0.25°, from the years 1950 to present.
2. MSWEP: The Multi-Source Weighted-Ensemble Precipitation v2.8 dataset (updated from Beck et al., 2019) is fully global, available at 3-hourly intervals and at 0.1° spatial resolution, available from 1979 to ~3 hours from real-time. This product combines gauge-, satellite-, and reanalysis-based data.
3. CHIRPS: The rainfall product developed by the UC Santa Barbara Climate Hazards Group called "Climate Hazards Group InfraRed Precipitation with Station data" (CHIRPS; Funk et al. 2015). Daily data are available at 0.05° resolution, from 1981-31 August 2024. The product incorporates satellite imagery with in-situ station data.
4. GPCC: Full Data Daily Product Version 2022 of daily global land-surface precipitation totals based on precipitation data provided by national meteorological and hydrological services, regional and global data collections as well as WMO GTS-data (Ziese et al., 2022). It is provided at a regular latitude/longitude grid with a spatial resolution of 1.0 x 1.0 degree and covers the time period from January 1982 to April 2024. Relative precipitation anomalies at the stations (daily totals divided by monthly total) are interpolated by means of a modified SPHEREMAP scheme (Becker et al., 2013; Schamm et al., 2014; Schneider et al., 2018) and then superimposed on the GPCC Full Data Monthly Version 2022 (Schneider et al., 2022) monthly precipitation totals with climatological infilling.
5. IMD: This dataset is developed and maintained by Indian Meteorological Department (IMD), at daily timesteps, and available for the period 1901-2023 (can be downloaded here). The gridded rainfall dataset is developed using the inverse distance weighting method based on records from a variable network of rain gauge stations across India (6955 rain gauge stations with varying availability periods- Pai et al., 2013).

Finally, as a measure of anthropogenic climate change in all studies we use the (low-pass filtered) global mean surface temperature (GMST), where GMST is taken from the National Aeronautics and Space Administration (NASA) Goddard Institute for Space Science (GISS) surface temperature analysis (GISTEMP, Hansen et al., 2010 and Lenssen et al. 2019).

A.1.2 Climate models

Across the studies, we use 3 multi-model ensembles from climate modelling experiments with different framings:

1. Coordinated Regional Climate Downscaling Experiment-East Asia (CORDEX-EAS) (0.22° resolution, EAS-22) multi-model ensemble (Kim et al., 2020), consisting of 6 simulations resulting from pairings of 3 Global Climate Models (GCMs) and 2 Regional Climate Models (RCMs). These simulations are composed of historical simulations up to 2005, and extended to the year 2100 using the RCP 8.5 scenario.

2. CORDEX-WAS-22 model ensemble: Coordinated Regional Climate Downscaling Experiment CORDEX-CORE over the West-Asia domain with 0.22 km resolution (WAS-22) (Teichman et al., 2021). The ensemble consists of 3 regional climate models downscaling 6 GCMs. These simulations are composed of historical simulations up to 2005, and extended to the year 2100 using the RCP8.5 scenario.

3. HighResMIP: SST-forced model ensemble (Haarsma et al. 2016), the simulations for which span from 1950 to 2050. The SST and sea ice forcings for the period 1950-2014 are obtained from the 0.25° x 0.25° Hadley Centre Global Sea Ice and Sea Surface Temperature dataset that have undergone area-weighted regridding to match the climate model resolution (see Table B). For the 'future' time period (2015-2050), SST/sea-ice data are derived from RCP8.5 (CMIP5) data, and combined with greenhouse gas forcings from SSP5-8.5 (CMIP6) simulations (see Section 3.3 of Haarsma et al. 2016 for further details).

A.1.3 Data summary

Event (year of occurrence)	**Observations and reanalyses**	**Climate models**
Cyclone Sidr (2007)	ERA5, MSWEP, GPCC	CORDEX-EAS, CORDEX-WAS
Cyclone Nargis (2008)	ERA5, MSWEP, CHIRPS, GPCC	CORDEX-EAS, CORDEX-WAS
Russian Heatwave (2010)	ERA5	N/A
Indian Flood (2013)	ERA5, MSWEP, CPC, IMD	CORDEX-WAS, HighResMIP

Table A.1.1: Summary of all datasets, described in the previous two subsections, used in each new analysis.

A.1.4 Statistical methods

Methods for observational and model analysis and for model evaluation and synthesis are used according to the World Weather Attribution Protocol, described in Philip et al., (2020), with supporting details found in van Oldenborgh et al., (2021), Ciavarella et al., (2021) and here. The key

steps are trend estimation from observations, model evaluation, multi-method multi-model attribution and synthesis of the attribution statement.

For each study, we analyse time series of the extreme index described above over each study region for a range of observational, reanalysis and model datasets. In each case, a nonstationary distribution, either generalised extreme value (GEV) or gaussian, is used to statistically model these variables. For precipitation, the distribution is assumed to scale exponentially with the covariate, with the dispersion (the ratio between the standard deviation and the mean) remaining constant. For temperature-based indices, the distribution is assumed to shift with the covariate, with the shape parameter remaining constant.

Event (year of occurrence)	**Parameter(s) (Extreme indices)**	**Statistical distribution**	**Assumed change with GMST**
Cyclone Sidr (2007)	Precipitation (Rx1day, OND)	GEV	Scale
Cyclone Nargis (2008)	Precipitation (Rx5day, MAM)	GEV	Scale
Russian Heatwave (2010)	Temperature (July average)	Normal	Shift
Indian Flood (2013)	Precipitation (Rx4day, JJA)	GEV	Scale

Table A.1.2: Summary of statistical distributions and assumptions about nonstationarity with GMST for the new studies in this report.

For each time series we calculate the return periods and intensity of the event under study for the GMST at the year of event occurrence versus a cooler pre-industrial climate. For all of the studies, this is given by a 0.9 C cooler climate: this allows us to compare the climate of now and of the preindustrial past (1850-1900, based on the Global Warming Index), by calculating the probability ratio (PR; the factor-change in the event's probability) and change in intensity of the event.. We also repeat the calculations for a 2024 GMST and a 1.3 C cooler pre-industrial climate, allowing us to also compare the likelihood of a similar hazard at present and how this has changed even since it initially occurred.

A.1.5 Climate Model Evaluation

The climate models are evaluated against the observations in their ability to capture:

1. Seasonal cycles: For this, we qualitatively compare the seasonal cycles based on model outputs against observations-based cycles. We discard the models that exhibit ill-defined peaks in their seasonal cycles. For example, we discard the model if the rainy season onset/termination varies significantly from the observations.

2. Spatial patterns: Models that do not match the observations in terms of the large-scale patterns are excluded.

3. Parameters of the fitted statistical models: We discard the model if the model and observation parameters ranges do not overlap.

The models are labelled as ‘good’, ’reasonable’, or ’bad’ based on their performances in terms of the three criteria discussed above. A model is given an overall rating of ‘good’ if it is rated ‘good’ for all three characteristics. If there is at least one ‘reasonable’, then its overall rating will be ‘reasonable’ and ‘bad’ if there is at least one ‘bad’. For each framing or model setup we use climate models that only just pass the evaluation tests if we only have five models or less for that framing that perform well.

A.1.6 IRIS storm track model

Assessing tropical cyclone risk given the infrequency of landfalling tropical cyclones (TC) and the short period of reliable observations remains a challenge. Synthetic tropical cyclone datasets can help overcome these problems. We explore this method here using a new global tropical cyclone wind model (IRIS) with several key innovations. It recognises that the key step for estimating landfall wind speed is the location and value of the life-time maximum intensity (LMI). It redefines the problem as one of decay only. The initial intensity, life-time maximum, is assumed to be physically constrained by the thermodynamic state as defined by the potential intensity (PI).

Observations show that the relative intensity, defined as observed maximum intensity divided by the potential intensity, follows a robust uniform distribution. This drives the stochastic model lifetime maximum intensity. The landfall intensity is then a fraction of this lifetime maximum depending on the time to landfall. Tracks are based on IBTRACS observations. The original model description paper has been accepted for publication (Sparks and Toumi, 2024). IRIS calculates basin and landfall wind speed intensity distributions from the location of LMI and the corresponding potential intensity at that location, based on observed tracks between 1980 and 2024.

There has been a recent observed global warming of about 1.0°C, putting the global mean temperature close to about 1.3°C above pre-industrial temperature in 2024, and about 0.9 °C in 2007/08. Regional and local prediction of absolute PI by climate models is problematic as they are known to have biases. Regional observed changes are difficult to distinguish from natural variability. We therefore make the assumption that the anthropogenic trend is the global zonal mean PI trend, and use the observed PI trend since 1979 from ERA-5. There is some warming from pre-industrial to 1979 for which we have incomplete potential intensity data. To estimate the pre-industrial potential intensity state we extrapolate backwards the current observed trends. This approach avoids the selection of any climate model. The method is simple and robust.

A.1.7 Climate Shift Index: Ocean

Climate Central’s Climate Shift Index: Ocean (Ocean CSI) tool is used to rapidly compute the influence of human-caused climate change on Sea Surface Temperatures along each Tropical Cyclone track. The methodology underpinning this attribution tool is based on peer-reviewed research (Giguere et. al, 2024). It uses a combination of an empirically-driven attribution method using OISST

data (Huang et. al, 2021), and model simulations using an ensemble of 13 debiased CMIP6 models. Results from these two methods are aggregated to compute a single metric measuring the increase in likelihood of an SST occurring as a result of climate change. This metric, called the Ocean CSI, is the ratio of the probability of a temperature occurring in today's climate to the probability of that same temperature occurring in a world without human-caused climate change. In addition to likelihood changes, the methods used to compute the Ocean CSI can be used to measure the temperature increase in Celsius (called the "climate-driven warming) in a location on a given day due to climate change (Giguere et. al, 2024). This allows us to calculate the specific difference between an observed daily temperature in a location and what that temperature would have been in a counterfactual world without climate change. We estimate both the Ocean CSI and climate-driven warming along each Tropical Cyclone track and in the surrounding region. The Ocean CSI uses 0.25° by 0.25° latitude-longitude grid cells. For each point along the track, we found the cell and corresponding daily metrics closest to the centre of the storm at that time.

A.1.8 Interpreting synthesis plots

Synthesis plots present the estimated changes in intensity or likelihood of the event of interest from both observational datasets (shown as blue bars) and climate models (red bars), along with weighted and unweighted averages of this information that is used to give an overarching attribution statement. The best estimate for each dataset is marked with a black triangle, while the coloured bars represent a 95% confidence interval obtained by bootstrapping. When more than one observational data product is used, a term to account for the spread of the best estimates is added in quadrature to the natural variability of each dataset: this is shown in the figures as a white box around the light blue bars. The dark blue bar indicates the average of the observational data products, including this additional uncertainty. Similarly, a term to account for intermodel spread is added in quadrature to the natural variability of the models: this is shown in the figures as white boxes around the light red bars. The dark red bar shows the weighted model average, where the weights are derived from the precision (inverse of the variance) of each model estimate.

Observation-based products and models are combined into a single result in two ways - a detailed description including the mathematical formulations can be found in the literature (Philip et al., 2020; Li & Otto, 2022). Firstly, we neglect common model uncertainties beyond the intermodel spread already incorporated in the observational and model averages, and compute the precision-weighted average of models (dark red bar) and observations (dark blue bar): this weighted mean is indicated by the magenta bar. To account for the fact that, due to common model biases, model uncertainty can be larger than the intermodel spread, we also show an unweighted average of the synthesised observations (dark blue bar) and models (dark red bar), indicated by the white box in the bottom row of the synthesis figures.

A.1.9 Summary of results

Event (year)	**Region(s) affected**	**Mortality**	**Attribution to climate change at the year of occurrence**		
Cyclone Sidr	Bangladesh	>4234	**Precipitation**	**Wind speeds**	**SSTs**

(2007)			**(RX1day, OND)** PR: 0.5 - 4 ΔI: -22 - 33%	PR: ~1.16 ΔI: 2.4 m/s	PR: 1.3 ΔI: ~0.69 °C
Cyclone Nargis (2008)	Southern Myanmar	>138366	**Precipitation (Rx5day, MAM)** PR: 0.25 - 55 ΔI: -19 - 49%	**Wind speeds** PR: ~1.18 ΔI: 5.2 m/s	**SSTs** PR: 1.47 ΔI: ~0.66 °C
Russian Heatwave (2010)	Western Russia	55736	**Temperature** PR: 3 - 7000 ΔI: 0.3 - 4.3 °C		
Horn of Africa Drought (2011)	Somalia, Ethiopia, Kenya	258,000	**Precipitation (MAM,seasonal total)** PR: >1 ΔI: >0		
India Floods (2013)	Uttarakhand, India	6054	**Precipitation (JJA Rx4day)** PR: 1.97 (1.26 - 4.17) ΔI: 11.4% (5.86% -16.9%)		
Typhoon Haiyan (2013)	Philippines	7354	**Precipitation** PR: >1 ΔI: >0	**Wind speeds** PR: >1 ΔI: >0	**Storm surge** PR: >1 ΔI: >0
Europe Heatwave (2015)	France	3275	**Temperature** PR: > 2		
Europe Heatwave (2022)	Italy, Spain, Germany, France, Greece, Romania, Portugal, UK	53542	**Temperature (tx1x / tn2x)** PR: > 17 / > 9 ΔI (observations): 3.6 °C / 4.0 °C ΔI (models): 1.9 °C / 1.9 °C		
Europe Heatwave (2023)	Italy, Spain, Germany, Greece, France, Romania	37129	**Temperature (western Mediterranean / southern Europe)** PR: ineffable / > 1000 ΔI: 2 (1.7 - 3.5) / 2.5 (2.0 to 3.2) °C		
Storm Daniel (2023)	Libya	12352	**Precipitation (Rx1day)** PR: 1 - 50 ΔI: 0% - 46%		

Table A.1.3: Summary of attribution results, including new analyses in this study and historical analyses, for the ten deadliest extreme weather events recorded in EMDAT since 2004. Light red is used to indicate a likely increase due to the influence of climate change that cannot confidently be quantified, dark red indicates a quantitative attribution to climate change. The attribution numbers given in this table should be used with caution: each number pertains to a specific event definition, which is impossible to describe completely in a summary table. Complete descriptions can be found in the relevant section of the full report above.

A.2 Cyclone Sidr

A.2.1 Model evaluation

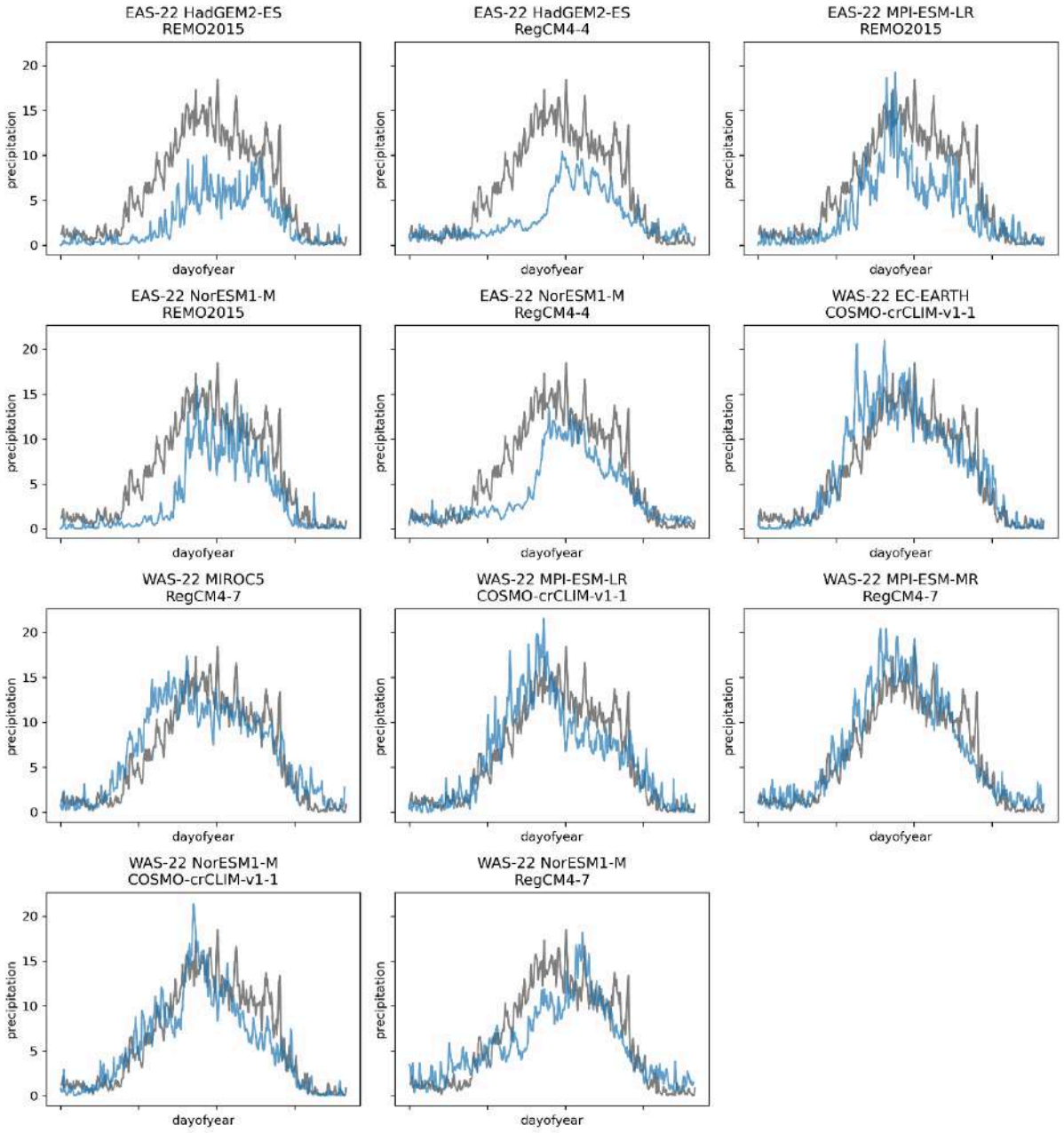

Figure A.2.1: Seasonal cycles of precipitation over the study region for Cyclone Sidr in CORDEX models (blue) and observations represented by MSWEP (black) for a climatology period 1991-2020.

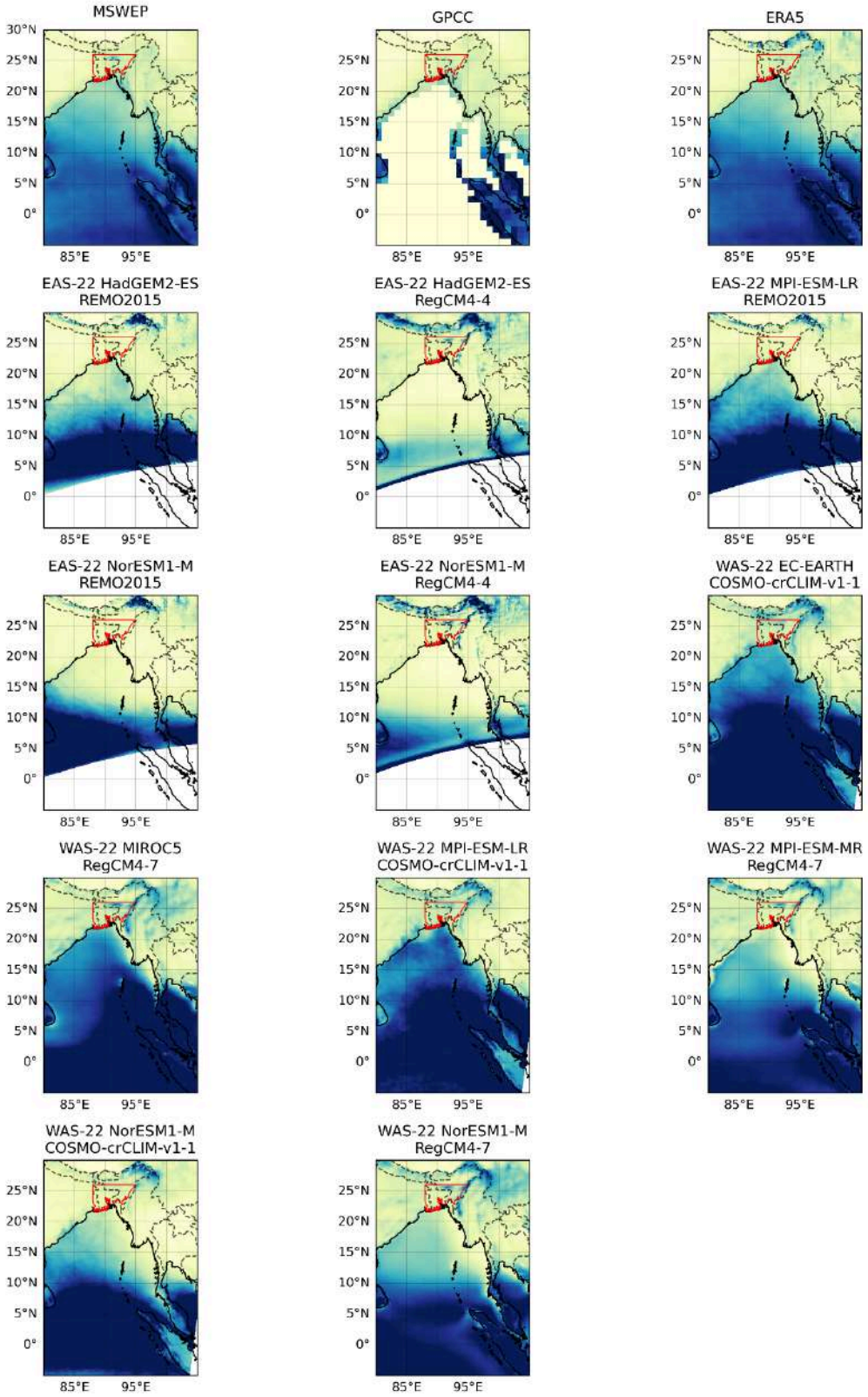

Figure A.2.2: Spatial patterns of precipitation for October-December over the Bay of Bengal in CORDEX models and observations (top row) for a climatology period 1991-2020. The study region for Cyclone Sidr is shown in red.

Model / Observations	Seasonal cycle	Spatial pattern	Dispersion	Shape parameter	Conclusion
MSWEP			0.526 (0.408 ... 0.616)	-0.076 (-0.427 ... 0.172)	
ERA5			0.533 (0.448 ... 0.602)	-0.014 (-0.395 ... 0.282)	
GPCC			0.585 (0.45 ... 0.689)	-0.285 (-0.592 ... 0.049)	
CORDEX WAS					
WAS-22_EC-EARTH_rcp85_r12i1p1_COSMO-crCLIM-v1-1 (1)	good	reasonable	0.476 (0.351 ... 0.575)	-0.16 (-0.35 ... 0.033)	reasonable
WAS-22_MIROC5_rcp85_r1i1p1_RegCM4-7 (1)	good	good	0.512 (0.376 ... 0.600)	-0.076 (-0.45 ... 0.21)	good
WAS-22_MPI-ESM-LR_rcp85_r1i1p1_COSMO-crCLIM-v1-1 (1)	good	good	0.450 (0.343 ... 0.526)	-0.25 (-0.72 ... 0.10)	good
WAS-22_MPI-ESM-MR_rcp85_r1i1p1_RegCM4-7 (1)	good	good	0.565 (0.419 ... 0.653)	0.16 (-0.17 ... 0.43)	good
WAS-22_NorESM1-M_rcp85_r1i1p1_COSMO-crCLIM-v1-1 (1)	good	reasonable	0.629 (0.490 ... 0.720)	0.19 (-0.27 ... 0.48)	reasonable
WAS-22_NorESM1-M_rcp85_r1i1p1_RegCM4-7 (1)	good	reasonable	0.486 (0.392 ... 0.555)	0.15 (-0.18 ... 0.49)	reasonable
CORDEX EAS					
EAS-22_HadGEM2-ES_rcp85_r1i1p1_RegCM4-4 (1)	bad	bad	0.511 (0.371 ... 0.595)	0.33 (0.088 ... 0.69)	bad
EAS-22_HadGEM2-ES_rcp85_r1i1p1_REMO2015 (1)	reasonable	reasonable	0.706 (0.559 ... 0.797)	0.36 (0.034 ... 0.69)	reasonable
EAS-22_MPI-ESM-LR_rcp85_r1i1p1_REMO2015 (1)	reasonable	reasonable	0.621 (0.488 ... 0.692)	0.075 (-0.29 ... 0.68)	reasonable
EAS-22_NorESM1-M_rcp85_r1i1p1_RegCM4-4 (1)	reasonable	reasonable	0.441 (0.323 ... 0.522)	0.25 (-0.064 ... 0.60)	reasonable
EAS-22_NorESM1-M_rcp85_r1i1p1_REMO2015 (1)	reasonable	reasonable	0.616 (0.419 ... 0.734)	0.33 (0.099 ... 0.71)	reasonable

Table A.2.1: Evaluation of the climate models considered for attribution of rainfall from Cyclone Sidr. For each model, the best estimate of the dispersion and shape parameters are shown and a 95% confidence interval for each, obtained via bootstrapping. The qualitative evaluation is shown in the right-hand column.

A.2.2 Synthesis figures

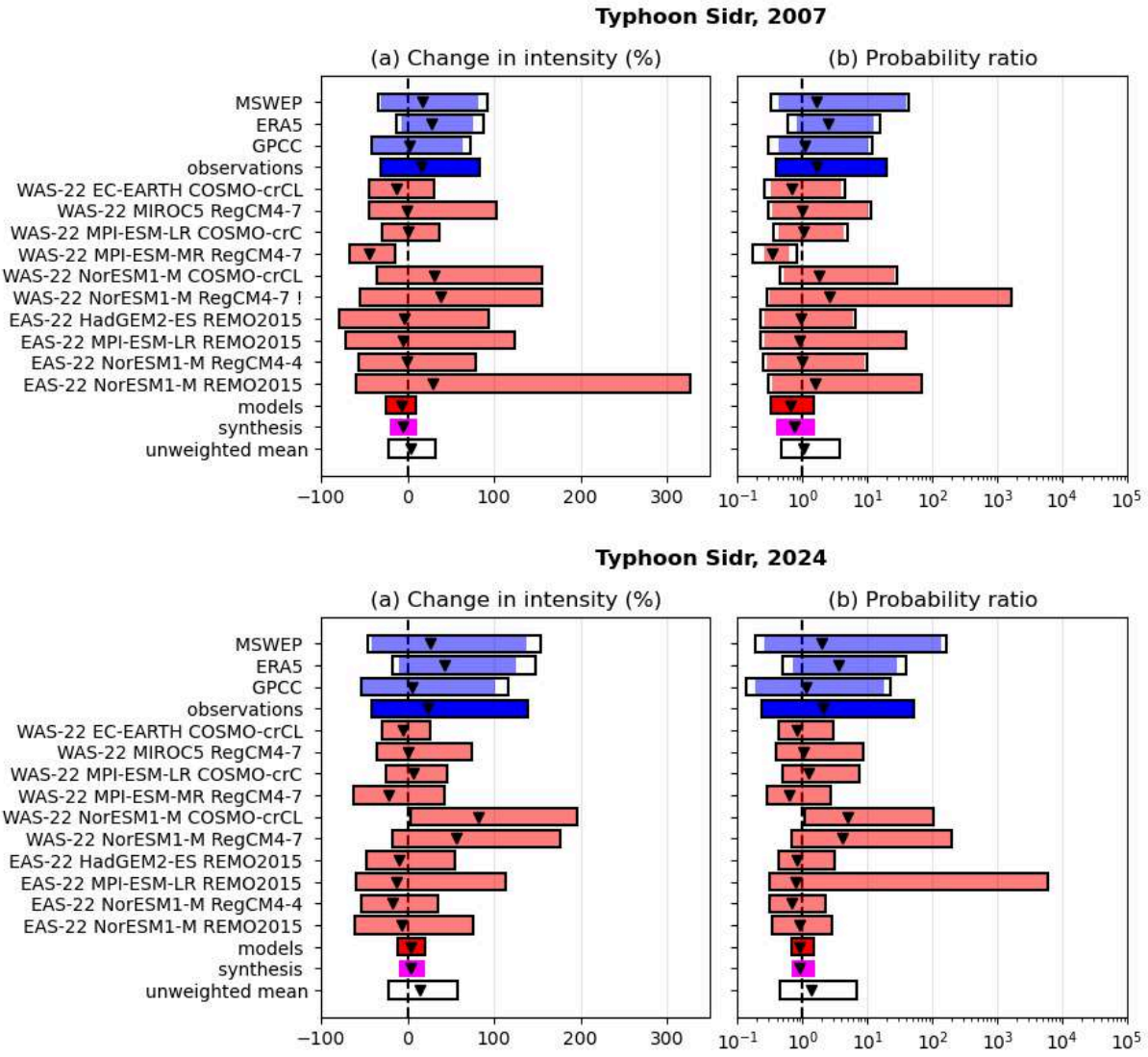

Figure A.2.3: Synthesised changes for a 4-year 1-day OND maximum rainfall event over the part of the Ganges-Brahmaputra basin affected by rainfall from Cyclone Sidr due to GMST. Changes in PR (left) and intensity (right) are shown for two historical periods: comparing the climate at the time of occurrence with a past 0.9°C cooler climate (top row) and comparing the present 2024 climate with a 1.3°C warmed climate (bottom row).

A.3 Cyclone Nargis

A.3.1 Model evaluation

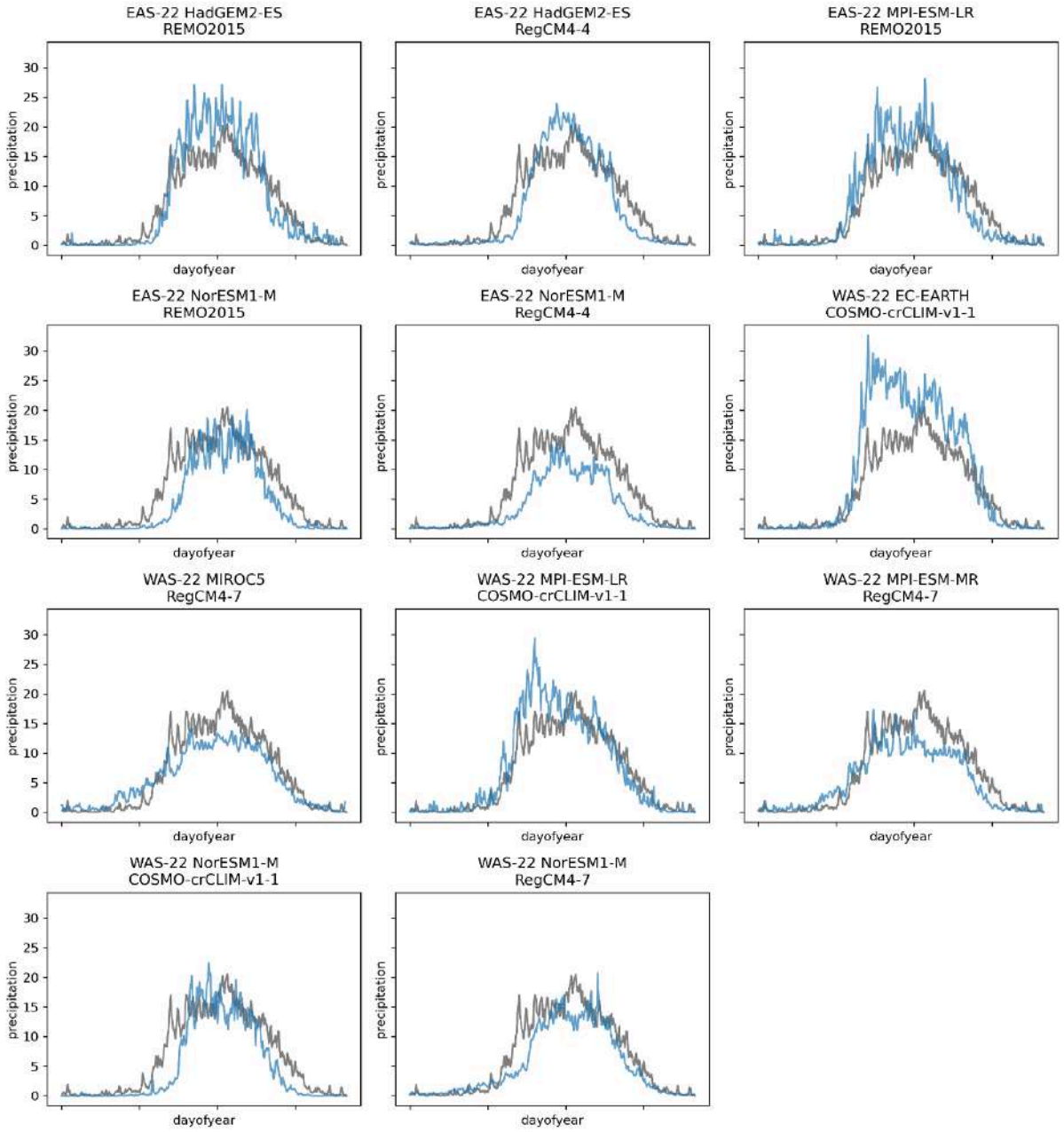

Figure A.3.1: Seasonal cycles of precipitation over the study region for Cyclone Nargis in CORDEX models (blue) and observations represented by MSWEP (black) for a climatology period 1991-2020.

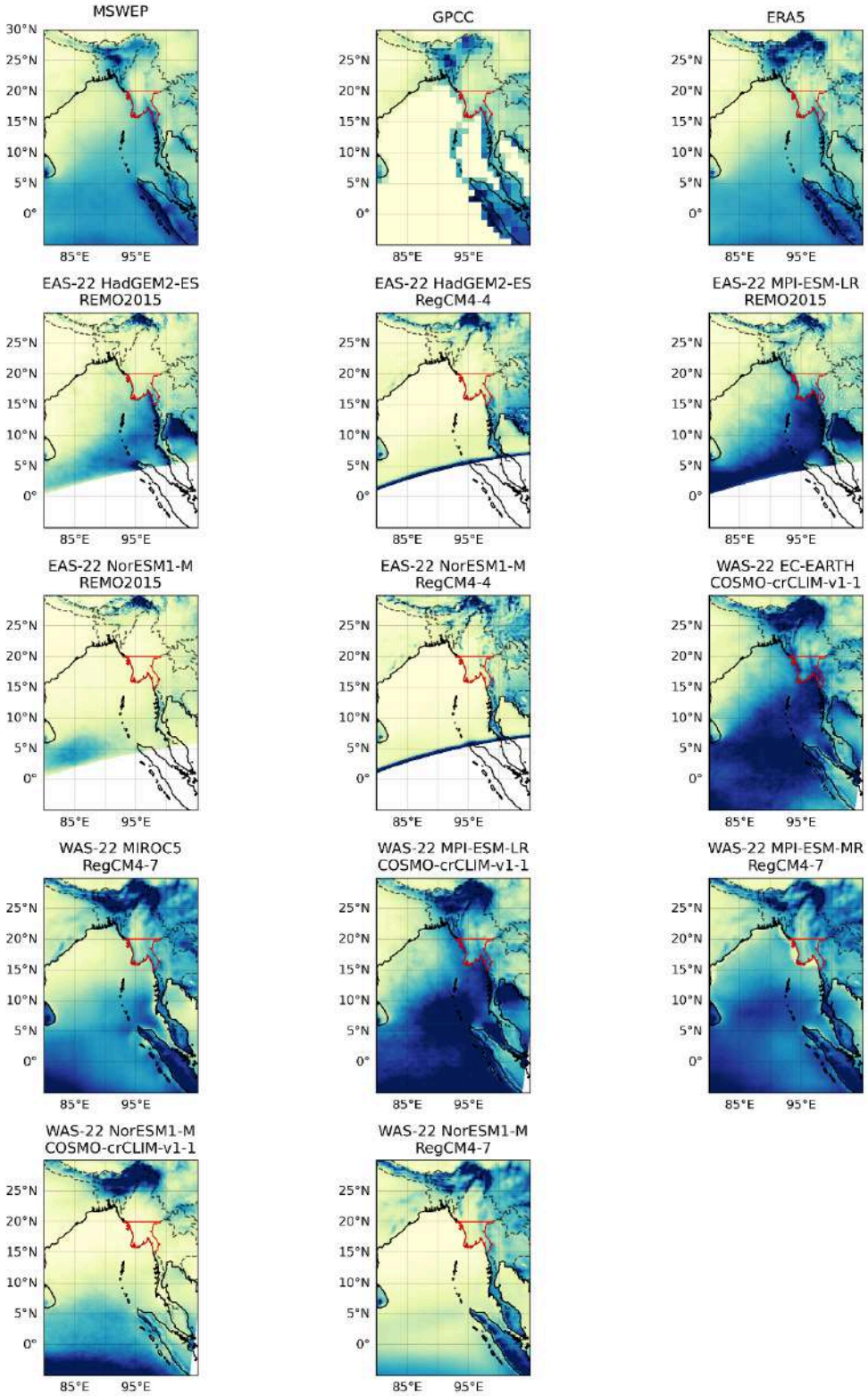

Figure A.3.2: Spatial patterns of precipitation for March-May over the Bay of Bengal in CORDEX models and observations (top row) for a climatology period 1991-2020. The study region for Cyclone Nargis is shown in red.

Model / Observations	Seasonal cycle	Spatial pattern	Dispersion	Shape parameter	Conclusion
MSWEP			0.341 (0.250 ... 0.394)	0.053 (-0.37 ... 0.45)	
CHIRPS			0.358 (0.271 ... 0.422)	-0.028 (-0.25 ... 0.20)	
ERA5			0.369 (0.302 ... 0.420)	0.065 (-0.12 ... 0.42)	
GPCC			0.322 (0.201 ... 0.397)	-0.20 (-0.71 ... 0.019)	
CORDEX WAS					
WAS-22_EC-EARTH_rcp85_r12i1p1_COSMO-crCLIM-v1-1 (1)	reasonable	reasonable	0.400 (0.279 ... 0.488)	-0.15 (-0.43 ... 0.025)	reasonable
WAS-22_MIROC5_rcp85_r1i1p1_RegCM4-7 (1)	good	reasonable	0.322 (0.188 ... 0.405)	0.34 (0.085 ... 0.93)	reasonable
WAS-22_MPI-ESM-LR_rcp85_r1i1p1_COSMO-crCLIM-v1-1 (1)	good	reasonable	0.415 (0.291 ... 0.497)	0.12 (-0.19 ... 0.53)	reasonable
WAS-22_MPI-ESM-MR_rcp85_r1i1p1_RegCM4-7 (1)	reasonable	reasonable	0.445 (0.325 ... 0.534)	0.41 (0.16 ... 0.82)	reasonable
WAS-22_NorESM1-M_rcp85_r1i1p1_COSMO-crCLIM-v1-1 (1)	reasonable	reasonable	0.769 (0.573 ... 0.896)	0.48 (0.20 ... 0.84)	bad
WAS-22_NorESM1-M_rcp85_r1i1p1_RegCM4-7 (1)	reasonable	reasonable	0.437 (0.334 ... 0.516)	-0.17 (-0.62 ... 0.28)	reasonable
CORDEX EAS					
EAS-22_HadGEM2-ES_rcp85_r1i1p1_RegCM4-4 (1)	reasonable	reasonable	0.500 (0.370 ... 0.570)	0.34 (-0.041 ... 0.96)	reasonable
EAS-22_HadGEM2-ES_rcp85_r1i1p1_REMO2015 (1)	good	reasonable	0.521 (0.410 ... 0.592)	-0.039 (-0.34 ... 0.34)	reasonable
EAS-22_MPI-ESM-LR_rcp85_r1i1p1_REMO2015 (1)	good	reasonable	0.349 (0.257 ... 0.432)	-0.33 (-0.86 ... -0.17)	reasonable
EAS-22_NorESM1-M_rcp85_r1i1p1_RegCM4-4 (1)	reasonable	reasonable	0.550 (0.397 ... 0.639)	0.071 (-0.24 ... 0.49)	reasonable
EAS-22_NorESM1-M_rcp85_r1i1p1_REMO2015 (1)	reasonable	reasonable	0.777 (0.556 ... 0.942)	0.50 (0.17 ... 0.97)	bad

Table A.3.1: Evaluation of the climate models considered for attribution of rainfall from Cyclone Nargis. For each model, the best estimate of the dispersion and shape parameters are shown and a 95% confidence interval for each, obtained via bootstrapping. The qualitative evaluation is shown in the right-hand column.

A.3.2 Synthesis figures

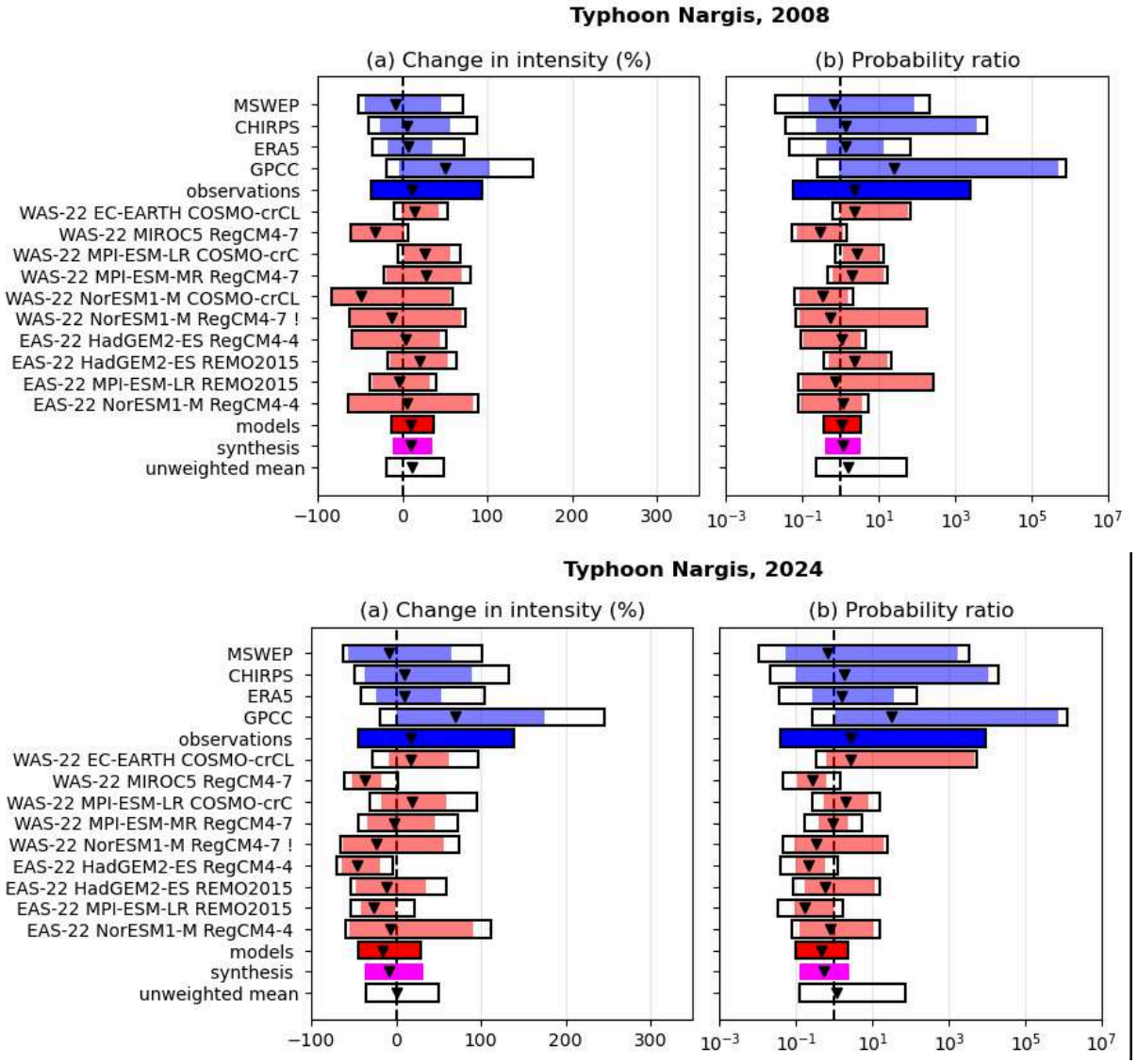

Figure A.3.3: Synthesised changes for a 15-year 5-day MAM maximum rainfall event over the part of southern Myanmar affected by rainfall from Cyclone Nargis, due to GMST. Changes in PR (left) and intensity (right) are shown for two historical periods: comparing the climate at the time of occurrence with a past 0.9°C cooler climate (top row) and comparing the present 2024 climate with a 1.3°C warmed climate (bottom row).

A.4 Russian Heatwave 2010

A4.1 Observational analysis of the Russian heatwave in 2010

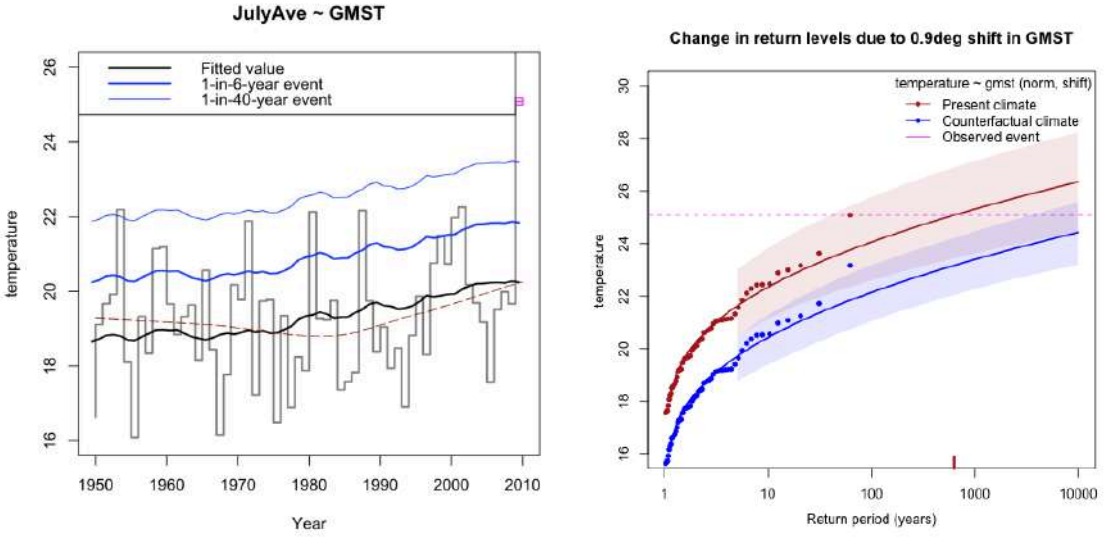

Figure A. 4.1: *Time series (left) and statistical fits (right) to July average temperature over the Western Russian region in ERA5. The influence of GMST is shown with the black line on the trend plots and the red vs blue probability curves. The magnitude of the is highlighted with a purple box (left) and line (right).*

A4.2 Observational analysis of the Russian heatwave in 2024

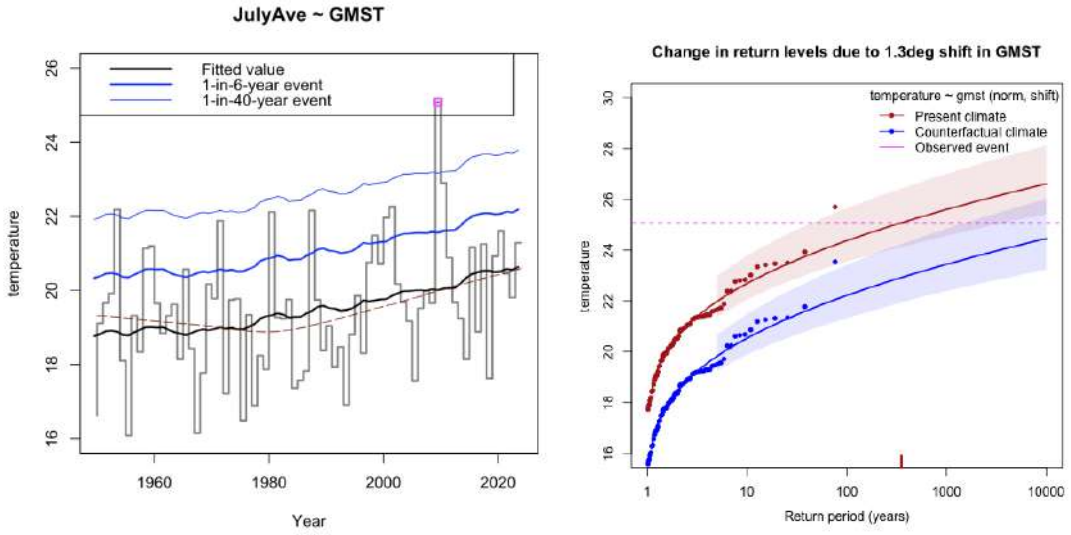

Figure A. 4.2: *Time series (left) and statistical fits (right) to July average temperature over the Western Russian region in ERA5. The influence of GMST is shown with the black line on the trend*

plots and the red vs blue probability curves. The magnitude of the is highlighted with a purple box (left) and line (right).

A.5 Horn of Africa Drought (2011-2024)

A.5.1 Synthesis results

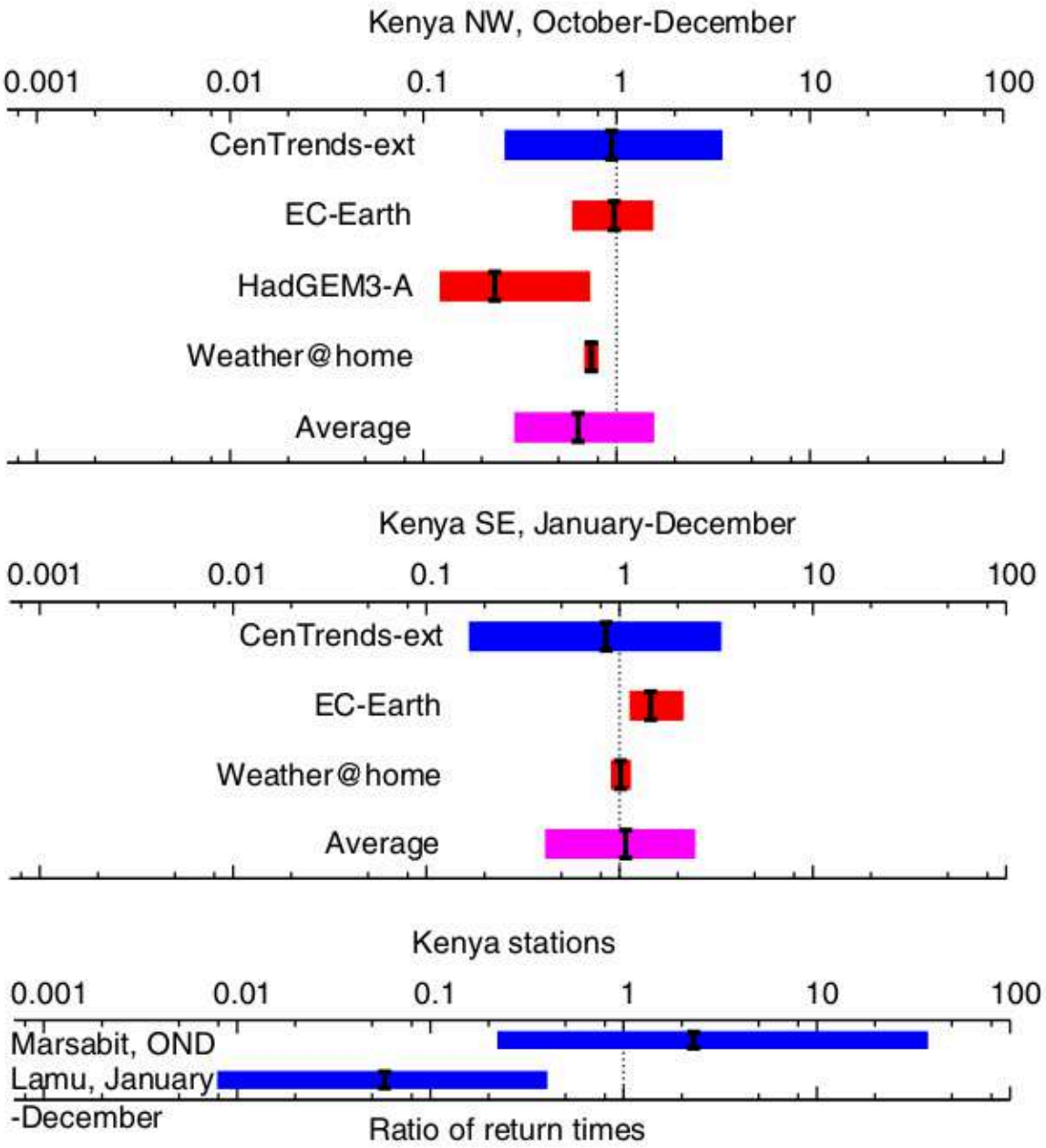

Figure A.5.1 Synthesised changes in return periods of 2016 drought event over Kenya , due to GMST. The upper plots show results for gridded datasets and models for OND season in NE Kenya; middle plots are gridded datasets and models for January–December in SE Kenya; and the lower plots are the station observations. Observations are shown in blue, models in red and the average in purple. Source: Uhe et al., 2018.

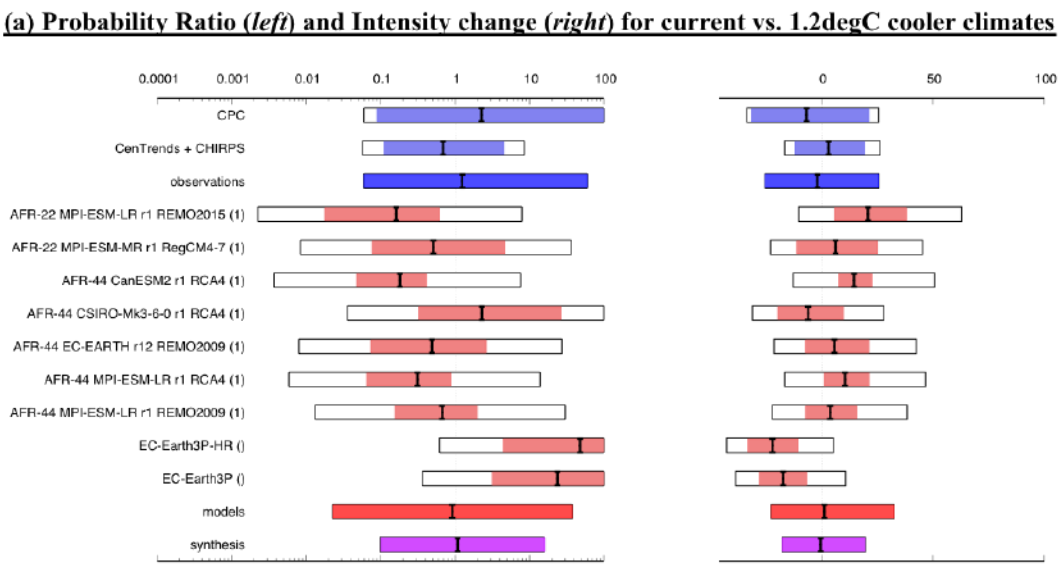

Figure A.5.2 Synthesised changes in return periods (left) and magnitude (right) of 24-month precipitation for 2021-2022 drought event over Horn of Africa, due to GMST. Changes in PR (left) and intensity (right) comparing the event in a 2022 climate to a 1.2 cooler climate. Source: [WWA, 2020-22 Horn of Africa Drought]

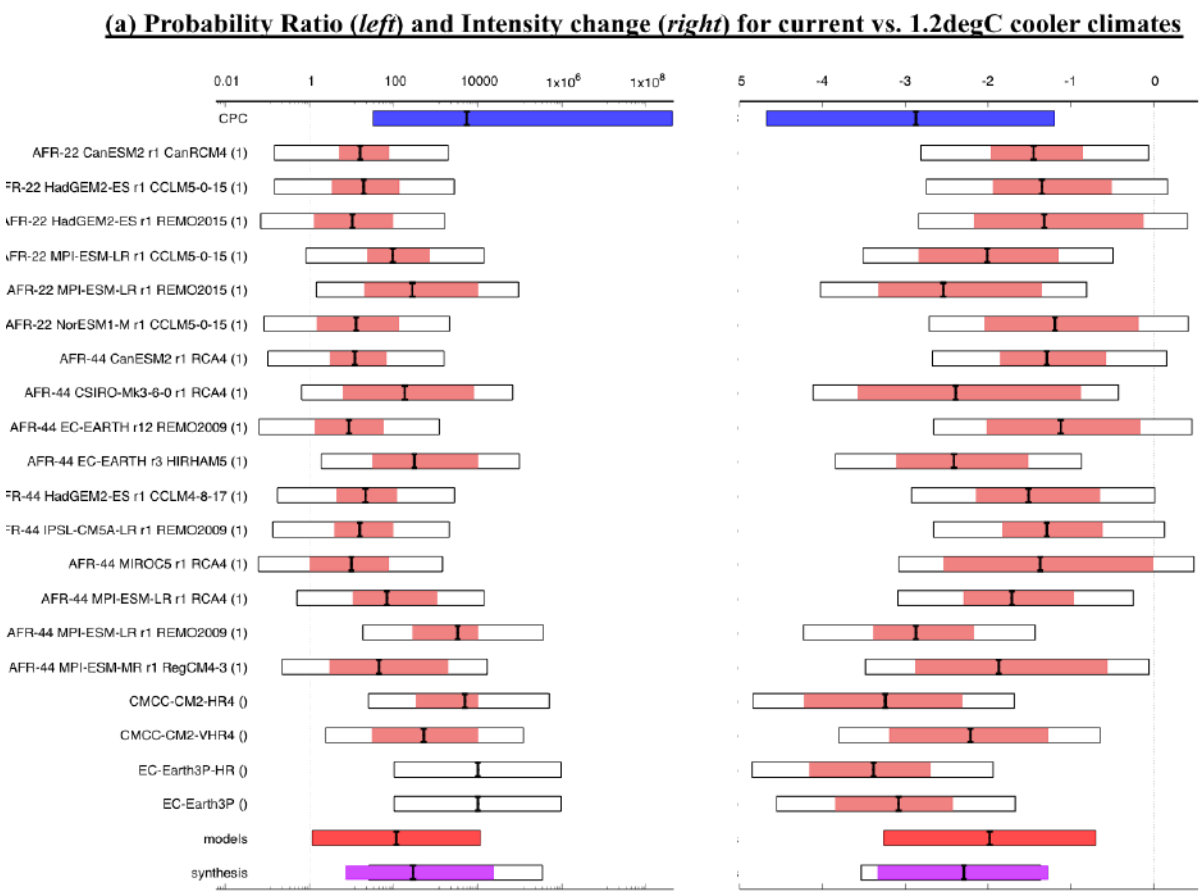

Figure A.5.3 Synthesised changes in probability ratios (left) and magnitude (right) of 24-month SPEI for 2021-2022 drought event over Horn of Africa, due to GMST. Changes in PR (left) and intensity (right) comparing the event in a 2022 climate to a 1.2 cooler. Source: WWA, 2020-22 Horn of Africa Drought

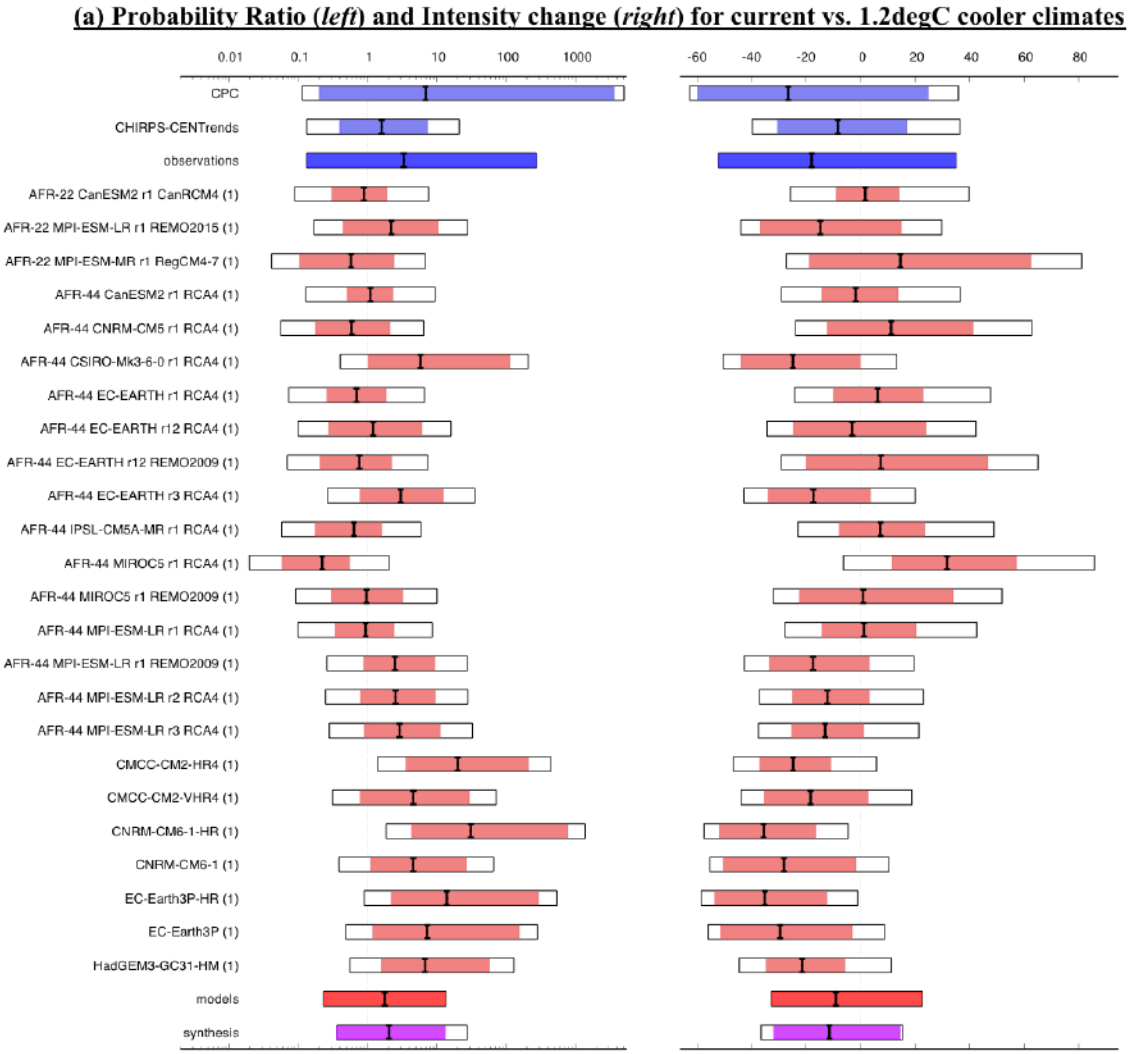

Figure A.5.4 Synthesised changes in probability ratios (left) and magnitude (right) of 2022 MAM rainfall for 2021-2022 drought event over Horn of Africa, due to GMST. Changes in PR (left) and intensity (right) comparing the event in a 2022 climate to a 1.2 cooler. Source: WWA, 2020-22 Horn of Africa Drought

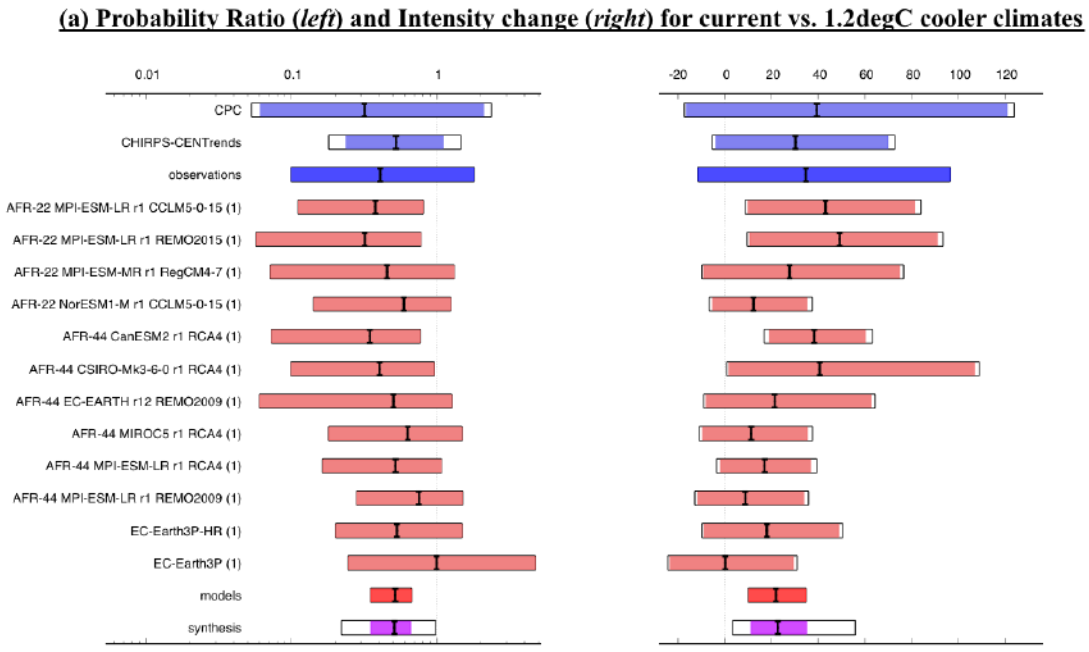

Figure A.5.5 Synthesised changes in probability ratios (left) and magnitude (right) of the 2022 OND rainfall for 2021-2022 drought event over Horn of Africa using NINO3.4 as an additional covariate in the 2022 climate and a 1.2ºC cooler climate. Source: [WWA, 2020-22 Horn of Africa Drought]

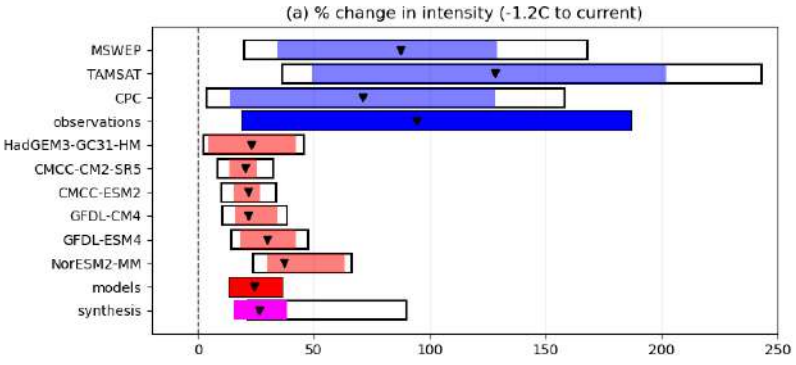

Figure A.5.6 Synthesised changes Synthesis of intensity changes in RX30day for OND 2023 flood event over Horn of Africa. Changes in intensity comparing the event in a 2022 climate to a 1.2 cooler climate. Source: [WWA, 2020-22 Horn of Africa Drought]

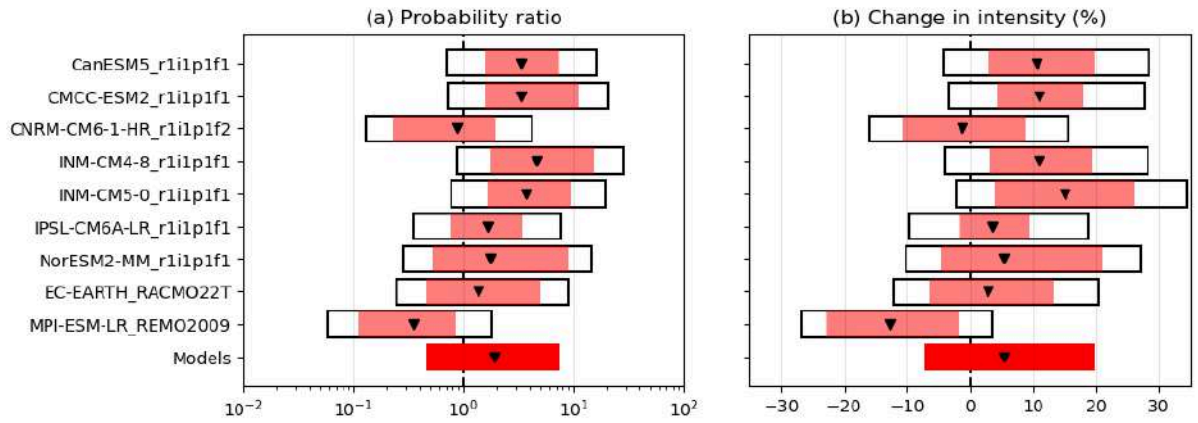

Figure A.5.8 Synthesised changes in probability ratio and intensity in RX30day for MAM 2024 flood event over East Africa. Changes in intensity comparing the event in a 2024 climate to a 1.3 cooler climate. Source: [WWA, 2024 East Africa floods]

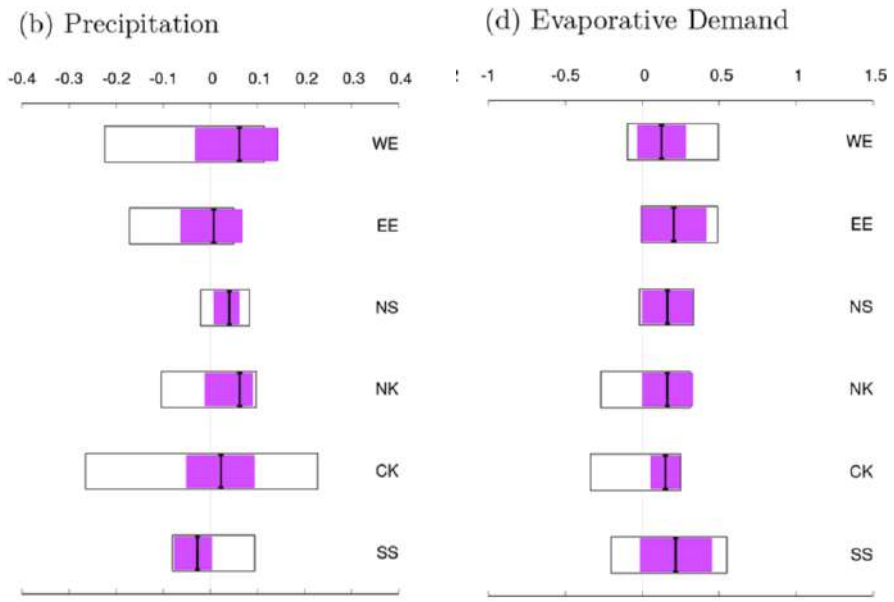

Figure A.5.9 Summary of the synthesised values for trends per degree of global mean surface temperature increase for precipitation [mm/d/K] (left) and evaporative demand [mm/d/K] (right) for six subregions of the Horn of Africa - see source for details. Magenta bars denote the weighted averages of observations and models, and white bars the unweighted averages. Source: [Kew et al. (2021)], Fig. 6.

A.6 Indian floods 2013

A.6.1 Model evaluation

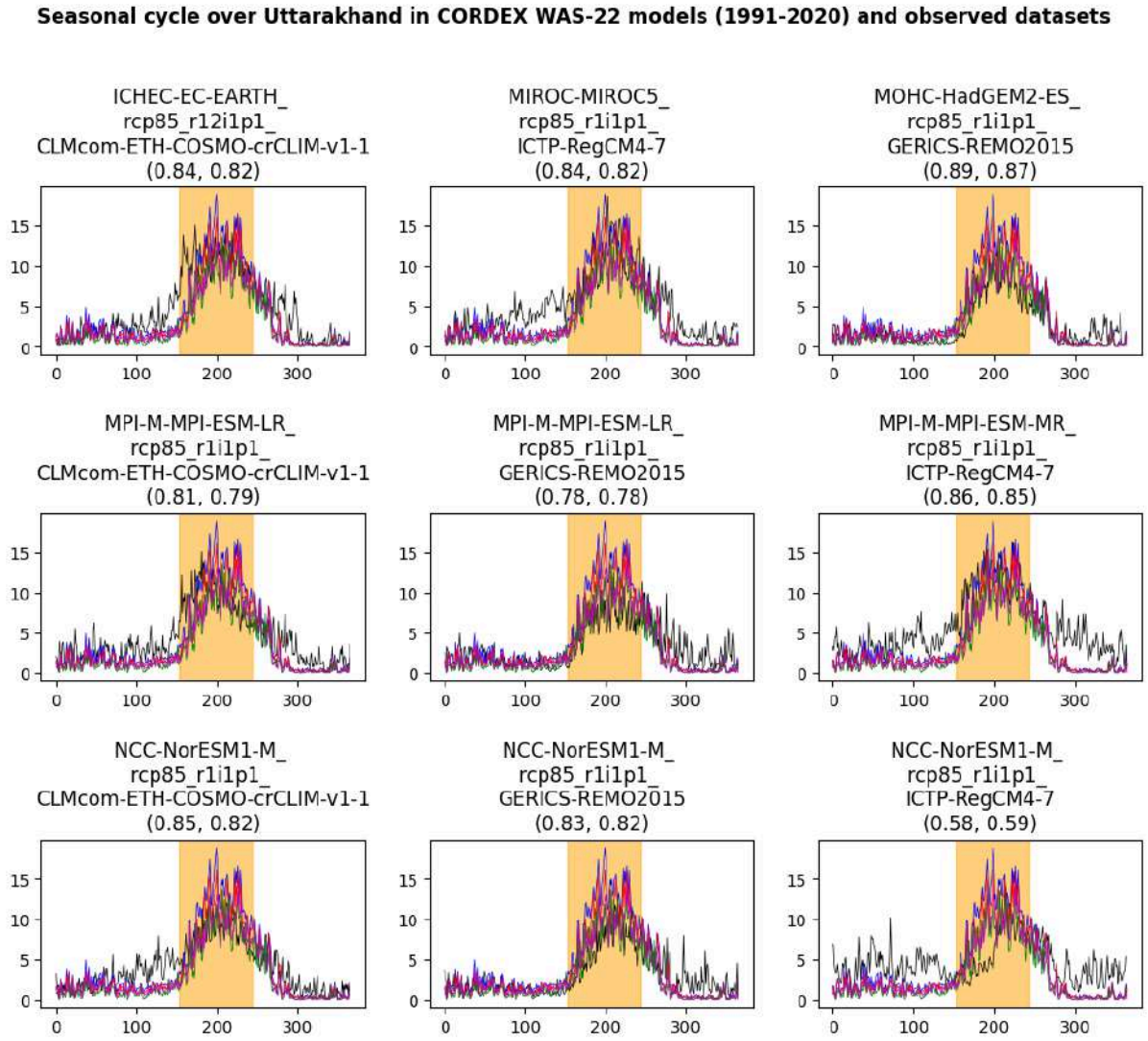

Figure A.6.1: Seasonal cycles of precipitation over the Uttarakhand study region in CORDEX models (black) and observations represented by ERA5 (blue), MSWEP (red), CPC (green) and IMD (magenta) for a climatology period 1991-2020.

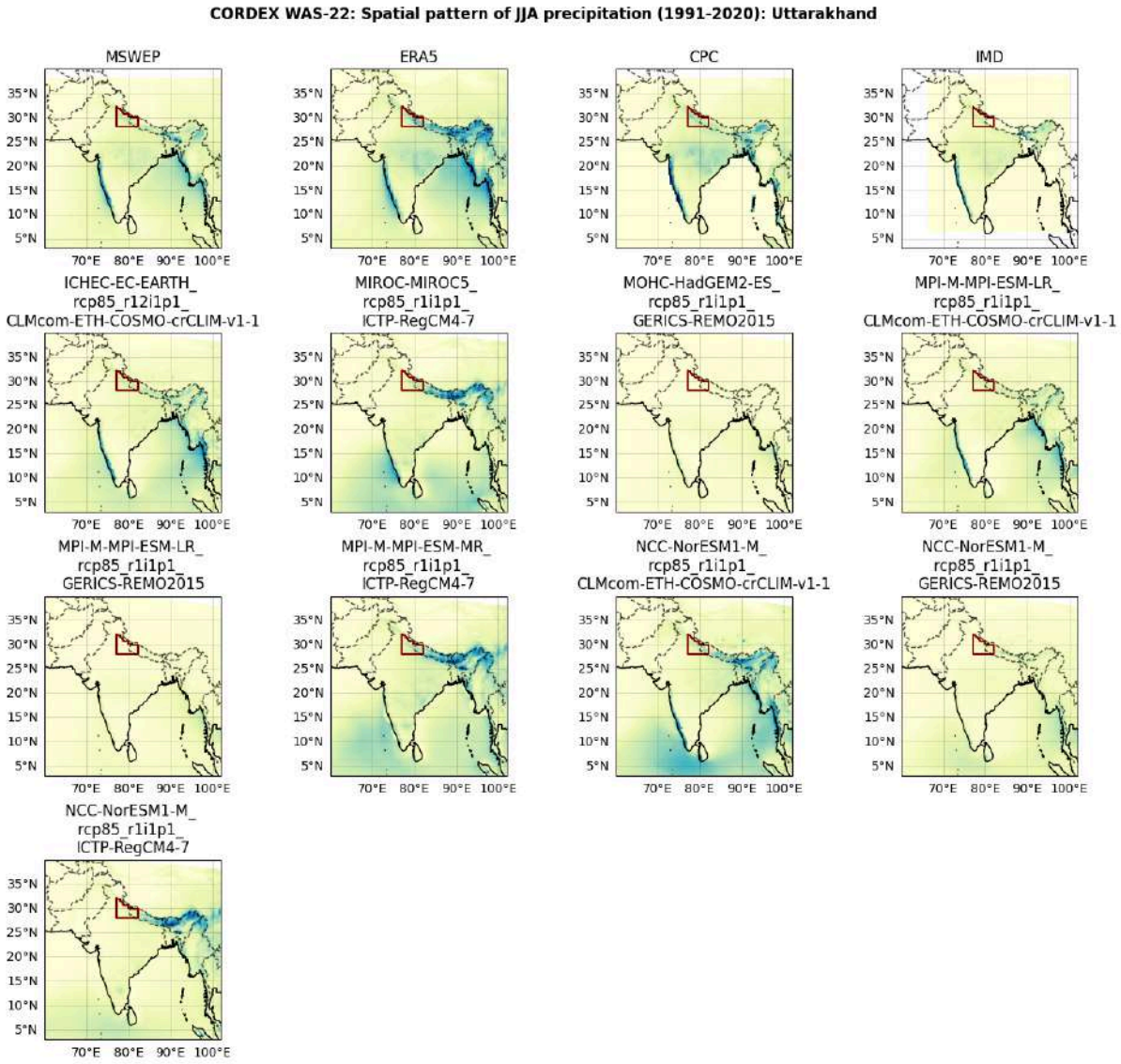

Figure A.6.2: Spatial patterns of precipitation for June-August over the region in CORDEX models and observations (top row) for a climatology period 1991-2020. The study region for the Uttarakhand flood event is shown in red.

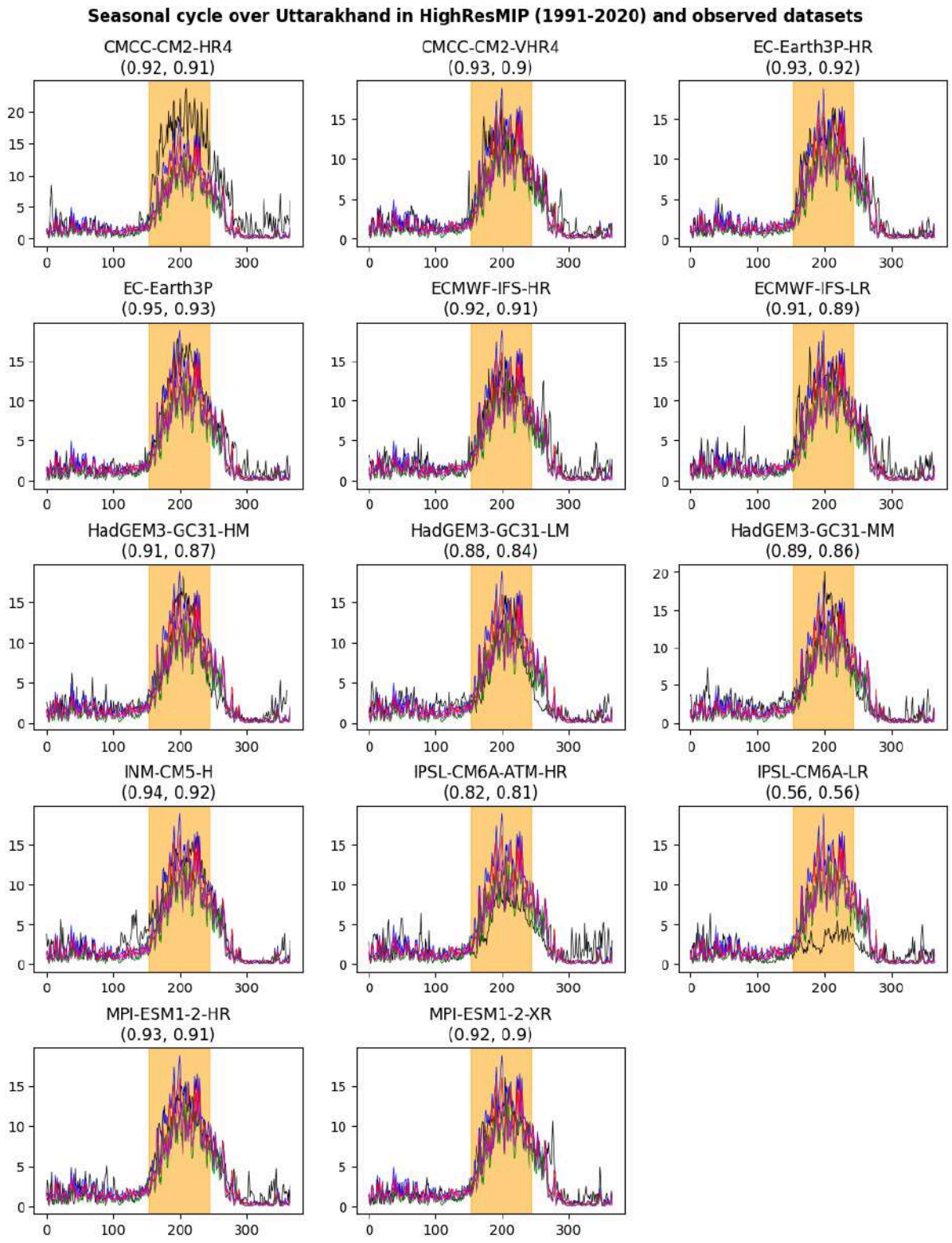

Figure A.6.3: Seasonal cycles of precipitation over the Uttarakhand study region in HighResMIP models (black) and observations represented by ERA5 (blue), MSWEP (red), CPC (green) and IMD (magenta) for a climatology period 1991-2020.

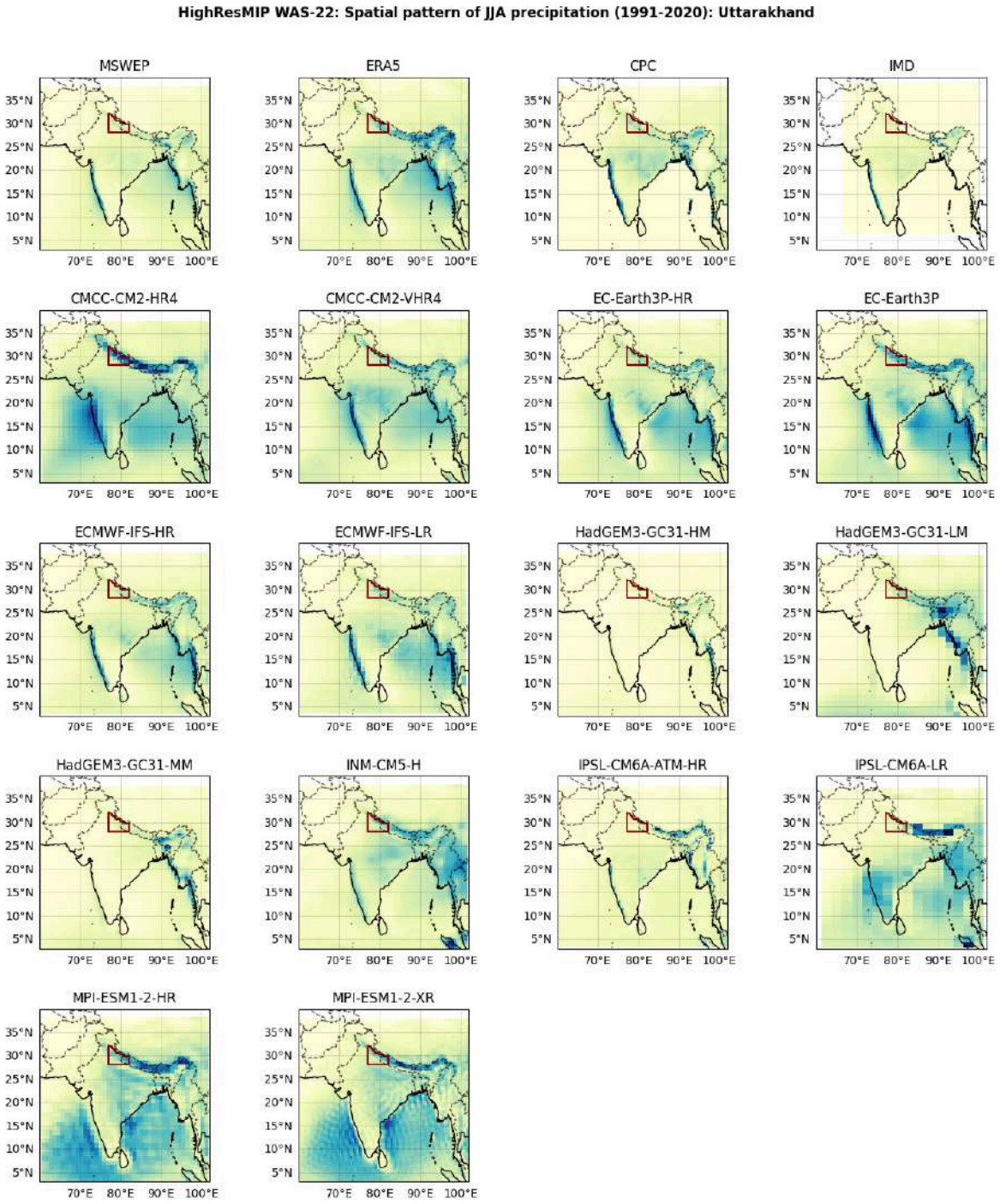

Figure A.6.4: Spatial patterns of precipitation for June-August over the region in HighResMIP models and observations (top row) for a climatology period 1991-2020. The study region for the Uttarakhand flood event is shown in red.

Table A.6.1: Evaluation of the climate models considered for attribution of extreme rainfall over Uttarakhand. For each model, the best estimate of the dispersion and shape parameters are shown and a 95% confidence interval for each, obtained via bootstrapping. The qualitative evaluation is shown in the right-hand column.

Model / Observations	Seasonal cycle	Spatial pattern	Dispersion	Shape parameter	Conclusion

IMD			0.255 (0.180 ... 0.304)	-0.027 (-0.346 ... 0.281)	
ERA5			0.238 (0.183 ... 0.274)	0.009 (-0.237 ... 0.322)	
MSWEP			0.173 (0.119 ... 0.220)	-0.080 (-0.603 ... 0.286)	
CORDEX WAS					
EC-EARTH_rcp85_r12i1p1_CLMcom-ETH-COSMO-crCLIM-v1-1 (1)	reasonable	good	0.230 (0.179 ... 0.267)	-0.070 (-0.304 ... 0.180)	reasonable
HadGEM2-ES_rcp85_r1i1p1_GERICS-REMO2015 (1)	good	bad	0.216 (0.157 ... 0.256)	-0.199 (-0.040 ... 0.452)	bad
MIROC5_rcp85_r1i1p1_ICTP-RegCM4-7 (1)	reasonable	good	0.294 (0.221 … 0.344)	-0.052 (-0.247 … 0.157)	reasonable
MPI-ESM-LR_rcp85_r1i1p1_CLMcom-ETH-COSMO-crCLIM-v1-1 (1)	reasonable	good	0.252 (0.206 … 0.291)	-0.069 (-0.275 … 0.107)	reasonable
MPI-ESM-LR_rcp85_r1i1p1_GERICS-REMO2015 (1)	reasonable	bad	0.263 (0.202 … 0.316)	0.209 (-0.077 … 0.423)	bad
MPI-ESM-MR_rcp85_r1i1p1_ICTP-RegCM4-7 (1)	reasonable	reasonable	0.330 (0.249 … 0.400)	-0.174 (-0.462 … 0.033)	reasonable
NorESM1-M_rcp85_r1i1p1_CLMcom-ETH-COSMO-crCLIM-v1-1 (1)	reasonable	reasonable	0.254 (0.184 … 0.297)	-0.120 (-0.266 … 0.163)	reasonable
NorESM1-M_rcp85_r1i1p1_GERICS-REMO2015 (1)	reasonable	bad	0.301 (0.229 … 0.354)	0.101 (-0.092 … 0.327)	bad
NorESM1-M_rcp85_r1i1p1_ICTP-RegCM4-7 (1)	bad	reasonable	0.391 (0.315 … 0.449)	-0.056 (-0.474 … 0.123)	bad
HighResMIP					
CMCC-CM2-HR4 histSST-present (1)	reasonable	bad	0.244 (0.190 ... 0.286)	0.038 (-0.17 ... 0.25)	bad
CMCC-CM2-VHR4 histSST-present (1)	good	reasonable	0.212 (0.159 ... 0.252)	0.082 (-0.089 ... 0.31)	reasonable
EC-Earth3P-HR histSST-present (1)	good	reasonable	0.200 (0.166 ... 0.229)	-0.20 (-0.42 ... -0.065)	reasonable
EC-Earth3P histSST-present (1)	good	reasonable	0.182 (0.149 ... 0.213)	0.072 (-0.16 ... 0.28)	reasonable
ECMWF-IFS-HR histSST-present (1)	good	good	0.239 (0.181 ... 0.283)	-0.12 (-0.29 ... 0.012)	good
ECMWF-IFS-LR histSST-present (1)	good	good	0.261 (0.209 ... 0.295)	-0.017 (-0.20 ... 0.22)	good
HadGEM3-GC31-HM histSST-present (1)	good	bad	0.170 (0.135 ... 0.196)	-0.095 (-0.29 ... 0.069)	bad

HadGEM3-GC31-LM histSST-present (1)	reasonable	bad	0.234 (0.187 ... 0.279)	-0.50 (-0.91 ... -0.30)	bad
HadGEM3-GC31-MM histSST-present (1)	reasonable	bad	0.273 (0.203 ... 0.328)	-0.10 (-0.22 ... 0.040)	bad
INM-CM5-H histSST-present (1)	reasonable	reasonable	0.201 (0.159 ... 0.234)	0.13 (-0.28 ... 0.37)	reasonable
IPSL-CM6A-ATM-HR histSST-present (1)	reasonable	reasonable	0.253 (0.203 ... 0.297)	0.30 (0.058 ... 0.55)	reasonable
IPSL-CM6A-LR histSST-present (1)	bad	bad	0.274 (0.223 ... 0.317)	0.21 (0.017 ... 0.38)	bad
MPI-ESM1-2-HR histSST-present (1)	good	bad	0.194 (0.157 ... 0.225)	0.15 (-0.061 ... 0.36)	bad
MPI-ESM1-2-XR histSST-present (1)	reasonable	bad	0.192 (0.152 ... 0.221)	0.17 (-0.025 ... 0.40)	bad

A.6.2 Synthesis figures

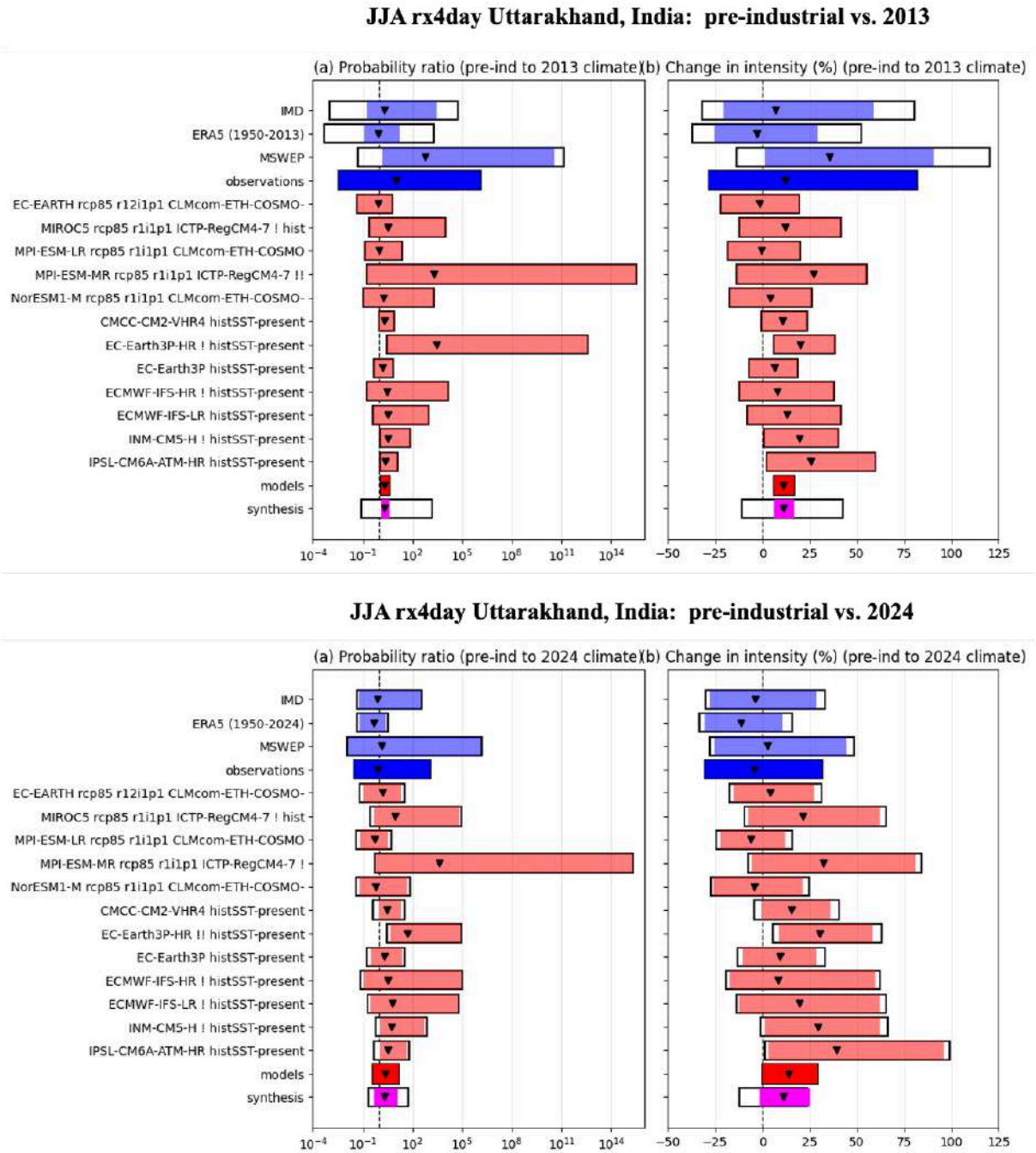

Figure A. 3.5. Synthesised changes for a 100-year 4-day JJA maximum rainfall event over Uttarakhand, India, due to GMST. Changes in PR (left) and intensity (right) are shown for two historical periods: comparing the climate at the time of occurrence with a pre-industrial (pre-ind) climate that would have been 0.9°C cooler climate as compared to the 2013 climate (top row) and comparing the present 2024 climate with the pre-ind climate that would have been 1.3°C cooler climate as compared to today (bottom row).